STUDY OF SUBWAVELENGTH STRUCTURES FOR OPTICAL BEAM FOCUSING AND LASER CAVITY

RAKESH G. MOTE

School of Mechanical & Aerospace Engineering

A thesis submitted to the Nanyang Technological University
In partial fulfillment of the requirement for the degree of
Doctor of Philosophy

2011

Dedicated to my parents and family members …

Acknowledgements

When our perils are past, shall our gratitude sleep?

- *George Canning*

A PhD thesis can never be completed by the author alone without the assistance of several people. The most pleasant aspect of completing the thesis is that it gives me the opportunity to thank the people who in one way or another made it possible.

First, my thanks go to my supervisor Assoc. Prof. Wei Zhou and co-supervisor Assoc. Prof. Siu Fung Yu for giving me the opportunity to work out this thesis in their research team. Thanks to them for personal support, encouragement, advice and patience throughout my tenure at the institute, without which the thesis would not have been in a better shape. I would also like to express my sincere thanks to Prof. A.K. Asundi, Assoc. Prof. M. Murukeshan and Assoc. Prof. C. Sherwood for making the time to participate in my thesis examination. Thanks are also due to anonymous reviewers who examined my research papers and thesis and assisted me in improving the manuscripts.

I am very grateful to Prof. Tapan Bagchi (IIT Kharagpur) for his motivation in pursuing doctoral studies. Thanks to Prof. V.K. Jain and Prof. S.K. Choudhury of IIT Kanpur, for providing me references for NTU application.

I should give my gratitude to Dr. Yongqui Fu for insightful discussions in the initial stage of the thesis. I would like to acknowledge the time and efforts by Dr. Haixia Qian for my FIB training. Many sincere thanks to Dr. Xiaofeng Li, Dr. Wang

Jun and Manu Vaishakh for technical discussions. Special thanks to Ashwani Kumar and Wang Qian for their assistance in conducting NSOM experiments.

I thank friendly staff of Precision Engineering and Nanotechnology (PEN) Center for their help in providing technical and administrative facilities. I sincerely thank to FEI Singapore for their prompt technical support whenever needed for FIB experiments. Thanks are also due to support team of Lumerical Inc., Canada for their valuable inputs in FDTD simulations.

I thank the other members of the group for contributing to a supportive working atmosphere and many memorable events over the past four years. Special mention of my group mate Yingchun. I thank her for her friendly gestures and timely help.

How could be any acknowledgment complete without mentioning family members? I am colossally indebted to my parents (आई, नाना) and my brother, Mahesh (बबलू). Their love and support have been a continuing source of inspiration in my life. What to say about my other better half? I thank my wife, Manisha, for her good cheer in the face of the demands of the task and I deeply appreciate her adjustments to the vagaries of my scholarship. I appreciate my beloved daughter, Srishti, who was too young to understand her Papa's frequent mood swings. They all deserve fruits of hardships more than anybody else does, including me.

Table of Contents

Acknowledgements iii

Table of Contents v

List of Figures viii

List of Tables xvii

List of Abbreviations and Symbols xviii

Summary xx

Chapter 1 Introduction 1

1.1 Background and Motivation 1

1.2 Case for Subwavelength Diffractive Optics 4

1.3 Thesis Objectives and Scope 8

1.4 Research Approach and Thesis Outline 9

Chapter 2 Literature Review 10

2.1 Overcoming the Diffraction Barrier 10

2.1.1 Subwavelength Structures for Focusing Based on Surface/Evanescent Waves 12

2.1.2 Subwavelength Structures for Beam Focusing without Evanescent Waves 17

2.2 Fresnel Zone Plates 19

2.3 Modeling of Fresnel Zone Plates 20

2.3.1 Scalar Approach 20

2.3.2 Rigorous Approach 23

2.4 Structures Based on FZP 27

2.5 Polarization Issues in Diffractive Optical Elements 31

2.6 Summary 34

Chapter 3 Near Field Focusing Behavior of Fresnel Zone Plates (FZP) 36

3.1 Influence of Metallic Coating on the Diffraction Characteristics of FZPs 36

3.2 Focusing Characteristics of FZPs 43
3.2.1 The Influence of Zone Numbers on the Focal Length of FZPs 43
3.2.2 The Influence of Metallic Coating Thickness on the Focal Length and DoF of FZPs 45
3.2.3 Suppression of Higher Order Foci 48
3.3 Can FZP Structure Support SPP? 49
3.4 Improving Diffraction Efficiency with Phase Zone Plate 51
3.5 Summary 58

Chapter 4 Subwavelength Focusing Behavior of High Numerical-Aperture Phase Fresnel Zone Plates under various Polarization States 59
4.1 Theoretical Formulation 59
4.2 Rotationally Asymmetry of a Focal Spot under High NA Phase FZP 63
4.3 Comparison with Exact Calculation with FDTD 66
4.4 Amplitude FZP under Linearly Polarized Illumination 74
4.5 Rotationally Symmetric Focusing using Circularly Polarized Illumination 75
4.6 Rotationally Symmetric Focusing with Radially Polarized Illumination 78
4.7 Summary 83

Chapter 5 Near-Field Focusing of Fresnel Zone Plates (FZP) Under Linearly Polarized Illumination: Fabrication and Characterization Issues 84
5.1 Fabrication of FZP using FIB 84
5.1.1 Amplitude Zone Plates 84
5.1.2 Phase FZP 87
5.2 Optical Characterization using Near-field Scanning Optical Microscope (NSOM) 92
5.3 Results 97
5.4 Summary 102

Chapter 6 Design and Analysis of Two-Dimensional High-Index-Contrast Grating (HCG) Surface-Emitting Lasers 103
6.1 High-Index-Contrast Grating (HCG) 103
6.1.1 Distributed Bragg Reflectors (DBR) 103

6.1.2 HCG Mirrors 106
6.2 Design and Analysis 112
6.3 Influence of Design Parameters on the Performance of 2D HCG 117
6.4 Surface Emitting Laser with 2D HCG 120
6.5 Summary 122

Chapter 7 Conclusions and Future Work **123**

7.1 Conclusions 123
7.2 Future Work 126

References **128**

Appendix A **141**

Appendix B **144**

Appendix C **149**

List of Publications **161**

List of Figures

Figure 1.1 Advantage of diffractive optics over refractive optics in achieving compact devices (a) a prism (b) a lens [9]. 5

Figure 1.2 Fresnel zone plate applications in (a) high resolution soft X-ray microscopy [17] and (b) high resolution mask-less lithography (Zone-plate-array lithography, ZPAL) [18]. 7

Figure 2.1 (a) SEM image of the 50 nm Ag film containing 200 nm diameter holes arranged on a quarter circle with a 5 μm radius (b) NSOM image taken at 532 nm incident wavelength and horizontal polarization (Yin et al [36]).. 13

Figure 2.2 (a) A nano-slit lens comprising of a nano-slit array with different width formed on thin metallic film (b) FDTD simulated Poynting vector distribution after focusing with nano-slit lens. (Shi et al [39]).... 14

Figure 2.3 (a) Symmetrical nanostructure for enhanced SPR (b) Cross section of the beam profile for the corrugation with tuned depth and 60-nm constant groove depth at a distance of z = 1 μm, respectively. Beam spot size δ at FWHM is ~ 600 nm (Fu et al [40]). 15

Figure 2.4 (a) A nanostructure comprising of a single subwavelength slit in Ag surrounded by grooves with traced depth profile. (b) Focal length and spot size dependence on depth profile. FDTD simulated $|H_y|^2$ distribution for (c) structure I and (d) structure II. (Shi et al [43])......... 16

Figure 2.5 (a) Subwavelength slit surrounded by chirped dielectric surface gratings (b) The focusing intensity distribution (Kim et al [44]). 16

Figure 2.6 Quasi-periodic array of nanoholes acts as (a) a light concentrator producing *hot-spot* foci (b) a lens imaging two closely spaced optical point-sources. (c) Dependence of resolution and focusing intensity on a height (h) above the nanohole array. (Huang et al [49, 50]).......... 18

Figure 2.7 (a) Micro-nano fiber array (MNF) (b) Focusing by MNF array in the far-field (c) Subwavelength focusing characteristics of focal spot (*XX'*) (Wang et al [51]). 19

Figure 2.8 (a) Construction of Fresnel zones. Amplitude or Fresnel zone plates: (b) positive zone plate (c) negative zone plate. 20

Figure 2.9 Geometry of diffraction aperture consisting of FZP and observation plane. (ρ, ϕ) are polar co-ordinates of a point in FZP plane. 20

Figure 2.10 Illustration of validity regions for different scalar diffraction theories .. 22

Figure 2.11 Zone plate structures approximated by an infinite grating under plane wave illumination for coupled-wave analysis (Schneider et al [61]). 24

Figure 2.12 Approximate local linear grating model for diffractive lens (Sheng et al [66]). 25

Figure 2.13 (a) Imaging scheme using photon sieve. (b) Focal spot intensity pattern by photon sieve and FZP. Note reduced side-lobes and improved spot-size. (c) Intensity distribution along propagation axis showing suppressed higher-order foci with the use of photon sieve. (Kipp et al [73]). 28

Figure 2.14 (a) Composite FZP proposed by Simpson et al [78] (b) Fractal zone plate structure proposed by Saavendra et al [79] 30

Figure 2.15 A volume zone plate in fused silica [83]. 31

Figure 2.16 Polarization dependent diffractive lens formed by unique orientation pattern of subwavelength gratings. Illumination wavelength, $\lambda = 10.6$ µm. [88] 33

Figure 2.17 Focusing characteristics of a continuous profile diffractive lens (a) and (b); and of a binary subwavelength diffractive lens for TE and TM polarization states. Illumination wavelength, $\lambda = 10$ µm [90]. 34

Figure 3.1 Construction of amplitude Fresnel zone plate (adapted from [92]). 37

Figure 3.2 Illustration of Rayleigh criterion showing tolerable wavefront deviation for the ideal imaging system. 39

Figure 3.3 Plot of maximum FZP diameter and corresponding number of Fresnel zones as a function of the focal length under paraxial approximation. Illumination wavelength is 633 nm. 40

Figure 3.4 (a) Plots of intensity distribution of the transmitted electric fields in *xz* plane($y = 0$): (i)-(iv); *yz* plane ($x = 0$): (v)-(viii); and *xy* ($z = f_c$): (ix)-(xii). Plots of focal spot intensities along (b) x ($y = 0$, $z = f_c$) (c) y ($x = 0$, $z = f_c$) and (d) z ($x = y = 0$) directions. f_c is the focal length obtained from the FDTD simulation. The white boxes drew in (a) are the cross section of the metal coatings.. 42

Figure 3.5 Shift of focal length (from its designed values) versus designed focal lengths (i.e., 0.5 μm, 1μm, 2 μm and 5 μm). It is assumed that the wavelength of incident plane wave is 633 nm and thickness of all metal films is 300 nm... 44

Figure 3.6 (a) Profile of electric field intensity (in a.u.) along the z ($x = y = 0$) direction. The inset shows focal length and DoF versus *Ag* thickness. (b) Profile of electric field intensity (in a.u.) along x ($z = f_c$) direction. Inset plots the peak intensity and FWHM of the focal spot versus film thickness. The FZPs have focal length of 0.5 μm under the illumination of 633 nm plane wave... 47

Figure 3.7 Plots of deviations of phase difference (from constructive interference from all 8 transparent zones) versus z-direction normalized by f. 49

Figure 3.8 Plots of transmission spectra versus illumination wavelength through a hole (of 300 nm in diameter) from a 300 nm thick *Ag* film surrounded by annular corrugations (with periodic and FZP structures) with an etch depth of 60 nm on both sides of the films. 51

Figure 3.9 Electric field intensity distribution verses x ($y = 0$ and $z = f_c$) direction for phase zone plates with $f = 0.5$ to 5.0 μm etched on glass all with etch depth of 300 nm. 53

Figure 3.10 Peak electric field intensity (in a.u.) versus etch depths at focal plane for focal length equal to 0.5 μm, 1 μm, 2 μm and 5 μm. Fresnel zone structure (8 zones) was etched on glass substrate for 100 – 800 nm depths. Wavelength of incident plane wave is 633 nm......................... 54

Figure 3.11 Electric field intensity distribution (in a.u.) along the x (y = 0 and z = f_c) direction. The inset shows peak electric field intensity and focal spot size (FWHM) at various etch depths (b) Electric field intensity distribution (a.u.) along the z-direction (x = y = 0). Inset shows actual focal length and DoF versus etch depths. Fresnel zone structure was etched on glass substrate for 100 – 692 nm depths. Wavelength of incident plane wave is 633 nm. 8 zones are designed for focusing at 0.5 µm. 55

Figure 3.12 (a) Electric field intensity distribution (in a.u.) along the x (y = 0 and z = f_c) direction. The inset shows peak electric field intensity and focal spot size (FWHM) at various etch depths (b) Electric field intensity distribution (a.u.) along the z-direction (x = y = 0). Inset shows actual focal length and DoF versus etch depths. Fresnel zone structure was etched on glass substrate for 100 – 692 nm depths. Wavelength of incident plane wave is 633 nm. 8 zones are designed for focusing at 5 µm. 57

Figure 4.1 Schematic cross section of a binary phase FZP. 61

Figure 4.2 (a) Near-field focusing characteristics of a phase FZP with 8 zones (NA = 0.996) under linearly polarized illumination obtained from the analytical model. Electric field intensity distribution shown at the focal plane of the phase FZP with $\Delta = \pi$. (b) Polarization vector distribution of a linearly polarized source. Cross-section shown is a xy-plane and polarization direction is along x-axis. (c) Polarization vectors after focusing of a linearly polarized beam by FZP. 64

Figure 4.3 Plot of $|E|^2$ along the x-axis versus different NA. 65

Figure 4.4 Depolarization ratio against phase difference, Δ, of the phase FZP for NA = 0.996. 66

Figure 4.5 Near-field focusing characteristics of a phase FZP with 8 zones (NA = 0.996) under linearly polarized illumination obtained from FDTD simulation. Electric field intensity distribution observed at the focal plane of the phase FZP with etch depth of 692.5 nm. 67

Figure 4.6 Plots of $|E|^2$, $|E_x|^2$ and $|E_z|^2$ along the x-axis for the phase FZP with etch depth of 200 and 692.5 nm. 68

Figure 4.7 Near-field focusing characteristics of a phase FZP with 8 zones (NA = 0.996) under linearly polarized illumination obtained from FDTD simulation. Electric field intensity distributions observed at the focal plane of the phase FZP with etch depth of 200 nm. 69

Figure 4.8 Depolarization ratio against etch depth of the phase FZP for NA = 0.996. 70

Figure 4.9 Effect of focused Gaussian source size (FWHM) on FWHM of focal spot. PW: Plane wave. 71

Figure 4.10 Comparison of flat-top and Gaussian illumination for phase FZPs. Detailed $|E|^2$ profile in the focal plane under illumination beam width (FWHM) of 4 μm for (a) a Gaussian source (b) a flat-top source. 72

Figure 4.11 Comparison of flat-top and Gaussian illumination for phase FZPs. Detailed $|E|^2$ profile in the focal plane under illumination beam width (FWHM) of 4 μm for (a) a Gaussian source (b) a flat-top source. 73

Figure 4.12 Detailed intensity distribution in the focal plane obtained by FDTD simulations for amplitude FZP (*Au* coating of 200 nm thickness) under linearly polarized illumination along *x*-axis. 75

Figure 4.13 Detailed intensity distribution in the focal plane obtained by FDTD simulations for a phase FZP under circularly polarized illumination. Etch depth of 200 nm was used in a glass. 76

Figure 4.14 Comparison of phase and amplitude FZPs under circularly polarized illumination. (a) Plots of $|E|^2$ and $|E_z|^2$ along the *x*-axis for phase FZP (glass with etch depth of 200 nm) and amplitude FZP (Au coating of 200 nm thickness) in the focal plane. (b) Intensity distribution in the focal plane for amplitude FZP. 77

Figure 4.15 (a) Radial and azimuthal porlarization as a linear superposition of orthogonally polarized Hermit-Gaussian modes. (b) Polarization vectors after focusing of a radially polarized beam by FZP. 79

Figure 4.16 Plots of $|E|^2$ and $|E_r|^2$ along the *x*-axis for the phase FZP with 8 zones (NA = 0.996) and $\Delta = \pi$ under illumination of radially polarized

light. Solid and dashed lines represent the calculation obtained from the analytical model and FDTD simulation respectively. 82

Figure 4.17 Detailed intensity distribution obtained by FDTD simulations for phase FZP under radially polarization illumination. 82

Figure 5.1 (a) Zone plate design used for fabrication (b) FIB milled zone plate on *Ag* coated glass (focal length 4 µm, λ = 488 nm) as per design shown in (a). (c) End point monitor graph for milling at beam current 30 pA, milling time 269 s. 86

Figure 5.2 SEM images of zone plate arrays on *Ag* coated glass with focal length (a) 4 µm (λ = 488 nm) and (b) 1 µm (λ = 633 nm). 87

Figure 5.3 Pattern shift due to charge accumulation under serial milling with ion beam current of 30 pA. 88

Figure 5.4 FIB fabricated phase FZPs in glass with focal lengths (a) f = 5 µm and (b) f = 2 µm (λ = 633 nm). Inset shows corresponding AFM scan image. (c) Zone profile by AFM measurements showing tilted sidewalls for a phase FZP shown in (a). For FIB milling, beam current was set to 50 pA with a dwell time of 1 µs. 89

Figure 5.5 Influence of zone wall tilt on focusing intensity ($|E|^2$) of phase FZP calculated by FDTD simulations. The designed zone width is at (a) center and (b) bottom of groove. Intensities are normalized by electric field intensity calculated with vertical sidewalls (i.e. tilt angle = 0). Phase FZP has a focal length of 0.5 µm (λ = 633 nm). 90

Figure 5.6 (a) FZP design for 500 nm focal length at λ = 633 nm and zone profile used for fabrication. (b) SEM image of phase FZP used for NSOM measurements. (c) SEM image of FIB sectioned phase FZP with focal length 0.5 µm. For fabrication, beam current was set to 30 pA and dwell time to 500 ns with a total milling time of 45 min. Design zone widths are observed at the center of zone depths. 91

Figure 5.7 Various NSOM configurations: (a) Transmission mode and (b) Reflection mode. 93

Figure 5.8 Commonly used NSOM probes (a) Cantilever probe [143] (b) Optical fiber probe attached to a tuning fork [144]. 94

Figure 5.9 Near-field measurement set-up. 96

Figure 5.10 Topography of FIB fabricated FZP (a) NSOM topograph and (b) corresponding SEM micrograph for comparison. 96

Figure 5.11 Profiles of electric field intensity after transmitted through the phase FZP at planes located at (a) z ~ 10 nm, (b) z = 525 nm, (c) z = 600 nm and (d) z = 750 nm from the surface of phase FZP. Incident polarization is shown with solid white arrow....................................... 98

Figure 5.12 Plot of normalized total electric field intensity, $|E|^2$, after transmitted through the phase FZP along (a) x-z plane and (b) the focal (x-y) plane located at z = 630 nm obtained from the FDTD simulation. The incident polarization is shown with a solid white arrow. (c) Comparison of total intensity obtained by FDTD results and NSOM measurements along propagation direction (z-axis). Error bar depicts forth-order polynomial fit to NSOM data standard deviations (upper error bars) and measurement error (lower error bars). 99

Figure 5.13 Plot of normalized total field intensity, $/E/^2$, after passing through the phase FZP in the x-y plane obtained from the NSOM measurement (solid lines) and FDTD simulation (dashed lines). (a) z = 600 and (b) z = 750 nm. 101

Figure 6.1 (a) Concept of laser cavity with mirrors at opposite ends. (b) Distributed Bragg reflector (DBR) pairs as a replacement of conventional crystal facet mirrors. 104

Figure 6.2 (a) Multilayer DBR configuration with Al_2O_3/ZnO thin films and (b) reflection spectra with 11.5 pairs of Al_2O_3/ZnO [155]. (c) Air/semiconductor DBR configuration with InGaN and (d) theoretical reflection spectra with 3 pairs of air/InGaN [157, 158]...... 106

Figure 6.3 (a) Concept of a high-index-contrast (HCG) grating (b) reflectivity by HCG showing broadband reflection ($\Delta\lambda/\lambda$ ~ 30%) [159].............. 107

Figure 6.4 (a) HCG structure under TE polarized illumination. (b) Simulated reflectivity spectrum of HCG grating and corresponding fitted Fano resonance line shape. Q factor is ~500,000 [165]. 108

Figure 6.5 Application of 1-dimensional high-index-contrast grating (HCG) in VCSEL (a) suspended HCG as a top mirror with tunable air-gap [168] (b) HCG with thick ($h = \lambda/4$) oxide gap [169]. 109

Figure 6.6 Schematic of multi-wavelength HCG-VCSEL array design [170]. 109

Figure 6.7 HCG grating reflectivity when used as a top mirror of VCSEL (λ = 840 nm). The white dots represents fabricated HCG-VCSEL parameters that led to lasing [171]. 110

Figure 6.8 (a) Hollow-core slab waveguide with high reflective 1D HCG (b) Waveguide loss as function of grating period and semiconductor width (c) Electric field intensity profile of hollow-core HCG waveguide [172]. 111

Figure 6.9 Schematic of a 2D HCG. Thickness of grating layer, t_g, was set to 460 nm. The refractive indices of grating layer, buffer layers and substrate were set to n_H = 3.48, n_L = 1.45 and n_{sub} = 3.48 respectively. 112

Figure 6.10 Plot of (a) reflection and (b) transmission spectra of 1D and 2D HCGs. The HCGs have same period (Λ = 700 nm) and thickness of gratings (t_g = 460 nm) and were supported by an infinite thick buffer layer (i.e., $t_{buf} = \infty$). 113

Figure 6.11 Reflection spectra of 2D HCGs with varying thickness of buffer layer (i.e., t_{buf} varies between 775 and 925 nm). 115

Figure 6.12 Plot of the reflection spectra of the HCGs versus normalized wavelength (i.e., normalized to the wavelength of the reflection dip). For the reflection dip at 1.343 µm, the dimensions of 2D HCG were set to Λ = 700 nm, fill factor = 65%, t_g = 460 nm and t_{buf} = 825 nm. For a reflection dip at 1.55 and 2 µm, the corresponding dimensions of 2D HCG were scaled by a factor of 1.157 and 1.489 respectively .. 117

Figure 6.13 Influence of (a) period of grating (Λ) (b) fill factor (c) grating thickness (t_g) and (d) polarization angle on the reflectivity of 2D HCG. 118

Figure 6.14 Influence of sidewall tilt angle on reflection characteristics: (a) the bottom width of the grating remains constant (b) the middle width of

the grating remains constant. 0 deg implies vertical side walls. HCG parameters are: Λ = 700 nm, fill factor = 65%, t_g = 460 nm. 119

Figure 6.15 Surface emission spectra of 2D HCG lasers with t_{buf} of 725 nm and infinite thick. The inset shows the reflectivity and 10% linewidth (defined as the width of the dip spectrum at a level 10% above the reflection dip, see Figure 6.9) of the reflection dip, as well as the Q factor of the 2D HCGs versus t_{buf}. 122

List of Tables

Table 5.1 Optimized FIB milling time for different zone plate designs. 86

List of Abbreviations and Symbols

k	Wave number or wave vector
f	Focal length
n	Refractive index
n_H	Refractive index of high-index material
n_L	Refractive index of low-index (buffer) material
$\mathbf{r}$	Radius/position vector
t	Etch depth
t_{buf}	Buffer layer thickness
t_g	Grating thickness
w	Zone width
z	Position along light propagation direction
$\mathbf{E}$	Electric field vector
G	Free space Green's function
G_r	Reciprocal wave vector
$\mathbf{H}$	Magnetic field vector
N	Number of full zones in Fresnel zone plates
DBR	Distributed Bragg reflector
DE	Diffraction efficiency
DoF	Depth of focus
EPM	End point monitor
FWHM	Full width at half maximum
FZP	Fresnel zone plate

GAE	Gas assisted etching
ITO	Indium tin oxide
NA	Numerical aperture
NSOM	Near-field scanning optical microscope
SP/SPP	Surface plasmon/surface plasmon polariton
TE	Transverse electric
TM	Transverse magnetic
δ_{Lor}	Lorentz line-width
ε	Permittivity
ε_{Lor}	Lorentz permittivity
ϕ	Azimuth angle in the x-y plane
λ	Wavelength of light in free space
θ	Inclination angle
Δ	Phase difference
Φ	Phase function
Λ	Period of grating

Summary

With the rapid development of microelectronic industry of data processing, data storage/reading, data transmission and various optoelectronic devices, the demand for small-sized optical components and optical systems is increasing. Diffractive optics has a potential to improve optical systems by increasing their reliability, robustness, and functional integration, while reducing their effective size. The present work investigates diffractive optical elements with subwavelength features for near-field focusing and laser cavity. Fresnel zone plates (FZPs) in the visible wavelengths are considered for near-field focusing. Further, for laser cavity reflectors, 2-dimensional grating based on high-index-contrast materials is investigated.

Near-field focusing properties of Fresnel zone plates (FZP) are investigated in the visible regime by a 3-dimensional finite-difference time-domain (FDTD) method. It is shown that FZPs with different opaque coatings can achieve subwavelength focusing in the visible wavelength. All the FZPs exhibit elongated focal length and depth of focus when compared with classical calculations. The subwavelength focusing characteristic is attributed to the interference of diffracted evanescent waves from a large numerical aperture. It is found that the near-field focusing of FZPs suppresses higher order foci such that the corresponding diffraction efficiency is improved. The use of phase zone plate structured on a glass without opaque coating is proposed to improve the diffraction efficiency of subwavelength focusing.

A vector nature of illumination is an important parameter in focusing by high numerical aperture element. A simple analytical model is developed to study the subwavelength focusing characteristics of a binary phase FZP. The model shows that

high numerical aperture phase FZP under the illumination of a linear polarized light produces rotationally asymmetric focal spot with beamwidth varying from 0.36λ to 0.79λ, where λ is the wavelength. On the other hand, rotationally symmetric focal spot with a minimum beamwidth of 0.39λ can be obtained from the illumination of a radial polarized light.

Amplitude and phase FZPs are fabricated on *Ag*-coated glass substrate and bare glass substrate respectively with the use of focused ion beam (FIB) technology. Tilt of sidewall in FIB milled zones of the FZP is characterized with atomic force microscopy (AFM) and FIB sectioning. With FDTD calculations, influence of tilt in sidewalls on focusing characteristics is investigated in order to set acceptable limits on tilt angle. Focusing behavior of phase FZPs is characterized by near-field scanning optical microscope (NSOM). Focusing characteristics are found to be in qualitative agreement with simulation results.

The use of a two-dimensional high-index-contrast grating (HCG) with a square periodic lattice is proposed to realize surface-emitting lasers. This is possible because the use of 2D HCG, in which multiple resonant leaky modes are excited by two orthogonal directions of the grating, causes the high reflective zone to be split into two regions. Hence, a dip of the reflectivity is formed to support the excitation of a resonant cavity-mode inside the 2D HCG. With a suitable design on the dimensions of the 2D HCGs, Q factor as high as 1032 can be achieved.

This thesis shows capability of FZP in achieving compact focusing element in the near-field focusing with tighter focal spots, both theoretically and experimentally. It also demonstrates the suitability of 2D subwavelength HCG grating with application to compact surface emitting laser.

Chapter 1

Introduction

One day, Leo Szilard informed his friend that he is going to write a diary. "*I am not going to publish it but just to inform God about some facts*"."*Do you think that God doesn't know facts?*" asked his friend. "*I am sure, God doesn't know this version of facts,*" answered Leo.

1.1 Background and Motivation

With the rapid development of microelectronic industry of data processing, data storage/reading, data transmission and various optoelectronic devices, the demand for small-sized optical components and optical systems is increasing. For instance, smaller features may allow for faster and more compact, economical integrated circuits (IC). Moore's law [1] describes a trend by which the number of transistors that can be placed inexpensively on an integrated circuit will double approximately every two years. Since 1975, the microelectronics industry has actually managed to outperform this trend, with a 30% reduction of the structure size every 1.5 years. This has posed challenges to semiconductor manufacturing and microscopy. The trends can be highlighted as follows [2, 3]:

- Need of high density optical storage and readout technology, typically a storage density of 1 Tb/in^2 and a data transmission rate of 1 Gbps.
- The progress of DRAM technology requires the drastic improvement of photo-lithography so as to fabricate pattern with feature size well below 50 nm.

- Much more sophisticated photonic integration technologies are needed in order to cater the growth of optical fiber transmission. For instance, by 2015, photonic matrix switching device should be of subwavelength size in order to achieve integration of 1000 × 1000 elements for 10 Tbps switching capability.
- Microlens arrays are popular in sensor-type devices like digital camera for improving the light collection efficiency in charge coupled devices (CCDs). Growing demand for higher resolution digital cameras will lead to a need for much tiny microlenses having ultra-short focal lengths and larger numerical aperture with aberration free smaller spot size.

The performance of optical system is limited by the wavelength of light. The resolution of an optical microscope is ultimately limited by diffraction. This limit is imposed by a diffraction phenomenon and is usually termed as *diffraction limit*. The best resolution for visible wavelengths is around 200 nm, according to the limit derived by Ernst Abbe [4]. After Abbe's theory, Rayleigh pointed out that two point light sources can be resolved (separately imaged) when the center of the Airy disk (diffraction maximum) generated by one of the sources overlaps with the first diffraction minimum in the diffraction pattern of the second Airy disk, a condition known as the Rayleigh criterion [5], described as Equation (1.1)

$$\Delta x = 0.61 \frac{\lambda}{NA} \tag{1.1}$$

where Δx is the smallest distance distinguishable between two objects, λ is the wavelength of light applied and NA is the numerical aperture of the lens.

In case of lithography, the optical resolution based on Rayleigh formula:

$$\Delta x = \kappa_1 \frac{\lambda}{NA} \tag{1.2}$$

where κ_1 is optical system specific process factor.

It is clear that, with the choice of a shorter operating wavelength in the range extreme ultraviolet (EUV) to deep ultraviolet (DUV), desired nanometric features can be achieved. Intel has recently reported reaching a resolution of 15 nm using quadruple patterning at 193 nm wavelength. However, the choice of the illumination wavelength in shorter wavelengths regime means more complicated optics. The reliability of the source at such short wavelengths from the point of the spectral purity, power and stability is a matter of concern. The costs associated with the extra processing steps are considerable and thus constraining cost-effectiveness of the approach.

Increasing NA of the system improves resolution. Thus, the resolution of conventional lens can be enhanced by immersion technique wherein high refractive index liquids are used thereby increasing effective NA of the system [6, 7]. However, such approach is limited by choice of high index liquids.

Near-field scanning optical microscopy (NSOM) or electron beam (e-beam) microscopy/lithography approaches are not limited by conventional diffraction limit. However, complexity of the system, for example, NSOM has a practically nanometer scale working distance and an extremely small depth of field, and high cost associated with e-beam source often restricts the application. Further, for high resolution images or large specimen areas scan times are extremely large due to point-by-point scanning. This poses limit on using for mass production measurements.

It is evident that sub-wavelength focal spots cannot be formed through conventional focusing using a lens system or microscope objective. There is need of novel, compact, cost-effective optical focusing elements, which can be easily integrated into the optoelectronic systems. The thesis aims at exploring compact optical elements in order to assist laser beam generation and shaping so as to cater growing demand for compact devices needed for miniaturized systems.

1.2 Case for Subwavelength Diffractive Optics

The uses of diffractive elements for near-field imaging of visible light have been demonstrated by Marks et al [8]. They proposed reconstruction of images by diffractive elements like Fresnel lens with the aim to improve signal-to-noise ratio of the near-field imaging as well as to enable parallel measurement. Hence, it is believed that the realization of subwavelength focusing well below the diffraction limit with diffractive elements can contribute to the miniaturization of photonic devices and systems.

With their unique properties, diffractive optics can improve optical systems by increasing their reliability, robustness, and functional integration, while reducing their effective size (see Figure 1.1). Rather than being refracted at continuous surface profiles, in diffractive optical elements (DOE) light is diffracted at the periodic microstructure of the element. Thus, optical fields are changed by means of diffraction through zones of microscale features formed on a surface. Periodicity and spatial structure determines the optical performance of the diffractive elements.

As the most popular optical components, lenses are widely used in applications that range from imaging to focusing. Conventional dielectric lenses perform beam shaping via refraction of light at curved surfaces with index contrast. In the convention

of wave optics, lens provides necessary phase retardation to the optical fields originating from infinitesimal dipole elements assumed to be continuously distributed on the exit surface of a lens. Such lenses i.e. refractive optical elements (ROE) are advantageous for broadband devices as they have lower wavelength sensitivity compared to diffractive optics. In addition, it is comparatively easier to realize large numerical apertures, and, in general, a high light efficiency.

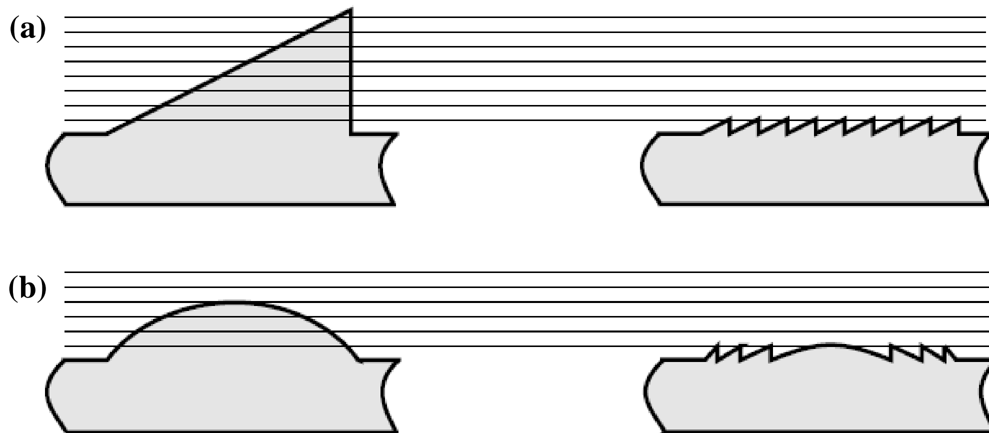

Figure 1.1 Advantage of diffractive optics over refractive optics in achieving compact devices (a) a prism (b) a lens [9].

However, the capability of conventional dielectric lenses deteriorates in scaling down to a wavelength or subwavelength range and the behavior deviates from the prediction by diffraction theories [10, 11]. This is a cause of concern with applications demanding very short focal lengths especially in the subwavelength regime. Although, recently Lee et al [12] proposed self-assembled nanoscale spherical lenses for near-field focusing, the proposed approach is challenging from the fabrication and system integration point of view. Fabrication of refractive microlenses is generally based on some (analog) physical process, such as mass transport due to surface tension and diffusion. Due to the analog nature of most fabrication techniques used for ROEs, their fabrication is often more difficult compared to the fabrication of diffractive

optics, since the process parameters need to be precisely controlled in order to achieve good reproducibility and uniformity. Furthermore, process and geometrical parameters are usually confined to certain ranges, thus leading to restrictions in design and geometry.

On the other hand, diffractive elements can be fabricated by planar techniques that are reliable and low cost. Diffractive elements can be designed to operate at any wavelength while refractive elements are constrained at short wavelengths by material transmission properties.

One interesting class of diffractive optics has critical dimensions smaller than the wavelength of the light with which they are designed to interact. Advances in micro-lithography, laser-beam writing, inductively coupled plasma writing, reactive ion etching, and e-beam writing have made it possible to produce diffractive elements with smaller features. One of the most significant results has been the high diffraction efficiencies produced by binary diffractive elements that have subwavelength features. For example, in contrast to the scalar theory prediction of 40% diffraction efficiency for binary elements, binary subwavelength elements with efficiencies over 80% were predicted [13] and demonstrated [14] in 1990s.

Recently, diffractive elements based on Fresnel zone plate (FZP) structures are receiving wider attention over a wide range of electromagnetic spectrum. FZP is an old topic in optics. Historically, FZP was proposed by Rayleigh in an unpublished work. However, first published work on FZP has been traced to Soret. Thus, FZP is also termed as *Soret lens*. It has not enjoyed much popularity in the optical systems at visible and infrared regime earlier because of following disadvantages [15]:

- Their light-collection efficiency is poor (only $1/\pi^2$ of the power incident on the zone plate participates in forming the primary image).

- They suffer from high background losses (1/4 of the light incident is undiffracted and creates a continuous background in the image plane).

However, FZP structure parameters are easy to modulate in order to provide focal lengths as per requirements. Further, while using FZP, material absorption is not a significant problem, since they can be fabricated in very thin plates, or even membranes. This fact, as well as their diffractive nature, enables zone plates to operate at any wavelength. Even neutral atoms have shown to be focused using FZP structures [16].

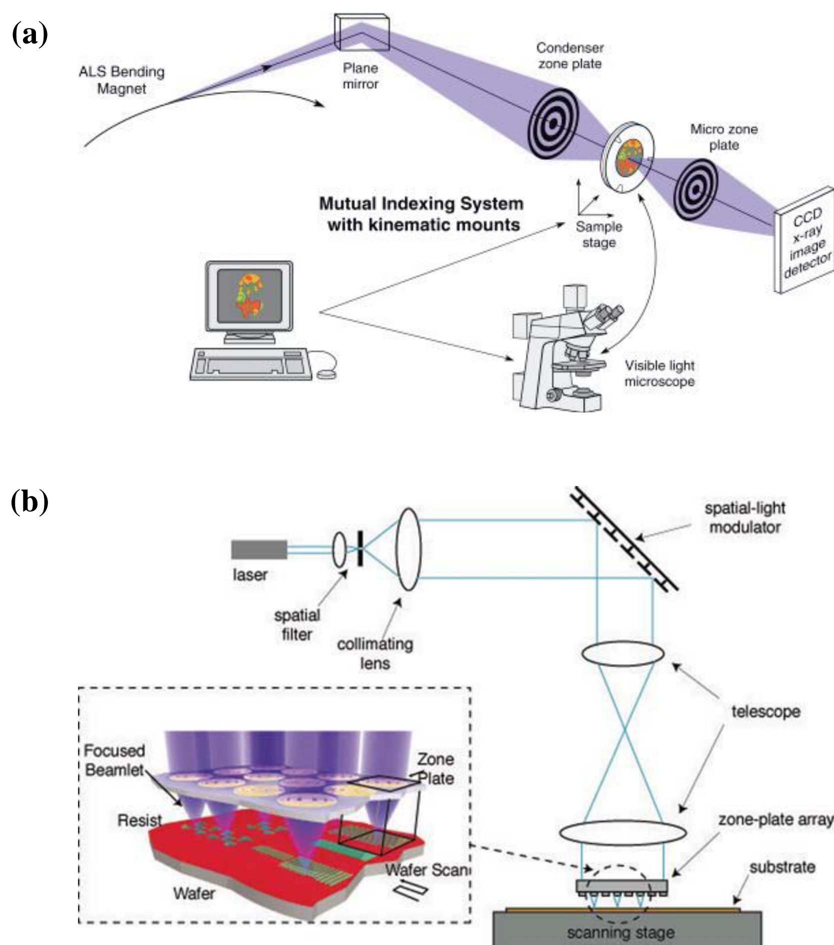

Figure 1.2 Fresnel zone plate applications in (a) high resolution soft X-ray microscopy [17] and (b) high resolution mask-less lithography (Zone-plate-array lithography, ZPAL) [18].

FZP structure has been used in obtaining spatial resolution down to 15 nm with soft X-ray microscopy [17]. High NA FZPs have been reported to be most feasible optical element in mask-less lithography with deep UV radiation [18, 19] (see Figure 1.2). In the quest of super-resolution, surface plasmon based FZP structures are used in in-plane [20] as well as out-of-plane [21] near-field focusing under optical wavelengths. With optical wavelengths, for near-field focusing, FZP features reach subwavelength dimensions and thus bring up novel focusing characteristics. In this thesis, emphasis has been put on subwavelength FZP for near-field focusing under optical wavelengths.

1.3 Thesis Objectives and Scope

The thesis aims at achieving following objectives:

- Design and analysis of planar subwavelength diffractive optical elements for near-field focusing and laser cavity.
- Fabrication, optical characterization and study of related issues of the optical elements.

In order to attain the objective, the scope of the work is as described below:

- A critical study of a prior art on devices proposed for near-field focusing. This will mainly include structures based on surface plasmon polaritons (SPP).
- Investigation of near-field behavior of FZP structure with high numerical aperture and exploring the possibility of subwavelength focusing with FZP structures.
- Study of polarization effects on focal spot profile with the use of high numerical aperture FZP and development of simplified model to predict the behavior.

- Experimental demonstration of optical performance of proposed FZP structures. Focused ion beam (FIB) will be used for fabrication and near-field optical microscope (NSOM) to ascertain focusing behavior.
- Design and analysis of subwavelength grating as reflectors in realizing laser cavity.

1.4 Research Approach and Thesis Outline

Chapter 2 presents a brief review of the literature on plasmonic subwavelength optical elements for focusing, Fresnel zone plates and its modeling. The research begins with the investigation of amplitude Fresnel zone plates for focusing in the near-field i.e. with focal lengths comparable to incident illumination and possibility of using phase zone plates for obtaining improved diffraction efficiency (**Chapter 3**). Vector nature of light i.e. incident polarization plays a crucial role in defining focal spot profile for zone plates with very high numerical aperture. **Chapter 4** presents a simplified modeling of phase zone plates to account for vector nature of light and optimizes zone plate design to improve rotational asymmetry under linearly polarized illumination. For attaining perfect rotational symmetry of a focal spot, use of radial polarization is demonstrated. Experiments are then carried out to verify the focusing characteristic of Fresnel zone plates. In **Chapter 5,** fabrication and characterization issues of zone plates are discussed. Focused ion beam (FIB) technology is employed to carry out fabrication of zone plate structures. Optical characterization is carried out with the use of near-field scanning microscope (NSOM). In addition to beam focusing, high-index-contrast grating (HCG) are studied with application to reflectors in laser cavities. Polarization insensitive 2D grating is designed and shown to be integrated with surface-emitting laser in **Chapter 6**. Conclusions are drawn in **Chapter 7** and further research directions are given.

Chapter 2

Literature Review

"*But I don't want to go among mad people*," said Alice.

"*Oh, you can't help that*," said the cat. "*We're all mad here*."

This chapter presents a review of the some of the relevant work on use of subwavelength structures, particularly structures exploiting surface plasmon polaritons (SPP), for focusing beyond diffraction limit, use of Fresnel zone plates for focusing and its modeling.

2.1 Overcoming the Diffraction Barrier

The resolving power of an optical system depends on the bandwidth of spatial frequencies ($\Delta k_{//}$) that are collected by the optical system. If two point sources are separated by a distance $\Delta r_{//}$ in the object plane [22]:

$$\Delta k_{\|} \Delta r_{\|} \geq 1 \tag{2.1}$$

The upper bound for $\Delta k_{//}$ depends on the wavenumber $k = (2\pi/\lambda)n$, where n is refractive index of the object medium, as spatial frequencies associated with the evanescent waves are decayed in the far-field.

Thus, a resolution can not be better than

$$Min\left[\Delta r_{\parallel}\right] = \frac{\lambda}{2\pi \mathrm{NA}} \tag{2.2}$$

However, Abbe's or Rayleigh's formulations are less optimistic (see Equation (1.1)). It must be noted that Rayleigh's formulation is based on a grating spectrometer, and not on an optical microscope. It is clear from Equation (2.1) that there is no limit to optical resolution provided the bandwidth $\Delta k_{//}$ is arbitrarily large. Thus, in order to break the diffraction barrier, high spatial frequency evanescent field components must be considered.

By placing an intimate-contact pre-patterned photomask, the optical near-field with high resolution details may be recorded [23]. In this case, high resolution is achieved at the expense of an inflexible and costly photomask and the high probability of contamination of the contacted surfaces. Furthermore, work by Pendry [24] introduced a concept of negative refractive index slab materials (artificial left-handed materials or meta-materials) to act as a perfect lens by focusing both the near- and far-field components emanating from a source in the microwave regime. However, in the optical regime, fabrication of artificial left-handed materials is still a challenge [25].

Surface plasmons (SPs) effect, discussed in the pioneering work of Ritchie [26] several decades ago, exhibits unique optical properties as the result of the resonant interaction between the surface charges oscillation and the incident electromagnetic wave. Surface plasmon resonance (SPR) is a quantum optical-electrical phenomenon arising from the interaction of light with a metal surface. Under certain conditions the energy carried by photons of light is transferred to packets of electrons, called plasmons, on a metal's surface. Energy transfer occurs only at a specific resonance

wavelength of light. Surface plasmons (SPs) provide the opportunity to confine light to very small dimensions.

With the assistance of SPR extraordinary far-field transmission of light via periodic arrays [27-29] of subwavelength apertures or single hole perforated in metallic films has been demonstrated. Light emerging from a subwavelength aperture is normally fully diffracted in all directions. It has been shown [30, 31] that this radiation pattern could be compressed into a narrow beam by patterning the surface immediately surrounding the exit plane of the aperture. In the directions perpendicular to the interface, the SPP intensity decays exponentially within less than 100 nm, whereas the SPP can propagate along the interface over distances approaching 1 mm [32]. Further study concentrates on beam shaping using the nanostructures to make a device for nano-focusing. However, to realize a true super-resolution imaging/focusing, one of the challenges is to devise a special coupling mechanism to convert a large band of the enhanced evanescent waves or SPP wave to propagation waves in the free space.

2.1.1 Subwavelength Structures for Focusing Based on Surface/Evanescent Waves

It is possible to confine surface plasmons along the surface with the use of subwavelength structures. Surface plasmons can be focused along the surface through reflection by surface defects via Bragg scattering or with the introduction of nano-slits to excite SPP along specific direction. In this section, a prior art on such subwavelength structures for SPP focusing is reviewed.

Liu et al [33, 34] used circular and elliptical structures to directionally excite the SPs toward the focus points. Nomura et al [35] proposed an optical far-/near-field

conversion device that can both excite SPs and focus it into a nanodot coupler. With an arc shaped hole array (see Figure 2.1) fabricated with FIB machining into Ag film, Yin et al [36] showed that SPP can be focused into an intense spot with subwavelength width. In this case, nanoholes (diameter 200 nm) act as a point like source for SPP, whose constructive interference gives rise to focusing. Longitudinal and transverse intensity profiles shows FWHM of 1400 and 380 nm.

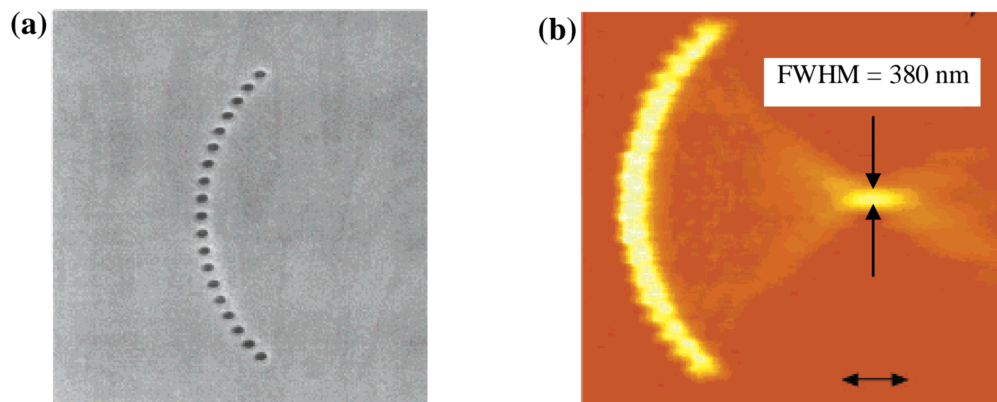

Figure 2.1 (a) SEM image of the 50 nm Ag film containing 200 nm diameter holes arranged on a quarter circle with a 5 μm radius (b) NSOM image taken at 532 nm incident wavelength and horizontal polarization (Yin et al [36]).

Excitation of surface plasmon porlariton (SPP) with subwavelength metallic structures and subsequent decoupling into radiation modes has been proposed by Sun et al [37]. With a suitable structure, radiated beam can be collimated or focused. In this section, some of the approaches to achieve beam focusing out of plane of focusing element with the assistance of SPP are reviewed.

Since the propagation constant of the SPP depends on the width of the slit, SPPs passing through different width sub-wavelength slits experience different retardations. When this property is used appropriately, the phase of the light transmitted through the slit can be modulated with specifically designed widths and light from slits converges in free space, as shown in Figure 2.2. The phase profile

(Φ) at position x to focus emitted light at a focal length f can be obtained according to the equal optical length principle as:

$$\Phi(x) = 2n\pi + \frac{2\pi f}{\lambda} - \frac{2\pi\sqrt{f^2 + x^2}}{\lambda} \tag{2.3}$$

Min et al [38] extended the nano-slit configuration by embedding a Kerr nonlinear material in metallic slit array to actively control the output beam. Nonlinear materials exhibit permittivity as a function of illumination intensity. By varying the illumination intensity, phase retardation through individual slits is shown to be manipulated and thus giving rise to different positions of focus. In other words, the focal length can be simply controlled by the intensity or beam waists of incident light.

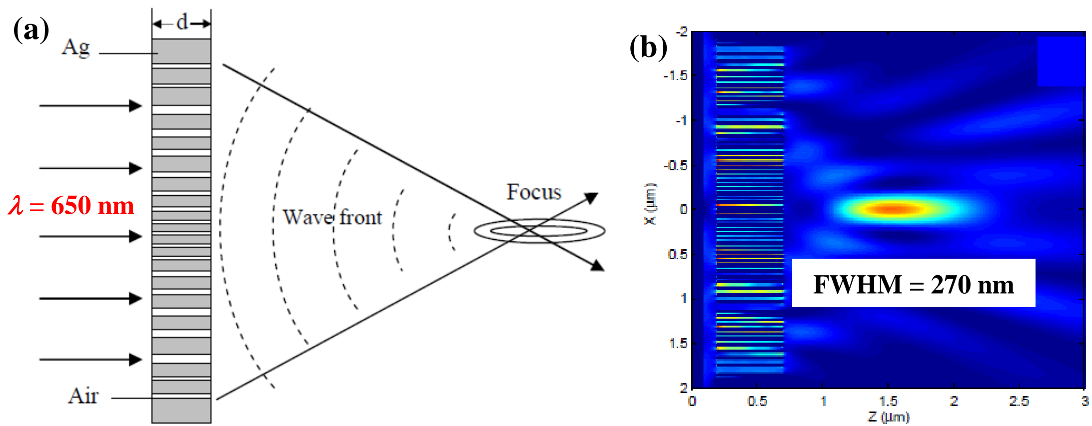

Figure 2.2 (a) A nano-slit lens comprising of a nano-slit array with different width formed on thin metallic film (b) FDTD simulated Poynting vector distribution after focusing with nano-slit lens. (Shi et al [39])

Phase modulation across the grooves can be accomplished by modifying the groove depth profile, similar to a nano-slit array with different widths. The relative phase of the light at the center of the groove exit also increases with increasing groove depth, and it varies periodically when the groove depth becomes deeper. As a result,

desired phase profile can be reached so as to yield constructive inference at the focal point.

Fu et al [40-42] introduced depth-tuned surface corrugations for the purpose of beam shaping. Figure 2.3 shows a symmetrical nanostructure having 7 slits for enhanced SPP. This nanostructure was used in a reflection mode. Transmission was reported to be as high as 8.1% with beam spot size of ~ 600 nm. However, the depth tuning did not reveal any significant change in the spot size.

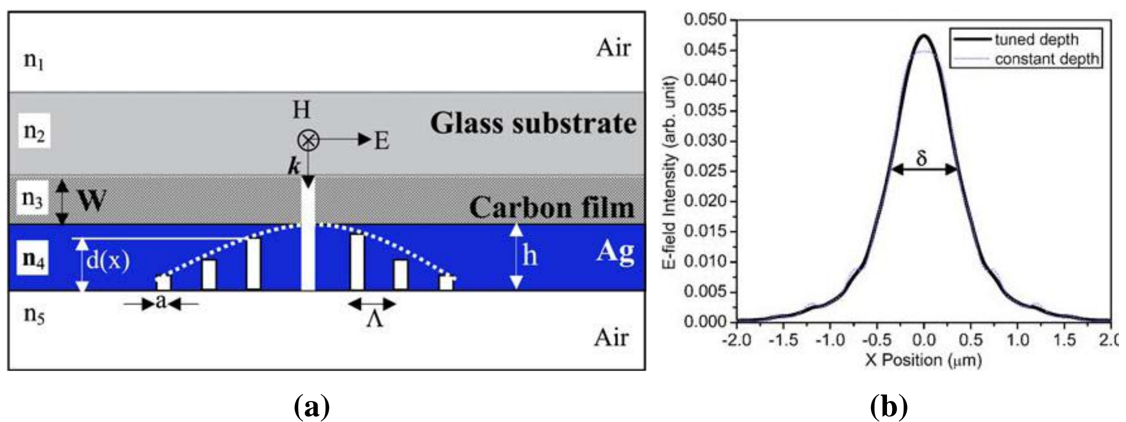

Figure 2.3 (a) Symmetrical nanostructure for enhanced SPR (b) Cross section of the beam profile for the corrugation with tuned depth and 60-nm constant groove depth at a distance of $z = 1$ μm, respectively. Beam spot size δ at FWHM is ~ 600 nm (Fu et al [40]).

Shi et al [43] have further shown focal length of groove based structure can be modulated by tuning of groove depths. The standing SPP waves in the subwavelength groove modulate relative phase distribution in the output surface depending on the groove depth distribution profile as shown in Figure 2.4(a). Consequently, focal length and spot size can be modulated (Figure 2.4(b-d)).

A subwavelength slit surrounded by dielectric grating with varying periods can be designed to form a beam spot at the desired focal point from the metal substrate, as shown by Kim et al [44]. The direction of the radiation fields generated by SPPs is changed by adjusting the distances and widths of adjacent surface gratings, resulting in

the chirped surface gratings as shown in Figure 2.5. This approach is different from the nano-slit configuration (Figure 2.2) or Fresnel zone plate configuration as it manipulates the side coupling fields or radiation fields into the free space, while the Fresnel zone plate controls the transmitted fields through its constituting components.

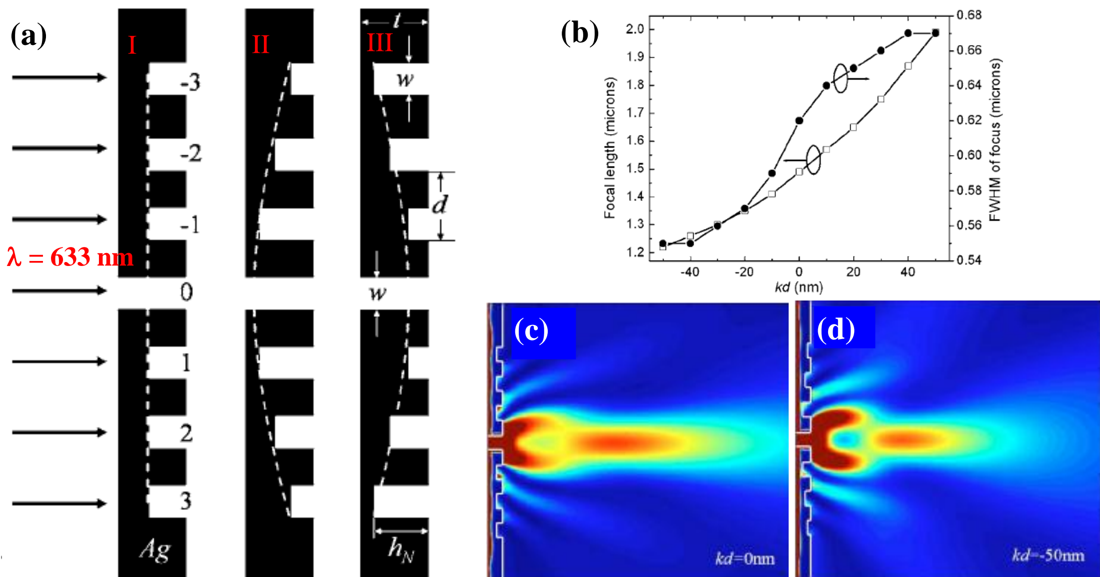

Figure 2.4 (a) A nanostructure comprising of a single subwavelength slit in Ag surrounded by grooves with traced depth profile. (b) Focal length and spot size dependence on depth profile. FDTD simulated $/H_y/^2$ distribution for (c) structure I and (d) structure II. (Shi et al [43]).

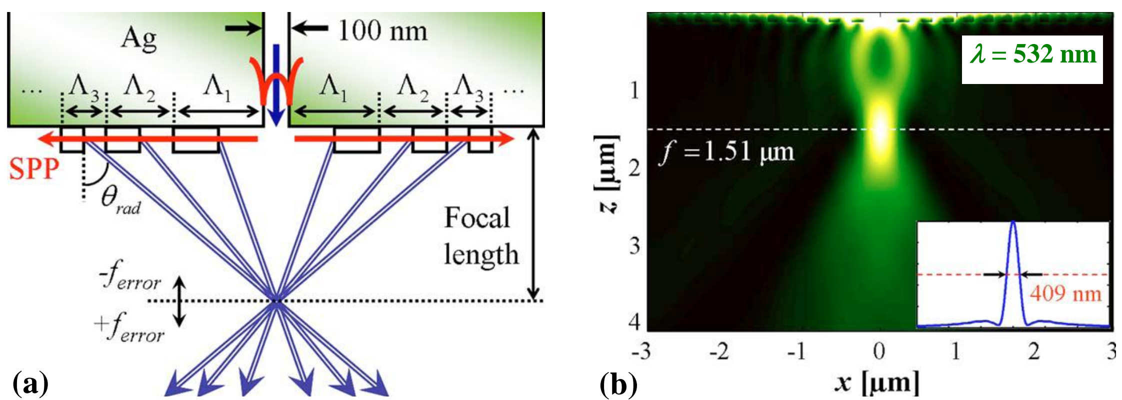

Figure 2.5 (a) Subwavelength slit surrounded by chirped dielectric surface gratings (b) The focusing intensity distribution (Kim et al [44]).

Almost all plasmonic nanostructures proposed are investigated as 2D element i.e. dimensions along third dimension are assumed to infinite. In other words, focusing characteristics along third dimension are not taken into account and focusing is essentially on a line rather than at a point. Recent work by Wang et al [45, 46] addresses this issue wherein a concept of depth-tuned 2D structures is extended to third dimension resulting in central slit surrounded by annular grooves with modulated depths. Such annular lens can focus at a point.

2.1.2 Subwavelength Structures for Beam Focusing without Evanescent Waves

Recovery of evanescent field may not be necessary in order to achieve subwavelength resolution in the far-field. It has been predicted theoretically by Berry and Popescu [47] that diffraction on a grating structure could create subwavelength localization of the light that propagate further into the far-field than evanescent waves. This was attributed to a phenomenon called *super-oscillations* wherein band-limited functions are able to oscillate arbitrarily faster than the highest Fourier components they contain.

Huang et al [48] have come with a quasi-periodic array of nanoholes in a metal screen that can concentrate optical energy into *hot spots* and form subwavelength spots at distances of a few tens of wavelengths (far-field) away from the array, under plane wave illumination. The subwavelength spots can be directly imaged by a conventional optical microscope and mapped into the far-field with high amplification. As shown in Figure 2.6(c), better resolution beyond the diffraction limit is attained, however, with the decrease in intensity of a focal spot.

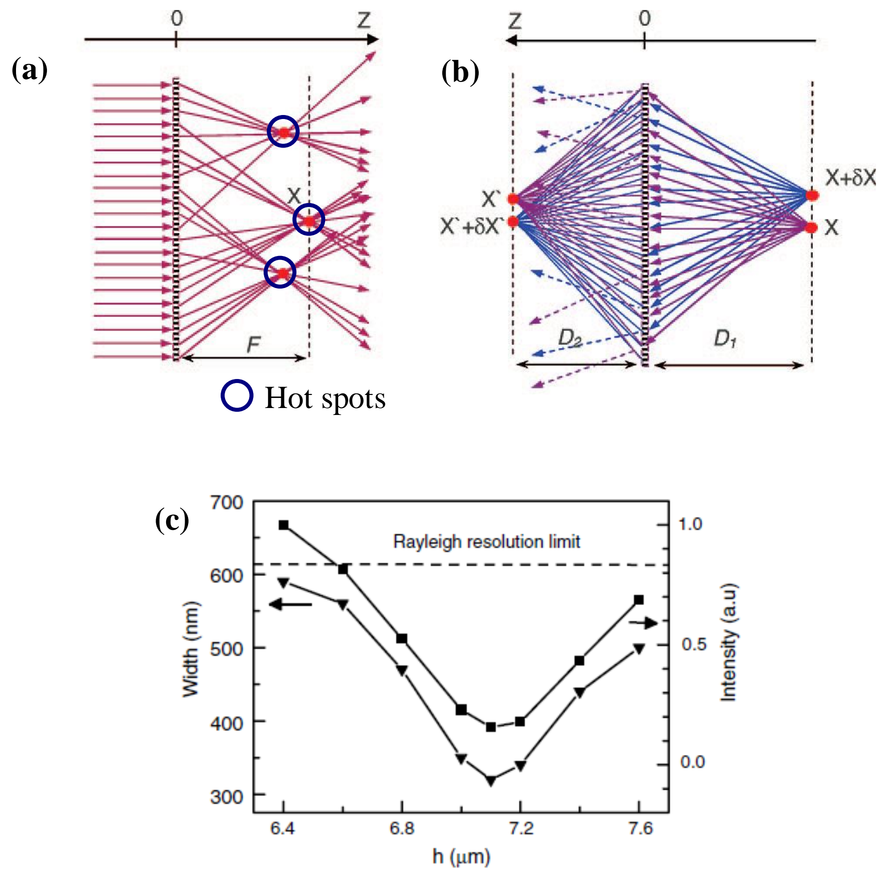

Figure 2.6 Quasi-periodic array of nanoholes acts as (a) a light concentrator producing *hot-spot* foci (b) a lens imaging two closely spaced optical point-sources. (c) Dependence of resolution and focusing intensity on a height (h) above the nanohole array. (Huang et al [49, 50]).

Utilizing super-oscillation theory, Wang et al [51] organized micro/nano fibers (MNFs) in a circle array to produce original super-oscillations and obtain a subwavelength focusing spot in the far-field as shown in Figure 2.7. The optimized MNF array was shown to obtain a subwavelength focusing spot with FWHM of 0.43λ at a distance of 9λ from the endfaces of MNFs.

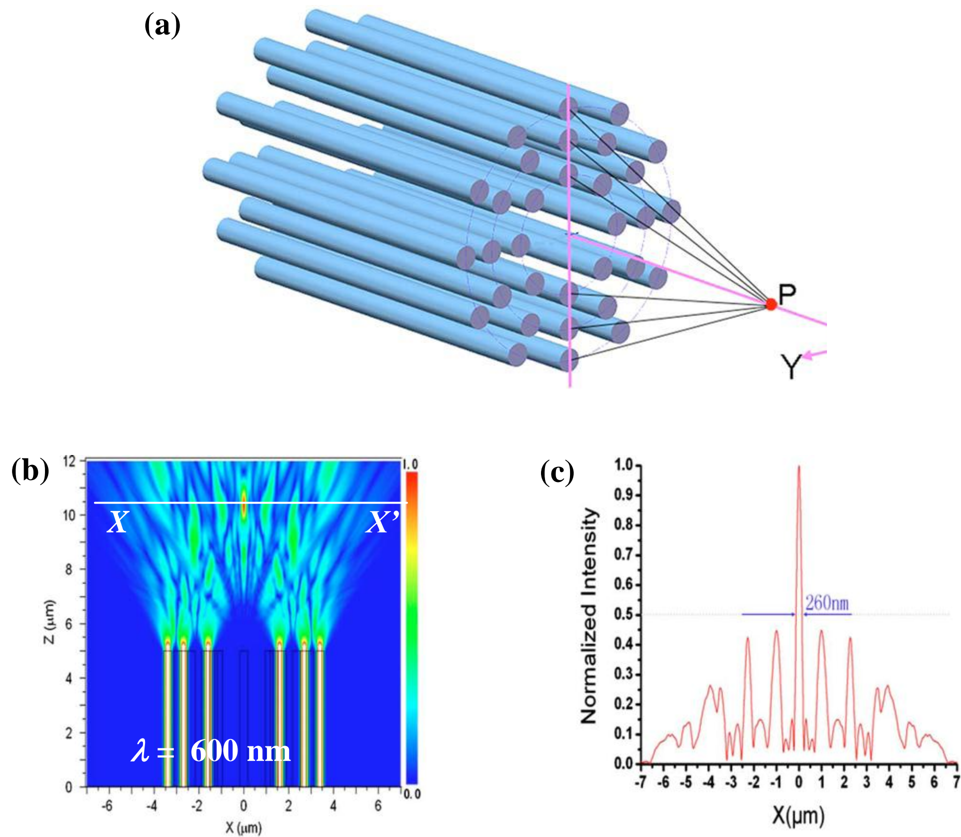

Figure 2.7 (a) Micro-nano fiber array (MNF) (b) Focusing by MNF array in the far-field (c) Subwavelength focusing characteristics of focal spot (*XX'*) (Wang et al [51]).

2.2 Fresnel Zone Plates

The Fresnel zone plate can be treated as a hologram formed by two point sources as shown in Figure 2.8. The wavefront from *P* may be thought of to be made up of a set of half-wavelength zones by spherical wavefronts with origin at *P′* and differing in radii by $\lambda/2$ (i.e. by phase π). Thus, each alternate zone acts as a source of wavelets according to Huygen's principle, which add up constructively to produce a focal point. Now, a diffractive focusing structure can be easily created by constructing concentric circles with radii defined. As shown in Figure 2.8, when alternate zones are made opaque, it is called a Fresnel or an amplitude zone plate. A positive zone plate is one with a transparent center as opposed to a negative zone plate whose center is opaque.

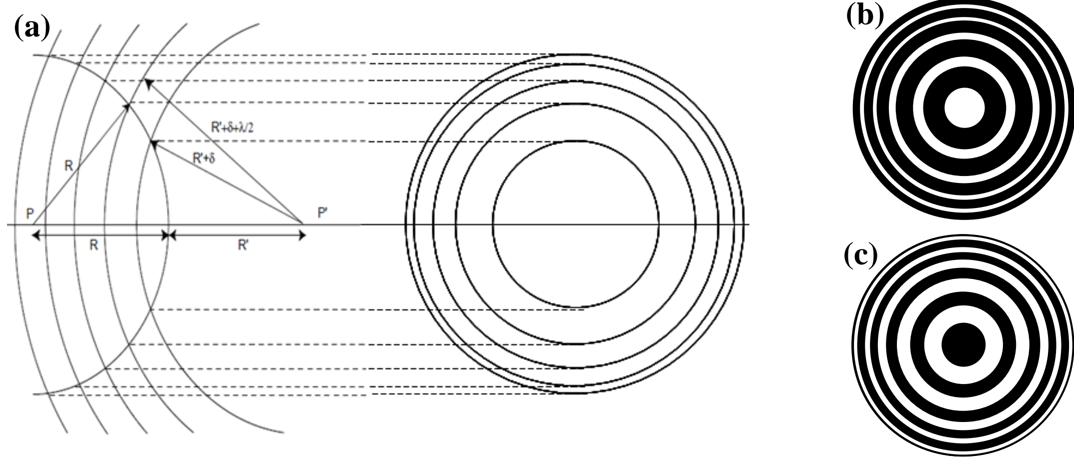

Figure 2.8 (a) Construction of Fresnel zones. Amplitude or Fresnel zone plates: (b) positive zone plate (c) negative zone plate.

2.3 Modeling of Fresnel Zone Plates

2.3.1 Scalar Approach

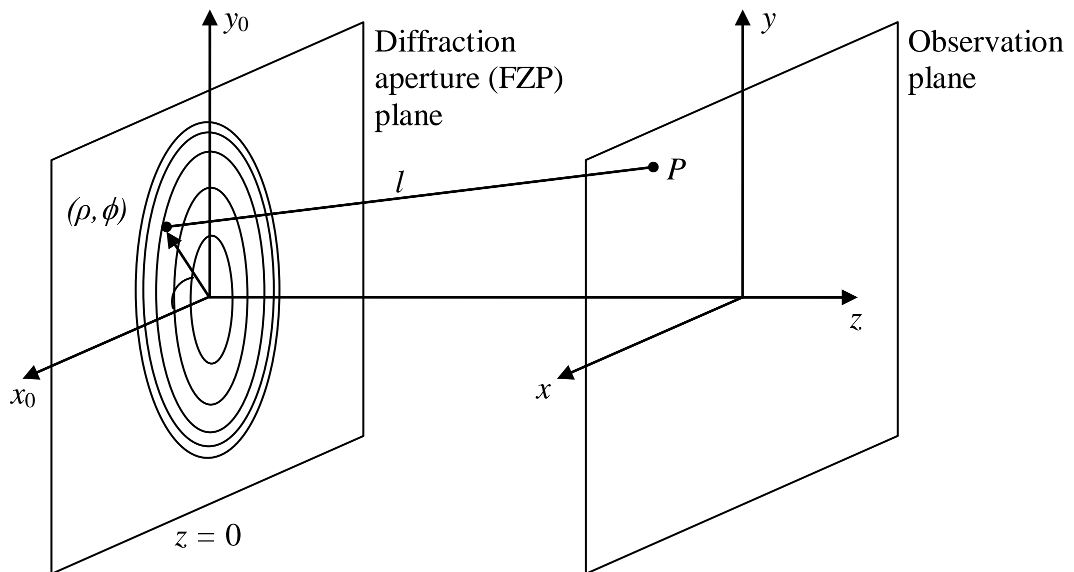

Figure 2.9 Geometry of diffraction aperture consisting of FZP and observation plane. (ρ, ϕ) are polar co-ordinates of a point in FZP plane.

Based on the basic diffraction formulations derived in *Appendix A* for an arbitrary aperture, focusing characteristics for FZPs are derived. For this purpose, the zone plate can be considered to be contained in the circular aperture as shown in Figure 2.9. The diffraction patterns of the zone plates are calculated by summation of the diffracted fields of the individual rings. Each ring is considered as the difference between two circular apertures. If F represents an integrand of the appropriate diffraction theory applied, we can write for amplitude zone plates with N Fresnel zones:

$$U(P)=\sum_{m=1}^{N-1}\int_{\rho_m}^{\rho_{m+1}}\int_{0}^{2\pi}Fd\rho d\theta \tag{2.4}$$

Similarly, we can write for phase zone plates:

$$U(P)=\sum_{m=1}^{N-1}(-1)^{m+m'}\int_{\rho_m}^{\rho_{m+1}}\int_{0}^{2\pi}Fd\rho d\theta \tag{2.5}$$

where $m' = 0$, if the first zone has a π phase shift or else $m' = 1$.

For the FZPs reported in the literature, paraxial approximations, Fresnel or Fraunhofer approximations are invoked in order to simplify the analysis. Diffraction pattern in the plane of observation depends on the distance of the observation plane from the aperture as shown in Figure 2.10.

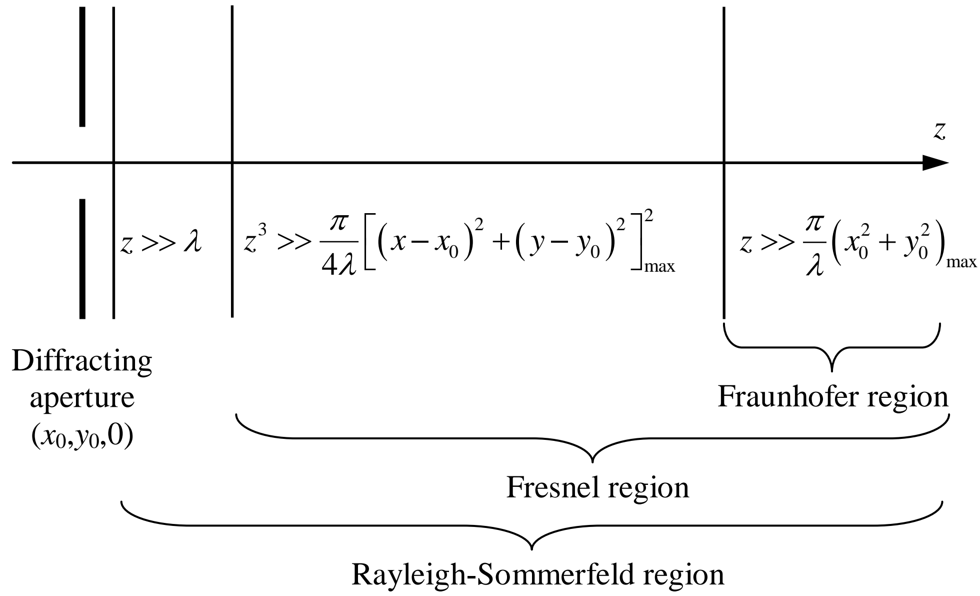

Figure 2.10 Illustration of validity regions for different scalar diffraction theories

Stigliani et al [52] used Kirchhoff's diffraction theory with Fraunhofer approximation to calculate the diffracted field from a zone plate. Subsequently, Waldman et al [53] emphasized against using Fraunhofer approximation and demonstrated that such an approximation would lead to the loss of all focusing properties of the zone plate. Further, Sun et al [54] have calculated the diffraction pattern due to FZP using a Fresnel approximation as the focal point of a FZP always falls in the Fresnel region. They have shown that the focusing properties of FZPs predicted using Fraunhofer approximations are incorrect except for the resolution defined by the Rayleigh criterion.

Rayleigh-Sommerfeld formulation (Equation (A.6)) is valid over the entire space behind the aperture. Exact solution to this integral for circular aperture was reported by Dubra et al [55]. The other work referred to the exact solution is in the paper by Osterberg et al [56]. Marathay et al [57] used this complete expression and reported on-axis irradiance at the principal focus has a $sinc^2$ distribution along the *z*-axis, a distribution usually associated with the rectangular diffracting geometries. In the region close to FZP, the secondary maxima display rectangular Fresnel diffraction

type distributions. Zhang et al [58] have claimed to derive an improved Rayleigh-Sommerfeld formula and applied to FZP analysis. However, the reported formula is not a new derivation but the exact integral form of Rayleigh-Sommerfeld formula (Equation (A.6)).

All the analyses of FZP are based on the diffraction integrals, which are the integral-form solution of the scalar Helmholtz wave equation. Here, the light wave is considered as a scalar phenomenon. The purely linear polarized field with only one electric (or magnetic) field component cannot exist owing to the Maxwell identity $\Delta \mathbf{E} = 0$. There must be an associated longitudinal field component along the propagation direction. However, the longitudinal field component can be ignored, provided the focal spot size is larger than the order of the wavelength. Usually, this condition is well satisfied for the FZPs working in the spectral regions of soft X-rays and EUV radiation.

2.3.2 Rigorous Approach

In the X-ray spectral band, zone plates are inevitably thick compared with the wavelength, so a full-wave theory is required to describe diffraction phenomenon inside the zone plate volume that determines its optical characteristics. In zone plate, diffraction analysis is based on a geometrical optical approach, which is valid under the assumption of optically thin zone structures i.e. it neglects the expansion of zone structures along the optical axis.

Rigorous solutions have been developed to address a class of high resolution and efficient zone plates, which necessarily must be optically thick, and having a high aspect ratio (thickness over the zone width). More accurate dynamical calculations of the diffraction of zone plates with high aspect-ratios were presented by using a

parabolic wave equation (PWE) [59, 60] and coupled-wave theory [61, 62]. Analytical approach based on parabolic wave equation, is more suited for illumination under X-ray regime. This is because the permittivity ε of all materials in X-ray range only slightly differs from its free-space value: (ε - 1) < 1. Physically, this causes all diffraction processes to be unidirectional and almost paraxial in character. Mathematically [63], this means that each component of the electromagnetic field $E\exp(i\omega t)$ can be represented as a modulated plane wave $E(x, y, z) = u(x, y, z)\exp(ikz)$ with the slowly varying complex amplitude $u(x, y, z)$.

For the application of coupled-wave analysis, the modulated region needs to be periodic. The zone plate pattern is subdivided into local regions, which are then approximated by infinite gratings as shown in Figure 2.11. Such an approximation is acceptable if zone plate has sufficiently large number of zones. This is because zone plate has an increasing line density, the local zone period ($\Lambda = 2dr_m$) changes slowly with the zone number m if m is large.

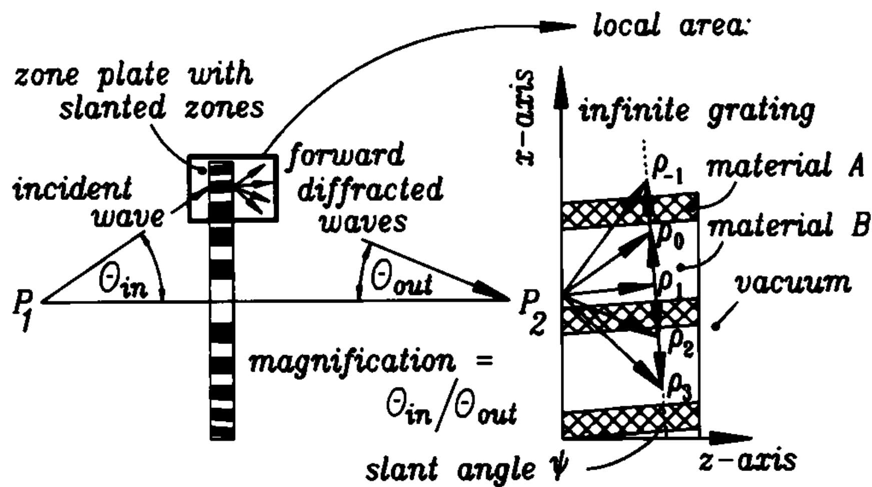

Figure 2.11 Zone plate structures approximated by an infinite grating under plane wave illumination for coupled-wave analysis (Schneider et al [61]).

There have been attempts to model diffractive or Fresnel lens in the visible regime of illumination [64-67] with a local grating theory. With this approach, a local

structure of an optical element is assumed as an infinitely extending diffraction grating. Noponen et al [65] first explicitly noted that the diffractive lens may be viewed locally as a grating. Their purpose for this approach was to improve the diffraction efficiency of diffractive lenses. Sheng et al [66] expanded the method for optimizing two-dimensional circular diffractive lenses. Recently, Ichikawa et al [68] used a simplified version of local grating theory for the modeling of one-dimensional micro-Fresnel lenses. It must be noted that the accuracy of the local grating approximations increases with the number of Fresnel zones of the lens, which is proportional to the aperture size for a given numerical aperture. However, the local grating theory becomes questionable for microlenses with only a few zones.

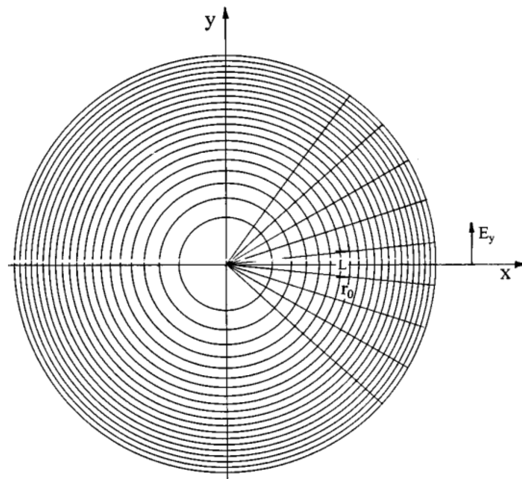

Figure 2.12 Approximate local linear grating model for diffractive lens (Sheng et al [66]).

In summary, above approach suffers from following limitations:

- Actual graded-period zone plates are approximated with a periodic diffraction grating model.
- Actual non-rectangular zone profiles are difficult to incorporate in the method.

- Unaccounted phase relations give too-optimistic estimate of the overall zone plate diffraction efficiency.

For finite size and aperiodic diffractive optical elements, Prather et al [69] developed a vector-based analysis of finite aperiodic diffractive optical elements by using a boundary integral method (BIM). The treatment has been general and both, perfectly conducting and homogeneous dielectric, diffractive optical elements are analyzed. However, the boundary integral equations are based on a suitable integral equation. This needs an exact Green's function to be derived, which can be realized for a homogeneous or discretely inhomogeneous media. Mait et al [70, 71] further demonstrated a design of binary subwavelength diffractive lens with due consideration to fabrication limitations like feature size and etch depths. Their approach was based on the combination of two approximate theories of diffraction, scalar diffraction theory and effective medium theory, and relies on the area modulation of subwavelength features. Effective medium theory allows one to predict the refractive index of a subwavelength structure while with scalar diffraction the phase transformation of a wave field is predicted. It must be noted that in these works, an analysis of one-dimensional elements is presented.

3D analysis of finite aperiodic subwavelength 2D diffractive optical elements using finite-difference time-domain (FDTD) was presented by Mirotznik et al [72]. FDTD offers several advantages over other frequency-domain techniques such as finite-element method (FEM) and boundary integral methods (BIM):

- FDTD is a direct solution of Maxwell's equations in time-domain. Consequently, it is a complete full-wave solution that contains no approximations, apart from discretization of the computational domain with Yee cells, which would prevent a correct solution from being reached. FEM and BIM can be plagued by spurious nonphysical solutions.

- FDTD is the most general in analyzing structures with variety of materials and geometries. Structures that contain inhomogeneous, lossy, or even anisotropic material properties can be easily handled.
- The memory requirements of the FDTD are significantly less than required by other rigorous methods.

Recently, using FDTD method, Fu et al [21] proposed the use of Ag based FZP for superfocusing in the visible wavelengths. However, structure design simply follows conventional design principles of FZP with no consideration to plasmonic coupling to output radiation.

2.4 Structures Based on FZP

In order to improve FZP performance i.e. to improve diffraction efficiency, resolution, minimize the presence of side-lobes and achieve ease of fabrication, various designs, based on FZP, are proposed by several authors. This section takes an overview of diffractive structures based on FZP addressing specific limitations of FZP.

1. Photon sieves

Kipp et al [73] proposed an element called photon sieve based on FZP structure. Photon sieves exhibit higher resolution and improved image contrast compared with traditional diffractive optics such as FZP. A photon sieve is composed of pinholes arranged in the radial direction such that their center locations correspond to the open zones of a traditional FZP. Along azimuthal direction, the centers of the pinholes are randomly located. As shown in Figure 2.13(a), this arrangement makes the portion of the light diffracted from the pinholes interferes constructively at a focal point. The focal spot produced by a FZP is due to almost equal contribution by its zones. However, such contribution drops abruptly to zero beyond the outermost ring

which leads to strong intensity oscillations in the diffraction pattern leading to appearance of side-lobes along with central maximum in the focal plane. With a photon sieve, the number of pinholes per zone can be readily adjusted to yield a smooth transition which minimizes side-lobes (see Figure 2.13(b)). Further by introducing randomness in the arrangement of the pinholes on each zone, higher order foci can be reduced (see Figure 2.13(c)). Other advantage offered by photon sieve is that, for a given resolution, minimum feature size (hole diameter) may be greater than the required for FZP with the same resolution. In addition, a photo sieve can be easily fabricated on standalone films as the holes of the sieve do not have connected regions.

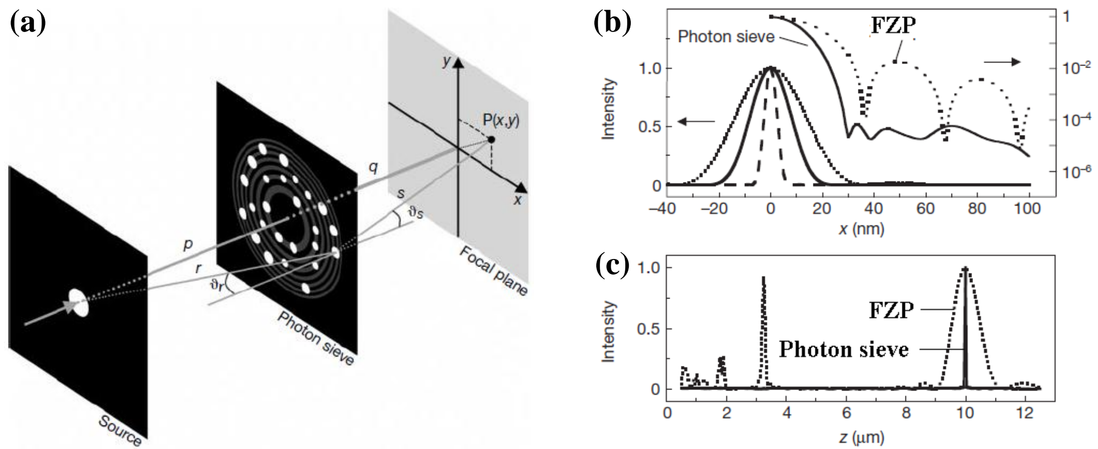

Figure 2.13 (a) Imaging scheme using photon sieve. (b) Focal spot intensity pattern by photon sieve and FZP. Note reduced side-lobes and improved spot-size. (c) Intensity distribution along propagation axis showing suppressed higher-order foci with the use of photon sieve. (Kipp et al [73]).

Cao and Jahns [74, 75] provided an individual far-field model for photon sieve. In this model, the far field of a circular pinhole is analytically described by the airy-pattern distribution. Menon et al [76] has demonstrated the first lithography results that use high numerical-aperture photon sieves as focusing elements in a scanning-optical-beam-lithography system. Here, photon sieve with minimum pinhole diameter of 500 nm was used under illumination of 400 nm wavelength. The photon sieve design is

based on a scalar diffraction theory. All the photon sieves reported so far work in the far-field region and their minimum hole diameter is larger than the incident wavelength.

Fu et al [77] proposed a nanopinhole based plasmonic structure (NPPS) for achieving a super-lens effect by using sub-wavelength pinholes on *Au* film coated on the glass substrate. However, no comparison was made with the corresponding FZP design. Interestingly, apart from the main focal point additional foci are reported along the propagation direction. This is in contrast with the photon sieves used in the far-field focusing wherein higher order foci are suppressed.

2. Modified Fresnel zone plates

The focal spot size by FZPs is limited by the smallest achievable outermost zone width with available fabrication techniques. In order to overcome the fabrication constraints, Simpson et al [78] suggested the use of a centrally obstructed zone plate, which mainly reduces the effect of a zero-order radiation and improves resolution. However, the system is more suited for a point object than extended objects and the central obstruction leads to a loss in the transmitted energy. In the same paper, they proposed a concept of composite zone plate which is made up of a small zone plate and the outer part of a large zone plate with equal outermost zone widths (see Figure 2.14(a)) and resolution obtained was about twice as good when the maximum number of outer zones is used. The main drawbacks are the long focal length making instrument long and the presence of side-lobes blurring the image

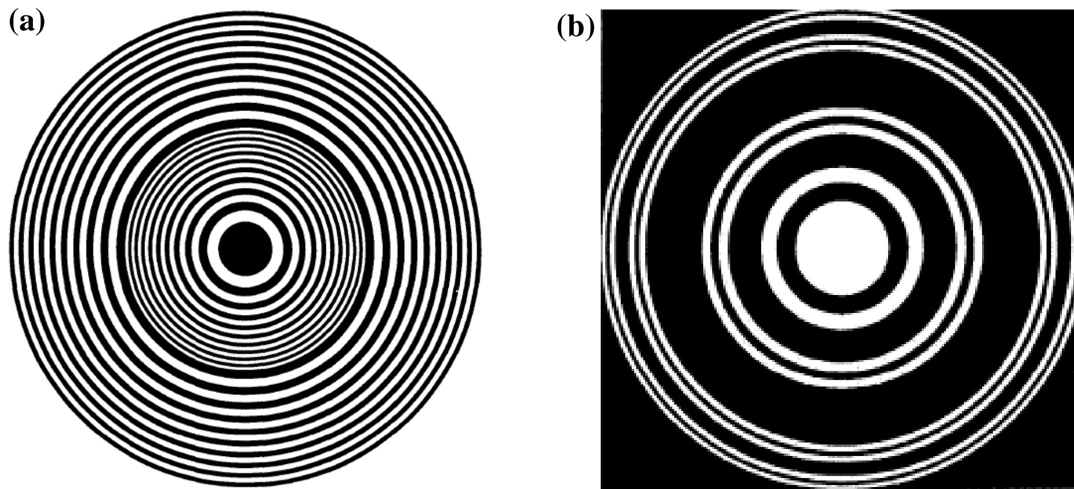

Figure 2.14 (a) Composite FZP proposed by Simpson et al [78] (b) Fractal zone plate structure proposed by Saavendra et al [79].

Motivated by the concept of photon sieves, Cao et al [80, 81] proposed to modulate zones of the FZP in order to produce a Gaussian focal spot because a focused Gaussian beam has the advantages of no side-lobes, circular symmetry, long focal depth, and good beam quality. With a minimum zone width of 30 nm, they have shown that a Gaussian focal spot with a beam width of 7 nm can be produced for 2.4 nm illumination. It must be noted that the modified FZP design is based on Rayleigh-Sommerfeld formulation (Equation A.7). The design is more suitable than the photon sieve owing to its circular symmetry, long focal depth and good beam quality.

Increase in the depth of field and reduction in the chromatic aberration can be achieved by replacing the periodic function used in the generation of a FZP by a fractal structure [79]. Fractal zone plates resemble conventional zone plates with some missing clear zones as shown in Figure 2.14(b). Such fractal zone plates show unique behavior of multiple foci with internal fractal properties along the optical axis [82]. Thus, the fractal zone plates offer the flexibility to design process to modify the pattern of multiple foci and their relative amplitudes.

3. Volume zone plates

Diffracted light from many FZPs can be effectively coupled together to enhance the intensity at the focal spot. Using this concept, in order to improve diffraction efficiency of FZPs, Srisungsitthisunti et al [83, 84] proposed *volume zone plates*. A volume Fresnel zone plate is essentially a collection of a number of zone plates or modified zone plates in a volume of a suitable material, such as fused silica (see Figure 2.15). Each of this zone plate should be carefully designed according to its position along the optical axis. This is because a volume zone plate should satisfy focal point matching and phase matching so that all the zone plates focus light exactly at the same focal point.

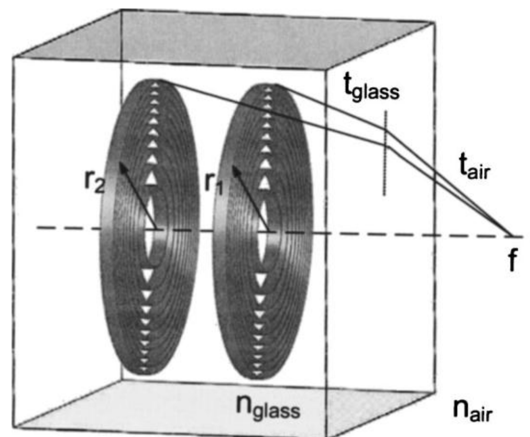

Figure 2.15 A volume zone plate in fused silica [83].

2.5 Polarization Issues in Diffractive Optical Elements

Polarization of an illumination source is an important factor while analyzing the performance of subwavelength diffractive optical elements. From polarization point of view, for diffractive lenses, rigorous design approaches were concentrated on TE and TM state of polarization.

Noponen et al [64, 65] developed a design procedure for cylindrical diffractive lenses using a rigorous local grating model and optimized the diffraction efficiencies. Hirayama et al used boundary element method (BEM) to analyze diffractive cylindrical lenses of continuous profile and with discrete levels. The response of these lenses was calculated for TE and TM polarization and higher diffraction efficiencies were noted with continuous profile lens. The emphasis of the work was on developing a BEM method and no optimization of the design was carried out. Finlan et al [85] and Sheng et al [66] proposed a design model for circular diffractive lenses with high numerical apertures. They used the local grating model to optimize the profiles of various grating periods simultaneously for both TE and TM polarization. Schmitiz et al [86, 87] presented a design concept which yields the performance of the lens independent of incident polarization (TE or TM). In a nutshell, the emphasis of all the work done was to optimize the design in order to improve diffraction efficiency regardless of incident polarization. As lens designs were for far-field focusing, no consideration was given to analyze focal characteristics like depth of focal, focal spot size etc.

In contrast to the research focused on achieving polarization independent diffractive element, work by Hasman et al [88] demonstrated a polarization dependent diffractive lens. Required geometrical phase is achieved by discrete orientation of the local subwavelength grating as shown in Figure 2.16. The focusing structure is a converging lens for incident right-hand circularly polarized beam state, and a diverging lens for incident left-hand circularly polarized beam. The implementation of a subwavelength gratings in the visible domain is difficult, however, at longer wavelengths (λ = 10.6 μm) such concept has been successfully implemented [89].

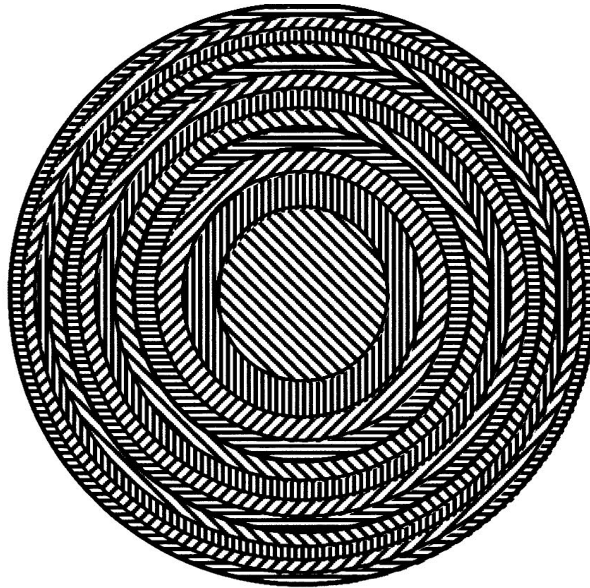

Figure 2.16 Polarization dependent diffractive lens formed by unique orientation pattern of subwavelength gratings. Illumination wavelength, $\lambda = 10.6$ μm. [88]

Feng et al [90] analyzed finite, subwavelength diffractive lenses by using a 2-dimensional FDTD method. The investigation was carried out for 10 μm illumination wavelength and for TE and TM polarization states. The design approach was based on the work by Farn et al [13] wherein subwavelength structures were considered as materials of an equivalent index. As shown in Figure 2.17, binary subwavelength lenses were found to be more sensitive to the polarization than the continuous profile lenses owing to vector diffraction nature, multiple scattering and presence of evanescent waves. Further, diffractive lens design is shown to be tailored in order to attain an extended depth of focus which is suitable for high precision optical alignment systems [91].

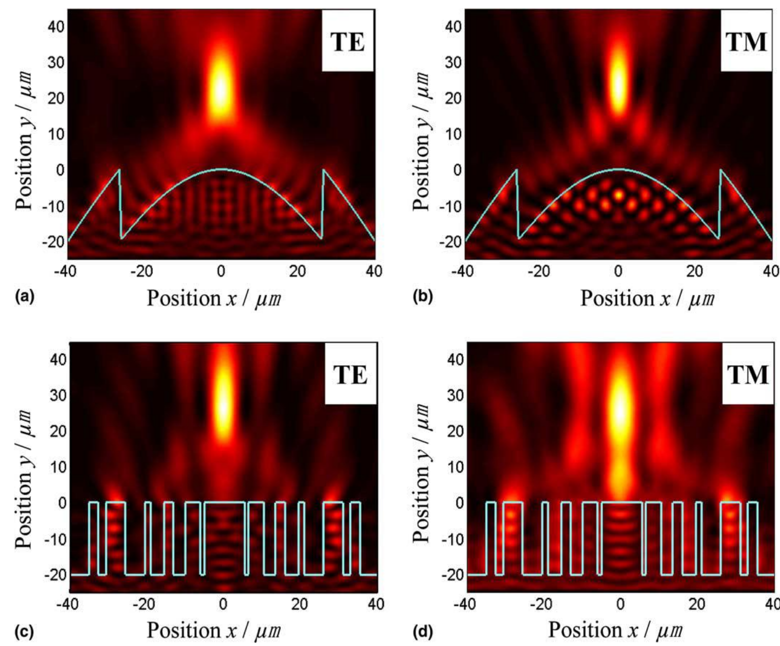

Figure 2.17 Focusing characteristics of a continuous profile diffractive lens (a) and (b); and of a binary subwavelength diffractive lens for TE and TM polarization states. Illumination wavelength, λ = 10 μm [90].

2.6 Summary

From the survey of the literature, following are issues need to be addressed:

1. Plasmonic structures as well as structures based on artificial left-handed materials (meta-materials) show promise in achieving subwavelength resolution at optical wavelengths. However, such structures are often difficult to modulate so as to get focusing out of the surface. Further, fabrication of meta-materials and plasmonic structures is challenging.
2. Fresnel zone plate structure has been studied extensively over the wide range of electromagnetic spectrum. However, little consideration has been given on focusing to achieve ultra-short focal lengths. Focusing performance of zone plates with focal lengths in the near-field needs to be investigated. Such zone

plates may open up myriad of interesting properties due to presence of subwavelength features and high numerical aperture.

3. Most of the models developed to ascertain the focusing characteristics are based on scalar diffraction theories which are developed under Kirchhoff's boundary conditions. Rigorous theories are proposed for design of diffractive lenses with subwavelength features. However, they are limited to 1D analysis in the far-field. In the optical wavelengths, behavior of the Fresnel zone plate with subwavelength features needs to be explored and a complete vectorial analysis like FDTD seems to be suitable choice for such analysis.
4. There is a very little consideration given to the vector nature of the illumination i.e. polarization while studying Fresnel zone plates. For a high NA Fresnel zone plate structure with short focal lengths, polarization may play a critical role in defining focusing profile.
5. In addition to theoretical analysis, issues with the fabrication of both type of zone plates i.e. amplitude and phase zone plate need to be investigated. This is important as high NA zone plates operating in the near-field will have subwavelength features.

The thesis attempts to address above issues as discussed in the following chapters.

Chapter 3

Near Field Focusing Behavior of Fresnel Zone Plates (FZP)

In this chapter, the focusing characteristics of FZPs in the optical wavelength with different metal coatings are studied in the near-field regime by using a finite-difference time-domain (FDTD) method. Further, the use of phase zone plates in glass to achieve a high focusing intensity is investigated. For analysis in this chapter, the illumination source is assumed to be linearly polarized.

3.1 Influence of Metallic Coating on the Diffraction Characteristics of FZPs

In this section, we examined the subwavelength focusing characteristics of metal-coated FZPs. Figure 3.1 shows the schematic of a negative-type FZP (i.e. with central opaque zone – metallic coating) considered in the analysis. Incident illumination is linearly polarized with electric field vector directed along the *x*-axis. FZP is located in the *xy* plane and *z*-axis is the optical axis.

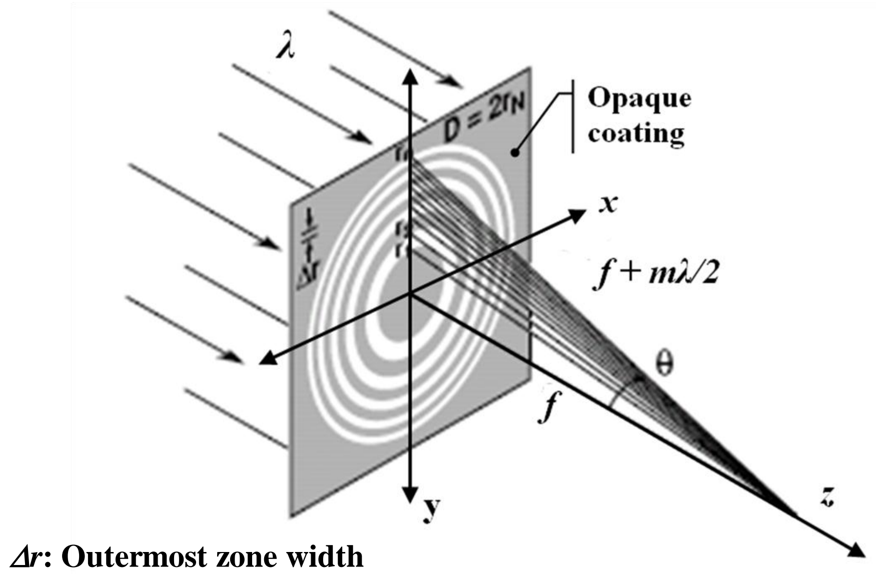

Figure 3.1 Construction of amplitude Fresnel zone plate (adapted from [92]).

The dimensions of the metallic-coated FZPs are obtained from the classical equation used in designing conventional FZPs [92] , written as:

$$r_m = \sqrt{m\lambda f + \frac{m^2\lambda^2}{4}} \tag{3.1}$$

where m (= 1, 2, …..) is an integer, r_m is the radius of the mth zone, f is the first order focus of the zone plate and λ is the operating wavelength. It must be noted that Equation (3.1) is based on classical far-field optics wherein focusing phenomenon is adequately explained based on the interference of diffracted traveling waves. For FZPs with focal lengths comparable to the incident wavelength and with the presence of subwavelength features, classical FZP analysis is not applicable in this regime. Under such conditions, focusing is influenced by presence of the near field. Hence, Equation (3.1) cannot be assumed to be exact design rule for such FZPs. However, in this work, as a reference, Equation (3.1) was used to design FZP and focusing behavior of such classical structures in the near field regime was investigated using a finite-difference

time-domain (FDTD) method. FDTD method is suitable as it provides rigorous vectorial solution for a wide range of materials and for arbitrary geometries of subwavelength dimensions.

The Equation (3.1) is usually simplified when $f >> m_{\max}\lambda$ as:

$$r_m = \sqrt{m\lambda f} \tag{3.2}$$

Differentiating Equation 3.2 by m, zone width can be obtained as:

$$w = \sqrt{\frac{\lambda f}{2r_m}} \tag{3.3}$$

Equation (3.2) is a very popular approximation in designing FZPs. However, validity of such approximation must be assessed in the present analysis. For this purpose, we calculate deviation between ideal phase profile (by Equation (3.1)) and approximated (paraxial) phase profile (by Equation (3.2)). The corresponding phase functions, with a wave-vector $k = 2\pi/\lambda$, can be written as:

$$\begin{aligned} \Phi_{ideal} &= k\left(f - \sqrt{f^2 + r^2}\right) \\ \Phi_{approx} &= -k\left(\frac{r^2}{2f}\right) \end{aligned} \tag{3.4}$$

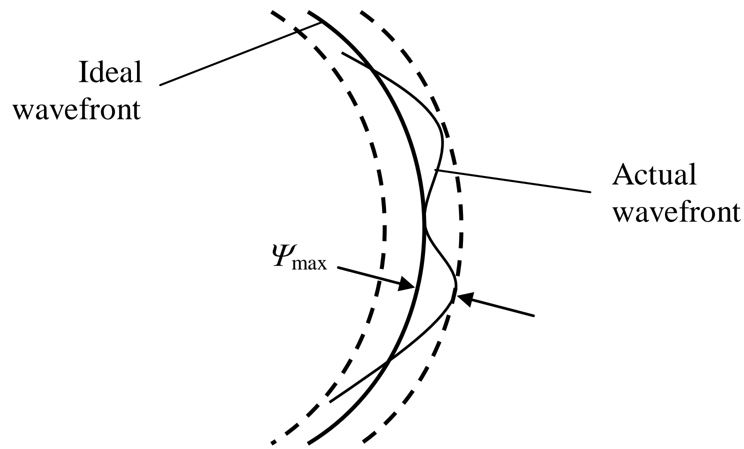

Maximum wavefront deviation (Ψ_{max}) ≤ $\lambda/4$

Figure 3.2 Illustration of Rayleigh criterion showing tolerable wavefront deviation for the ideal imaging system.

According to the Rayleigh criterion the lens can be considered as ideal if the maximum path length deviation is smaller than $\lambda/4$ [9] as shown in Figure 3.2.

$$\left|\Phi_{approx} - \Phi_{ideal}\right| < k\frac{\lambda}{4} \tag{3.5}$$

Using Equations (3.4) and (3.5), a limiting condition on acceptable combination of diameter of the FZP and corresponding focal lengths can be obtained as:

$$\frac{r^2}{2f} + f - \sqrt{f^2 + r^2} = \frac{\lambda}{4} \tag{3.6}$$

Figure 3.3 shows acceptable focal length and maximum FZP diameter combination with the use Equation (3.6) for illumination wavelength of 633 nm. It can be deduced that for focal lengths of 0.5 μm and 5 μm, FZP diameter must not be larger

than 1.49 μm and 7.53 μm respectively to use Equation (3.2) for the radii calculations. However, it can be easily seen for 0.5 μm focal length it is impossible to have any zone within 1.49 μm diameter. Hence, in our analysis, we use exact Equation (3.1) for the design of FZP instead of using approximation.

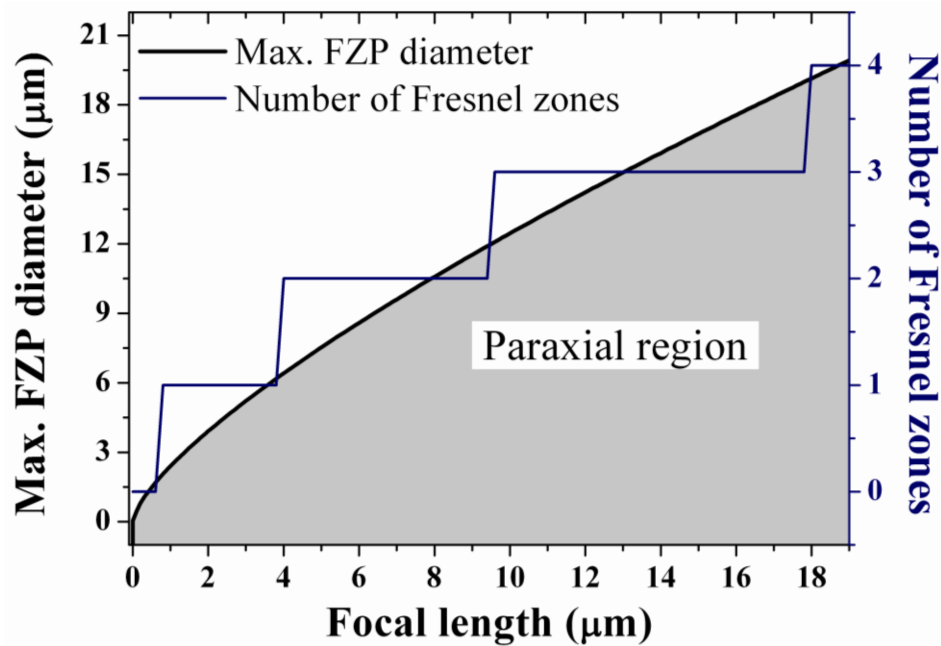

Figure 3.3 Plot of maximum FZP diameter and corresponding number of Fresnel zones as a function of the focal length under paraxial approximation. Illumination wavelength is 633 nm.

The focusing characteristics of the metal-coated FZPs are then analyzed by a 3-dimensional finite-difference time-domain (FDTD) method. All FDTD simulations were carried out using a commercial FDTD solver (Lumerical Inc., Canada). In the calculations, the mesh size along each axis was set to at least 10 points per smallest structure size. This ensures that at least 20 points per wavelength can be obtained. Plane wave source was used for illumination and perfectly matching layer was applied as the boundary condition. Dielectric properties of materials are defined based on parameter values in [93].

The role of SPP in the sub-wavelength focusing characteristics of metal coated FZPs is studied by using different type of metal coatings. Figure 3.4 plots the electric field intensities of metal-coated (i.e., *Ag*, *Au*, *Al*, and *W*) FZPs with focal length, f, number of zones, m, and illumination wavelength, λ, set to 0.5 μm, 8, and 633 nm respectively. The thickness of all the metallic coatings is assumed to be equal to 300 nm. It is observed that the magnitude and profiles of electric field intensity emitted from FZPs with different metallic coatings are similar. However, the electric field intensity is slightly lower for the case with *W* than that with *Ag*. This may be due to the relatively large surface absorption of *W* film at the visible wavelength. As *W* will not support SPP in the visible wavelength [94] and all the metal-coated FZPs exhibit similar diffractive efficiency, this implies that the mechanism of near-field focusing is independent of the choice of metals. Hence, the above calculations showed that the superfocusing phenomenon observed in metal-coated FZPs cannot be caused by SPP.

As shown in Figure 3.4, FDTD analysis predicted focal lengths longer than the designed value used in Equation (3.1) for all the metal-coated FZPs. It is noted that the depth of focus (DoF) obtained from FDTD method was found to be much larger than that of its designed value (i.e., DoF = $\pm\Delta r^2/\lambda$ where Δr is the outermost zone width of the FZPs). In the work of Fu et al [21] , the shift of focal length and DoF in FZPs from their designed values is attributed to the coupling of SPP wave through the cavity mode.

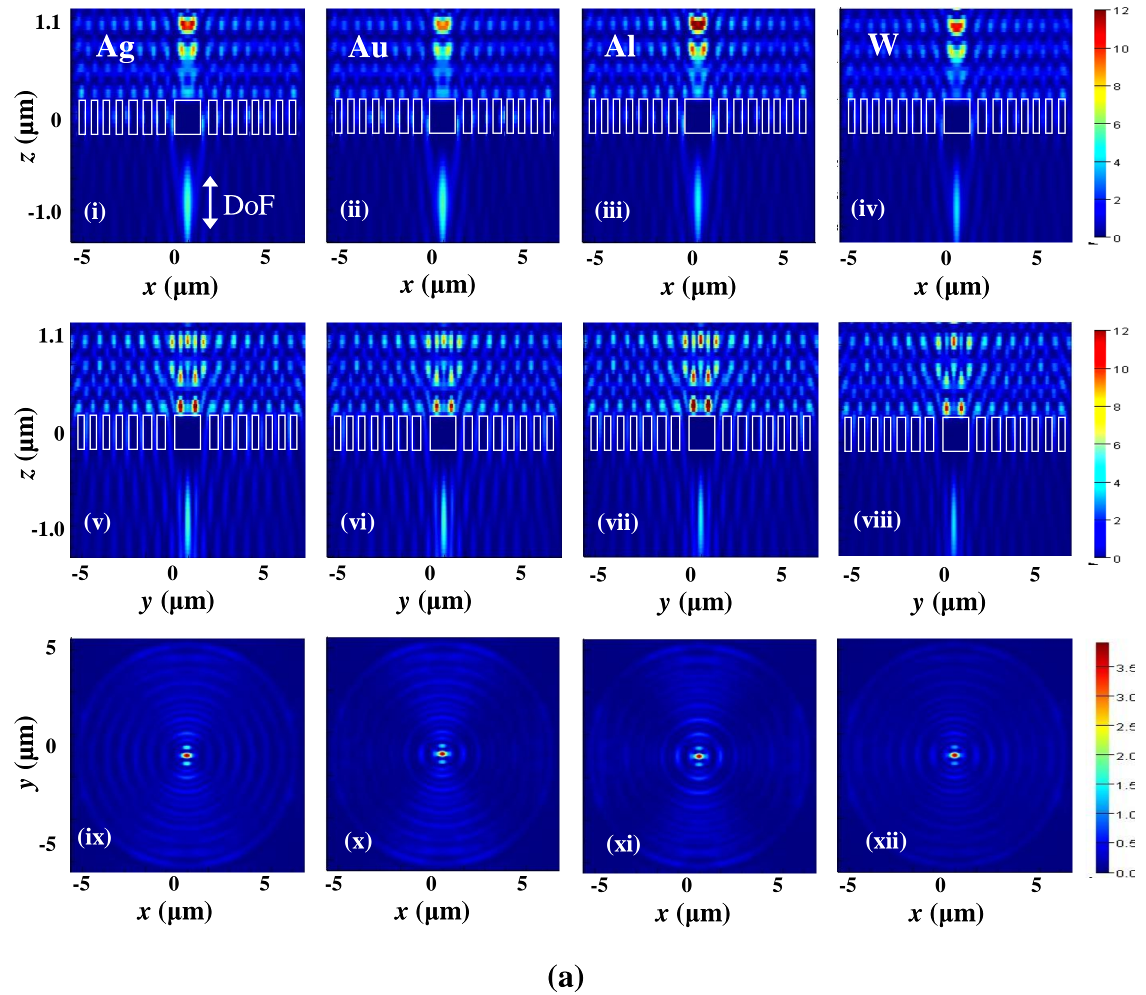

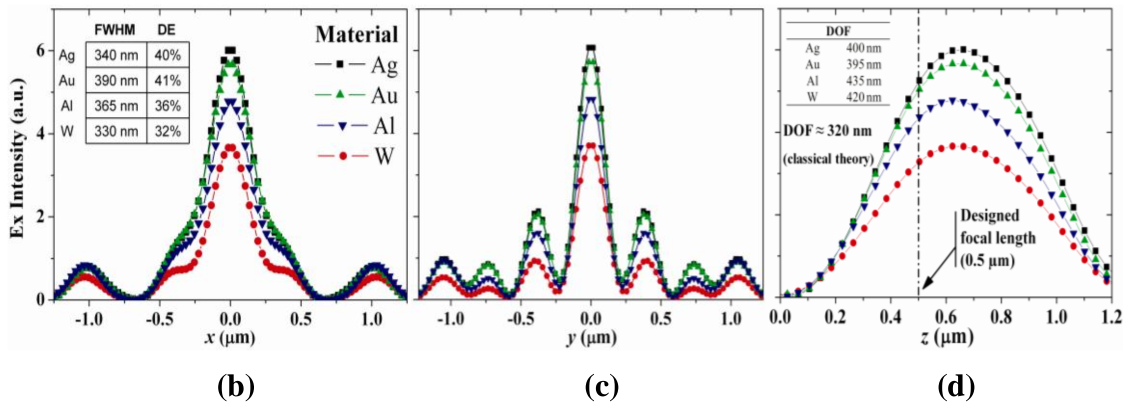

Figure 3.4 (a) Plots of intensity distribution of the transmitted electric fields in *xz* plane($y = 0$): (i)-(iv); *yz* plane ($x = 0$): (v)-(viii); and *xy* ($z = f_c$): (ix)-(xii). Plots of focal spot intensities along (b) x ($y = 0$, $z = f_c$) (c) y ($x = 0$, $z = f_c$) and (d) z ($x = y = 0$) directions. f_c is the focal length obtained from the FDTD simulation. The white boxes drew in (a) are the cross section of the metal coatings.

However, it is observed that the underestimation of focal lengths and DoF occurred for all the materials including *W* (i.e., *W* do not support SPP). Hence, it can be concluded that surface plasmon wave has no role in the shift of focal length and DoF [95].

3.2 Focusing Characteristics of FZPs

From the above calculations, it is observed that the use of FZPs to achieve near-field focusing exhibits characteristics that are different to those of conventional zone plates [95]: There are 1) deviations in the estimation of focal length, *f*, and depth of focus, DoF, from classical theory, i.e., Equation (3.1), and 2) suppression of higher order foci. These focusing characteristics of near-field FZPs are discussed further in the following sub-sections.

3.2.1 The Influence of Zone Numbers on the Focal Length of FZPs

Figure 3.5 plots the shift of focal length (i.e., difference between the FDTD calculation and designed focal length) as a function of the designed focal lengths for the *Ag* coated FZPs with different *N* (= 4, 8 and 12). It is observed that the shift increases with the decrease of the designed focal length. In addition, the shift reduces with the increase of *N* especially for the case with short designed focal length. Figure 3.5 also plots the shift of focal length for *W*-coated FZP with *N* values of 8 and 12. It is noted that the corresponding shift of focal length decreases with the increase of *N* so that both *Ag* and *W* coated FZPs have similar diffraction characteristics. However, it is found that the DoF is less dependent on the zone number.

Focal length of FZP is governed by phase-shifts through successive zones. As per design the rule given by Equation 3.1, phase shift of π is necessary to achieve focusing at the designed focal length. However, under illumination of subwavlength zones, evanescent field are generated and these fields couples with emerging waves from the zones. Thus, phase of waves at the exit surface is not equal to the phase of waves assumed while deriving the Equation 3.1. Hence, the constructive interference would not occur exactly at the designed focal length. However, under high NA focusing conditions, it is difficult to meet the constructive interference at distances less than the focal length. Hence, focusing occurs at distances higher than the designed value of the focal length.

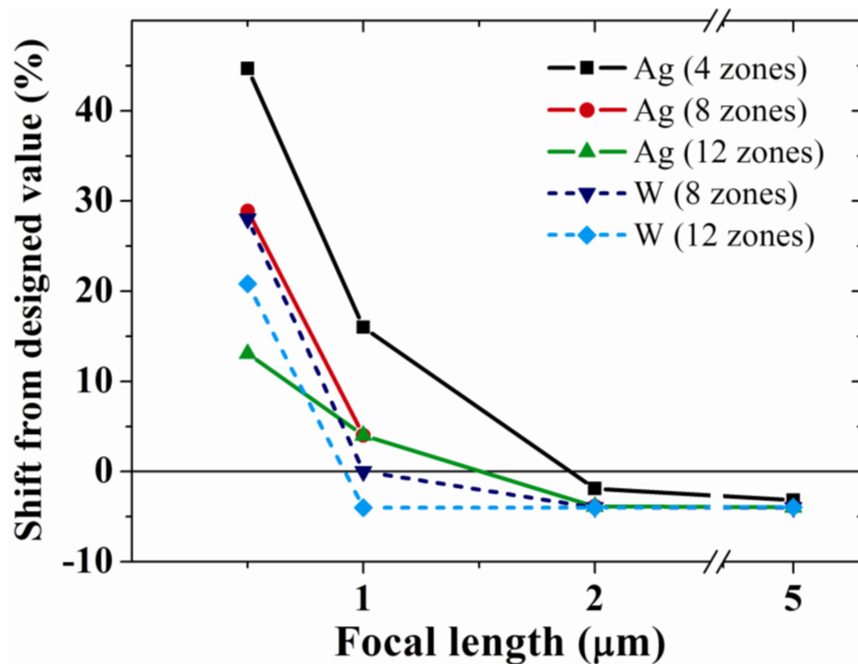

Figure 3.5 Shift of focal length (from its designed values) versus designed focal lengths (i.e., 0.5 µm, 1µm, 2 µm and 5 µm). It is assumed that the wavelength of incident plane wave is 633 nm and thickness of all metal films is 300 nm.

It is noted that the increase of zone number (i.e., increase of obliquity to the diffracted field at focus) reduces the shift of focal length even though there is an

increase of NA. This is because the increase of obliquity reduces the influence of evanescent fields so that more number of zones may average out the effects of evanescent fields. In addition, the presence of absorbing metal film greatly reduces the influence of evanescent fields. Hence, the increase of zone number leads to the reduction of focal length shifts. For FZPs with focal length of 0.5 μm, the shift in focal length is reduced from 45% to 15% when the zone number is increased from 4 to 12. Therefore, the shift in focal length from its designed value is due to the omission of interference effects between the diffracted evanescent and incident waves in the derivation of Equation (3.1) [96].

As the focal length is increased (i.e. as focal point approaches the far-field) the focal shift error is reduced. But, the focusing is observed at a distance shorter than the designed focal length (i.e. negative focal shift error). The phenomenon can be treated analogous to the focal shifts noted with circular apertures which were numerically investigated in far-field domain first by Osterberg et al [56]. The amount of focal shits in these cases is mainly governed by diffracting aperture, focal length and wavelength. As noted by Li et al [97], the focal shift is a consequence of the combined effects of interference of Huygens wavelets from all points on the incident wavefront and the inversed square law of radiation that cause the irradiance maximum to increase and shift toward the aperture.

3.2.2 The Influence of Metallic Coating Thickness on the Focal Length and DoF of FZPs

The analysis of conventional zone plates is typically based on the assumption that the opaque zones have a zero thickness. However, the metallic coating of FZPs used for subwavelength focusing has a finite thickness which is comparable to the focal length.

Hence, there is a need to analyze the influence of coating thickness on the focusing behavior of FZPs. In our study of *Ag*-coated FZPs, FDTD simulations were carried out using Ag film thickness varying from 100 to 400 nm. The zone plate is designed to have 0.5 μm focal length and 8 zones. Figure 3.6 depicts the transmitted electric field intensity from the FZPs with various thickness of *Ag* along z and x (y direction is at the focal plane) directions. The inset of Figure 3.6(a) plots the focal length and DoF as a function of the thickness of *Ag*. It is observed that the deviation of focal length (from the designed value) reduces with increasing *Ag* thickness. The deviation may be due to the presence of strong coupling of evanescent fields in the thin *Ag*-coating. On the other hand, DoF increases with the thickness of *Ag*-coating. This is because the increase of *Ag*-coating thickness is equivalent to the increase of thin metal layers (i.e., as the number of thin layers stacked together to form the metallic coating). Hence, each thin metal layer contributes differently to the diffraction of evanescent waves along the z-direction. As the focusing planes of each thin layer do not coincide, the resultant focal spots will be smeared along the z-direction so that the DoF is increased. The inset of Figure 3.6(b) shows the intensity and full-width half-maximum (FWHM) of the focal spot versus the thickness of *Ag*. It is observed that the intensity (FWHM) of the focal spot increases (decreases) with the decrease of film thickness. This is because when film thickness reduces, coupling between evanescent fields on both sides of the films is enhanced such that the focusing intensity is improved.

Consequently FZPs with thin metallic coating have the advantages of better spatial resolution and larger diffraction efficiency; however, the actual focal length of FZPs deviates more from the designed focal length.

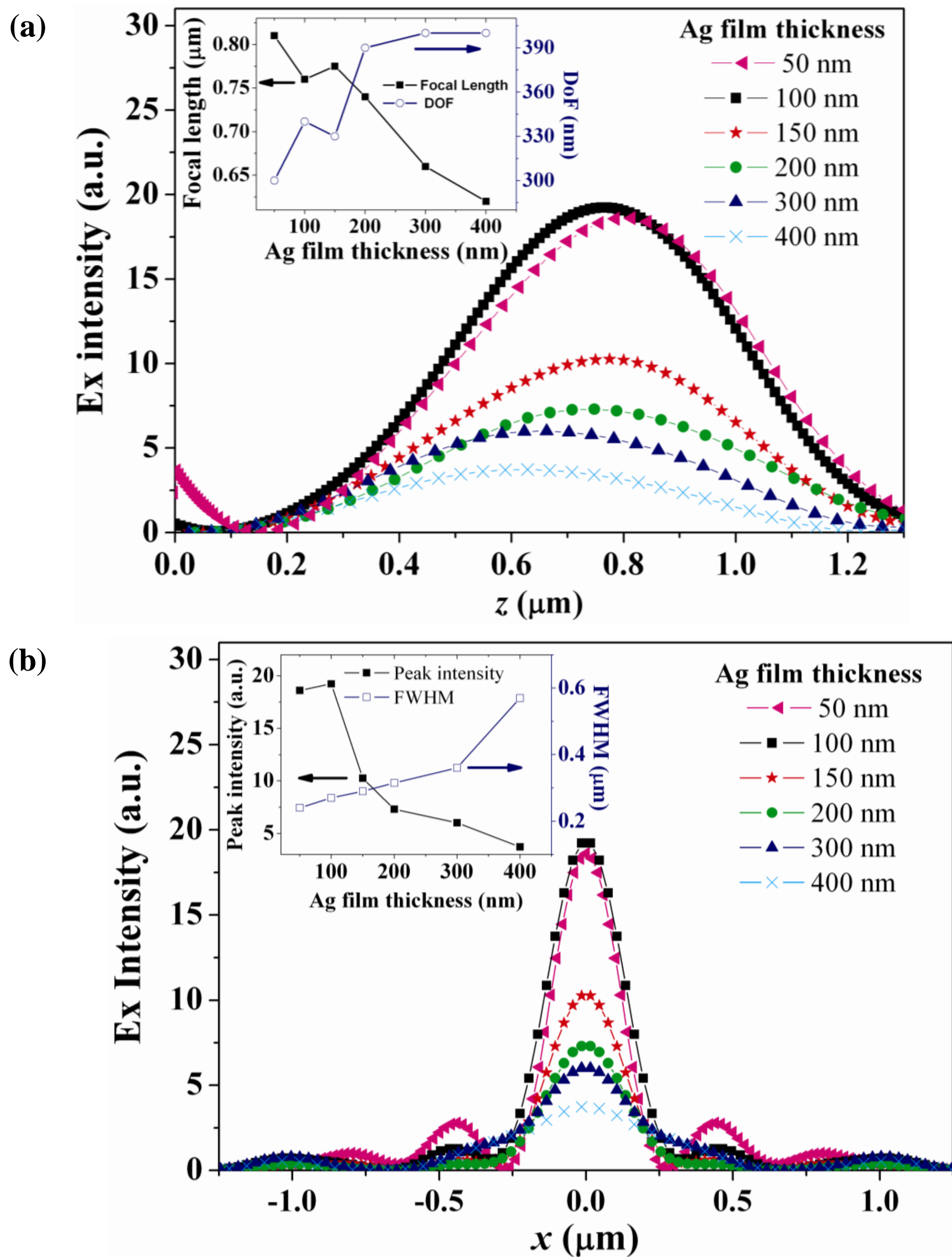

Figure 3.6 (a) Profile of electric field intensity (in a.u.) along the z ($x = y = 0$) direction. The inset shows focal length and DoF versus *Ag* thickness. (b) Profile of electric field intensity (in a.u.) along x ($z = f_c$) direction. Inset plots the peak intensity and FWHM of the focal spot versus film thickness. The FZPs have focal length of 0.5 μm under the illumination of 633 nm plane wave.

3.2.3 Suppression of Higher Order Foci

Conventional zone plates (i.e., $f >> \lambda$) are known to show additional foci due to the influence of higher diffraction orders. However, the analysis performed in Section 3.2.2 did not reveal any higher order foci – only one focus point is observed during near-field focusing. The suppression of higher order foci may be due to the obliquity factor in large NA zone plates. This is because zone plates with large NA minimize the light from the outer zones diffracted to the regions near to the center of the zone plates. Hence, higher order foci cannot be supported. Similar observations have been reported with large NA zone plates [98, 99]. A simple phase analysis would reveal the suppression of higher order foci from the metal-coated FZPs. Phase difference, Δ_m, from the mth zone boundary at any point on the z-axis can be written as

$$\Delta_m = \frac{\sqrt{r_m^2 + z^2} - \sqrt{r_{m-1}^2 + z^2}}{\lambda/2} \tag{3.7}$$

The total phase difference, Δ, at a point on the z-axis can then be calculated by summing Δ_m for all the zones. The value of Δ should be an integer in order to obtain constructive interference at the focus point. Any deviation from an integer would mean no focusing at that point on the z-axis. Figure 3.7 shows the deviations of phase difference (from a nearest integer) versus the normalized propagation distance, z/f. Zero deviation implies a position of constructive interference or a focal point. In the calculation, the FZPs with various f are assumed to have 8 zones and under the illumination of 633 nm plane wave. It is observed that only one point on the z-axis supported constructive interference (i.e., one focus point) for the FZPs with foci equal to or less than 0.5 mm (NA varies from 0.8 to 1 for the focal length changes from 5

μm to 0.5 μm respectively). However, higher order foci started to emerge from the zone plate with focal length equal to or larger than 5 mm (*NA = 0.05*). This shows that FZP with large NA used for near-field focusing suppress higher order foci.

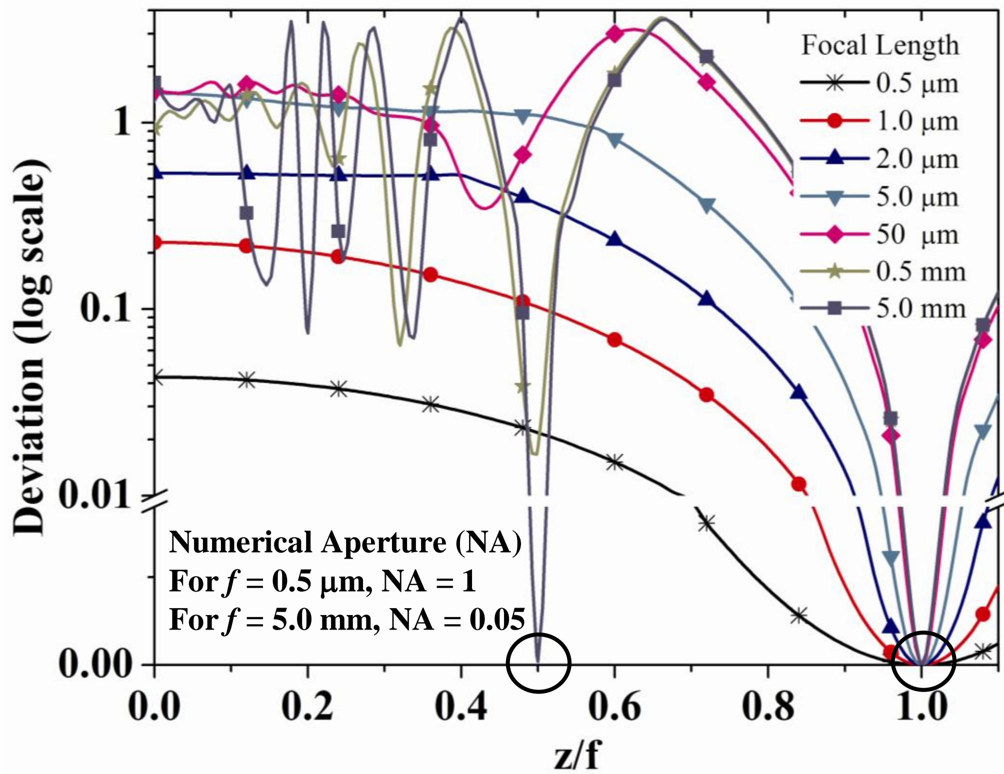

Figure 3.7 Plots of deviations of phase difference (from constructive interference from all 8 transparent zones) versus *z*-direction normalized by *f*.

3.3 Can FZP Structure Support SPP?

It has been demonstrated that the SPP can be used to enhance the transmission of light through a subwavelength hole surrounded by metallic circular corrugations on *Ag* film [30]. Hence, the transmission characteristics through a small hole surrounded by FZP structure are investigated in order to explore the possibilities of supporting SPP in metal-coated FZPs. Figure 3.8 compares the FDTD calculated transmission spectra of subwavelength hole (300 nm in diameter) surrounded with FZP structure (8 zones) and periodic annular corrugations (with period of 500 and 600 nm, and 8 and 12 rings) on

both sides of the *Ag* film. A very weak transmission is observed through the hole with FZP structure compared to the transmission through the hole with periodic annular structures, while enhanced transmission peaks are obtained with periodic annular structures. This is because the annular corrugations serve as a periodical perturbation to ensure the coupling of incident light with the SPP at the two interfaces of the symmetrical configuration. This interaction is only possible through the presence of grating momentum, which obeys the conservation of momentum [100, 101]. For annular corrugated structure, the coupling condition can be written as:

$$\vec{k}_{sp} = \vec{k}_r \pm i\vec{G}_r \tag{3.8}$$

where $\vec{k}_{sp}$ is the surface plasmon wave vector, $\vec{k}_r$ is the component of the incident wave vector that lies in the plane of the sample. $\vec{G}_r (= 2\pi / \Lambda)$ is a reciprocal wave-vector where Λ is the period of the circular corrugation. Equation (3.8) predicts that for normal incident of plane wave to the annular corrugated structures with Λ equals to 500 and 600 nm, the corresponding resonant wavelength are 515 and 617 nm, respectively. This is in close agreement with the observed resonant wavelength (i.e., the transmission peaks at 575 and 650 nm) as shown in Figure 3.8. For FZP structure, periodicity is absent (radius of zones changes as distance from center increases as shown in Figure 3.1) and there exists a broad spectrum of $\vec{G}_r$ vectors corresponding to each zone (Λ_1, Λ_2, Λ_3, ….). With FZP structures, coupling of SPP with propagating field becomes inefficient when compared with the periodic corrugation having a unique $\vec{G}_r$ vector satisfying Equation (3.8). The presence of 3 low intensity peaks from the FZP transmission pattern shown in Figure 3.8 indicates the influence of broad spectrum of $\vec{G}_r$. Therefore, FZP structure does not have any feature supporting

surface plasmon resonance. It is confirmed that the SPP is not the mechanism to achieve subwavelength focusing in FZPs [95].

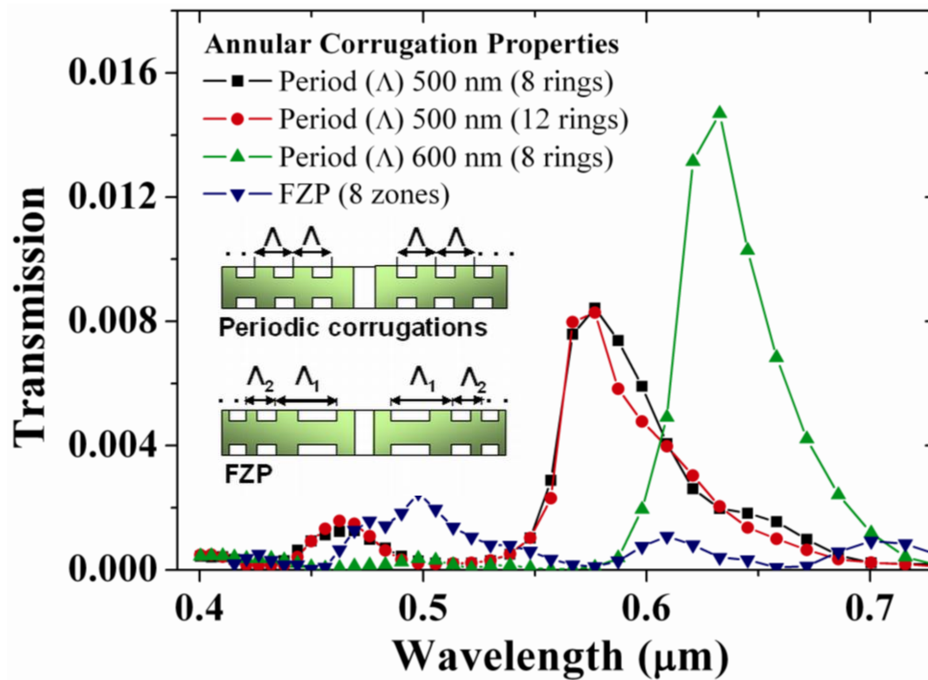

Figure 3.8 Plots of transmission spectra versus illumination wavelength through a hole (of 300 nm in diameter) from a 300 nm thick *Ag* film surrounded by annular corrugations (with periodic and FZP structures) with an etch depth of 60 nm on both sides of the films.

3.4 Improving Diffraction Efficiency with Phase Zone Plate

Conventional zone plates are known to show poor diffraction efficiency partly due to the existence of higher order foci. Ideally, $1/\pi^2$ (~10 %) of the power incident on the zone plate participates in the formation of principal image [102]. In section 3.3, it is found that the use of zone plates in the near-field regime gives higher diffraction efficiencies as a result of the suppression of higher order foci. The diffraction efficiency of metal-coated FZPs with 0.5 μm focal length can be as high as 40%.

However, the diffraction efficiency of metal-coated FZPs is still limited by the presence of opaque zones [103]. Therefore, the opaque zones are replaced with phase-shifting regions to improve the light collection efficiency [95]. This is possible as the phase zone plates required no metallic coating to form the opaque zones for the diffraction of evanesce waves [104]. In this case, it is assumed that the FZP structure is etched on glass substrate with no opaque zone. The thickness difference arising from the etch depth provides the required phase difference to achieve constructive interference for the evanescent fields among the zones. Figure 3.9 plots the electric field intensity profile at the focal plane (i.e., $y = 0$ and $z = f_c$ where f_c is the focal length obtained from the FDTD simulation) of the FZPs with different focal length and the corresponding etch depth is assumed to be 300 nm. Focusing at sub-wavelength scale is observed at an incident wavelength of 633 nm. It is noted that the focusing patterns are similar to that given in Figure 3.4. However, the maximum transmission intensity is about 6 times larger than that of the metal-coated FZPs. This is because the proposed phase zone plates have no opaque zones and the reflection and absorption of light are significantly reduced. The diffraction efficiency is improved from 40% to 47% for phase zone plates with 0.5 μm focal length when compared with that of the metal-coated FZPs.

Phase difference, Δ, from a phase zone plate due to the thickness difference, t, between zone regions can be expressed as

$$\Delta = \frac{2\pi}{\lambda}(n_{sub} - 1)t \tag{3.9}$$

where n_{sub} is the refractive index of the substrate material. For phase zone plate with N zones, intensity at a focus plate is shown to be [103]:

$$I \;\alpha\; N^2 (1 - \cos \Delta) \tag{3.10}$$

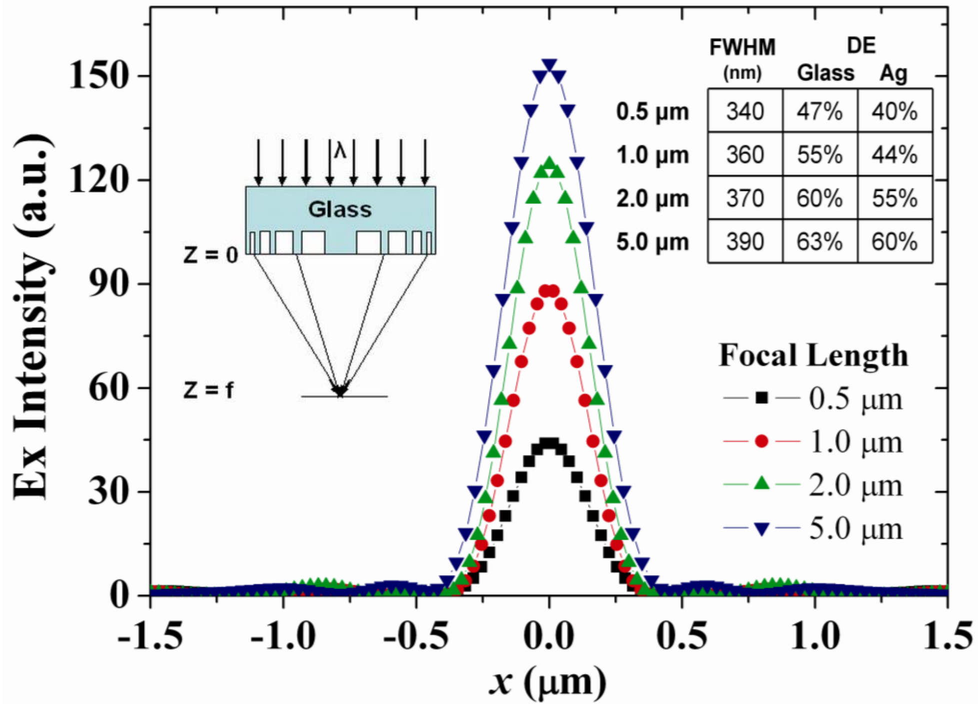

Figure 3.9 Electric field intensity distribution verses x (y = 0 and $z = f_c$) direction for phase zone plates with f = 0.5 to 5.0 μm etched on glass all with etch depth of 300 nm.

Maximum intensity is achieved with $\Delta = \pi$. For glass phase zone plate, the optimized value of t is approximately 692 nm for an incident wavelength of 633 nm. Figure 3.10 shows the peak intensity as a function of etch depth for 4 designed focal lengths. It is observed that the maximum intensity occurs at an etch depth of ~ 690 nm for the focal length of 5 μm. However, the reduction of focal length reduces the required value of etch depth to achieve maximum intensity. The deviation from Equation (3.10) for the phase zone plate with small focal length can be understood from its electric field intensity distribution Figure 3.10.

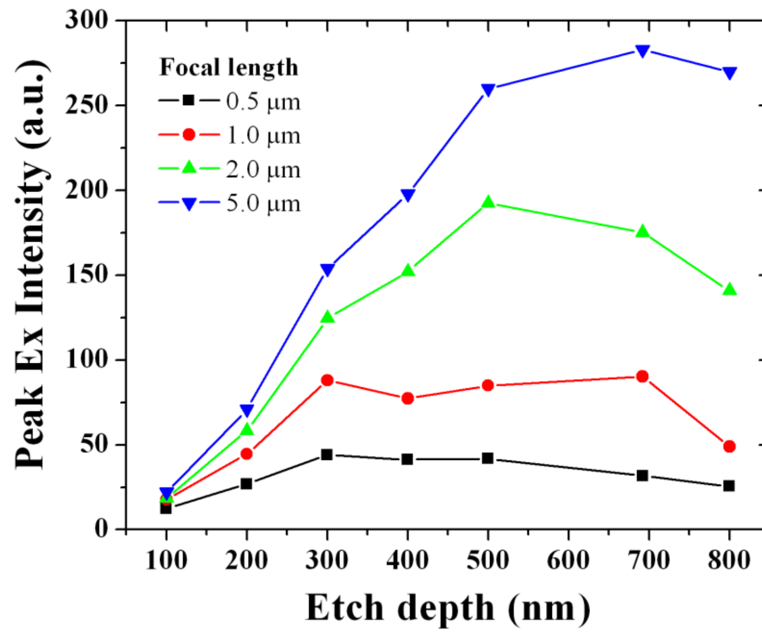

Figure 3.10 Peak electric field intensity (in a.u.) versus etch depths at focal plane for focal length equal to 0.5 μm, 1 μm, 2 μm and 5 μm. Fresnel zone structure (8 zones) was etched on glass substrate for 100 – 800 nm depths. Wavelength of incident plane wave is 633 nm.

Figure 3.11 shows the electric field intensity distribution along the *x* and *z*-directions of the phase zone plates with a focal length of 0.5 μm. The change in the field distribution along the z-direction with increasing etch depth is observed to follow an irregular trend. The electric field intensity at the focal point increases when the etch depth is increased from 100 nm, which reaches a maximum value when the etch depth is 300 nm. By contrast, Equation (3.10) predicts a maximum focusing intensity at an etch depth of 692 nm. This can be explained by the phenomenon of diffracted evanescent fields operating in the near-field regime.

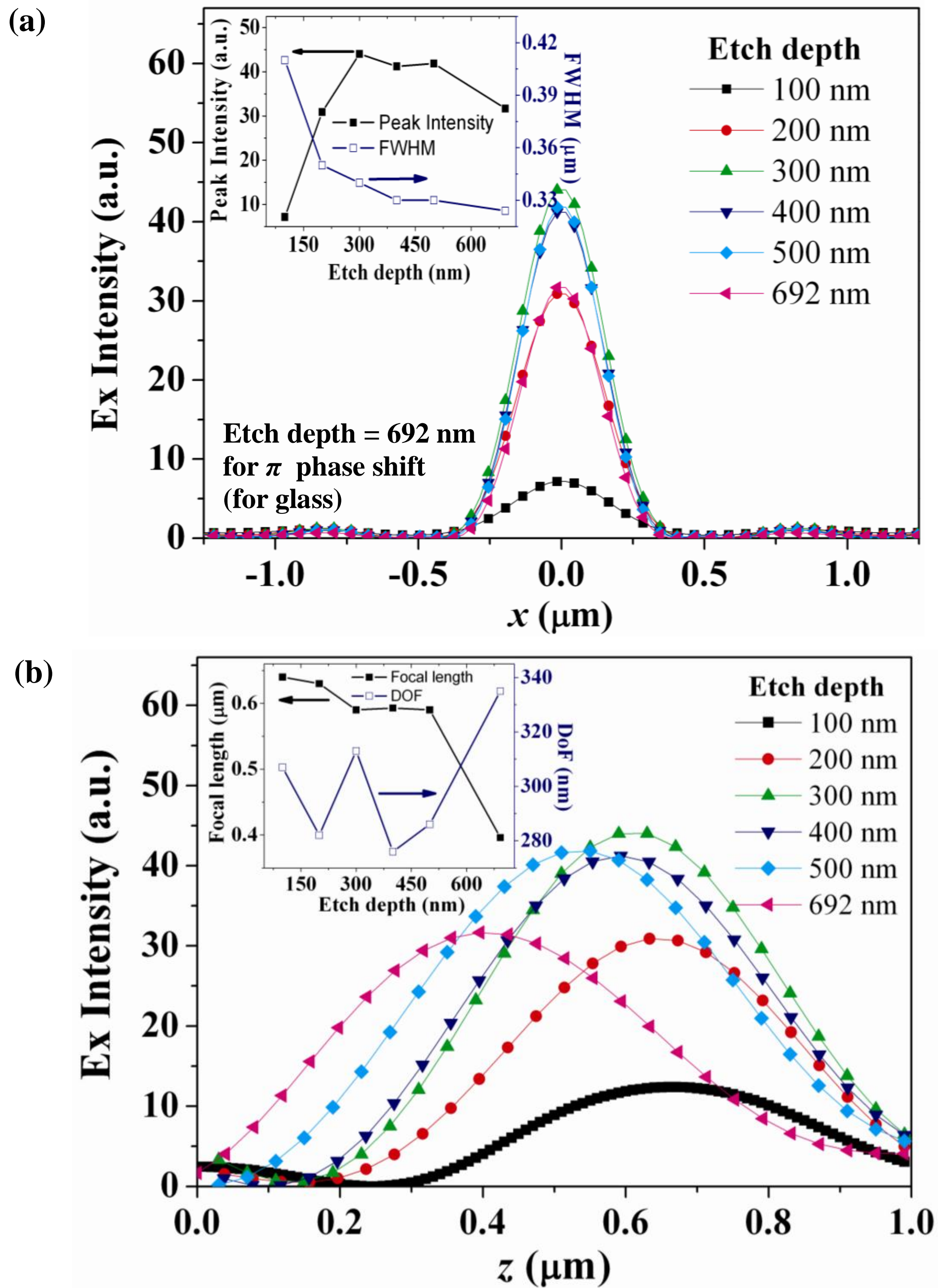

Figure 3.11 Electric field intensity distribution (in a.u.) along the x ($y = 0$ and $z = f_c$) direction. The inset shows peak electric field intensity and focal spot size (FWHM) at various etch depths (b) Electric field intensity distribution (a.u.) along the z-direction ($x = y = 0$). Inset shows actual focal length and DoF versus etch depths. Fresnel zone structure was etched on glass substrate for 100 – 692 nm depths. Wavelength of incident plane wave is 633 nm. 8 zones are designed for focusing at 0.5 μm.

For higher etch depths, evanescent fields undergo multiple scattering and coupling with radiating fields becomes inefficient. This effect leads to the observed anomaly beyond 300 nm etch depth.

Figure 3.12 shows the electric field intensity distribution along the x and z-directions direction of the phase zone plates with a focal length of 5 μm. The focusing intensity is found to be maximized when the etch depth approaches its ideal value of 692 nm. The focal spot is found to move towards the zone plate as the etch depth is increased and the corresponding FWHM, as shown in the inset of Figure 3.12(a), remains constant for etch depths greater than 380 nm. The focusing characteristics are degraded with deviation of etch depth from its ideal value. This is due to the deviations in the induce phase errors and all zero-order radiation cannot be cancelled.

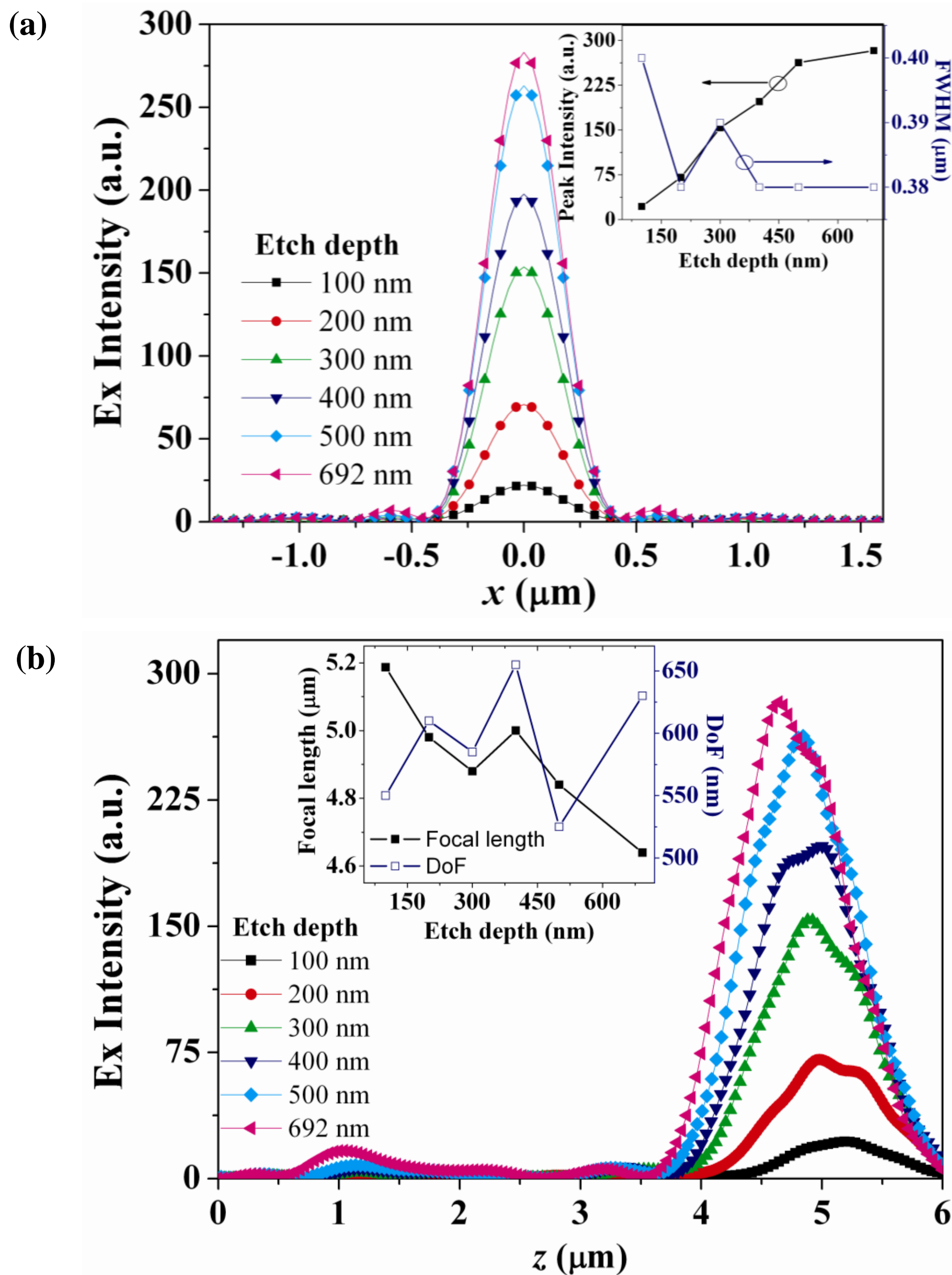

Figure 3.12 (a) Electric field intensity distribution (in a.u.) along the x ($y = 0$ and $z = f_c$) direction. The inset shows peak electric field intensity and focal spot size (FWHM) at various etch depths (b) Electric field intensity distribution (a.u.) along the z-direction ($x = y = 0$). Inset shows actual focal length and DoF versus etch depths. Fresnel zone structure was etched on glass substrate for 100 – 692 nm depths. Wavelength of incident plane wave is 633 nm. 8 zones are designed for focusing at 5 µm.

3.5 Summary

The focusing behavior of FZPs with a classical design is investigated for their near-field focusing. The focusing characteristics are affected by the presence of near fields which is in contrast with zone plates in the far field wherein focusing is mainly due to the interference of diffracted component of the field. It is found that the use of FZPs for near-field focusing exhibits unique characteristics of 1) focal shift, 2) elongated DoF and 3) the suppression of higher order foci [95]. The shift of focal length and elongation of DoF can be optimized by controlling the number of zones and the choice of film thickness of the FZPs. In general, the use of *Ag*-coated FZPs with 12 zones and *Ag* thickness of more than 400 nm minimize the influence of focal shift. However, a larger metal thickness leads to reduction of focusing intensity and an elongation of DoF. On the other hand, it is observed that the use of FZPs for near-field focusing shows no higher order foci so that the corresponding diffraction efficiency can be improved to ~40%. However, it is necessary for the focal length of the FZPs to be less than ~10 times the operating wavelength. This work shows that the unique characteristics of FZPs are not due to the influence of SPP. This is because the FZPs do not have any feature supporting surface plasmon resonance. Instead, the unique characteristics are more appropriately explained by the diffraction of evanescent fields inside the subwavelength feature of the transparent zones in FZPs.

The use of phase zone plates to achieve subwavelength focusing with high transmission efficiency is also investigated [95]. The phase zone plates can be obtained by realizing the required zones through etching on the glass substrate so that no opaque coating is required. It is found that the phase zone plates can support high-intensity focal spot with subwavelength size. The peak transmission power is found to be 5 times higher than those from *Ag*-coated FZPs.

Chapter 4

Subwavelength Focusing Behavior of High Numerical-Aperture Phase Fresnel Zone Plates under various Polarization States

This chapter concentrates on polarization effects due to large numerical aperture (NA) on the focusing characteristics of a binary phase Fresnel zone plate (FZP). An analytical model of vector formalism, which is based on Richards and Wolf's electromagnetic diffraction theory, is developed to understand the focusing mechanism of phase FZPs. The analytical model is verified by comparing with the exact results obtained from the finite-different time-domain (FDTD) simulation.

4.1 Theoretical Formulation

Owing to the vector nature of light, focal spot of high NA focusing systems suffer from a rotational asymmetry under the illumination of linear polarized (LP) light [105, 106]. Hence, the use of radially polarized light has been proposed to attain rotationally symmetric focusing [107-109]. It is expected that phase FZPs under the illumination of radially polarized light could produce a rotationally symmetric focusing spot with better diffraction efficiency than that obtained from the linearly polarized light. On the other hand, in order to ascertain and understand the physics behind the focusing behavior of high NA phase FZPs, an analytical model is required to be developed.

Such an analytical model will also be useful to analyze and design phase FZPs for better focusing characteristics. Rigorous diffraction theories are well established in modeling grating structures [66, 110]. However, analytical model based on rigorous diffraction theory to study focusing characteristics of phase FZP with a high NA and small number of zones will be too complex to formulate.

The theory developed by Richards and Wolf [105] can be extended to study the focusing characteristics of binary phase FZPs [111]. This can be done by selecting the successive zones of the phase FZPs to transform input wave into spherical wavefront [92]. Figure 4.1 shows the cross-section schematic of a phase FZP and its focusing parameters. The analytical expressions of the focal spot obtained from the phase FZP can be deduced by using Kirchhoff's boundary conditions. The influence of inhomogeneous waves (i.e., evanescent waves) is also ignored in the derivation. This assumption is reasonable as the diffraction waves are the dominant fields of the focal spot. Hence, the components of electric field vector near the focal region can be written as [105]:

$$\mathbf{E} = \begin{pmatrix} E_x \\ E_y \\ E_z \end{pmatrix} = \frac{-iA}{\pi} \int_0^{\alpha} \int_0^{2\pi} BC \exp(ik(\hat{\mathbf{s}} \bullet \mathbf{r})) \begin{pmatrix} \cos\theta + \sin^2\phi(1-\cos\theta) \\ (\cos\theta - 1)\sin\phi\cos\phi \\ -\sin\theta\cos\phi \end{pmatrix} \sin\theta d\theta d\phi \quad (4.1)$$

where $A = kfl_0/2$, l_0 denotes the relative amplitude of the field, k (= $2\pi/\lambda$) is a wave vector and f is a focal length. B is a factor accounting for the energy conservation in the transmission of field through the focusing system and C is a phase transfer function. Angle ϕ is the azimuth angle as defined in Figure 4.1. $\phi = 0$ represents the polarization direction of the incident light. Vector $\boldsymbol{s}$ is the propagation direction of a light ray and vector $\boldsymbol{r}$ is the position vector on the focal plane at $z = 0$.

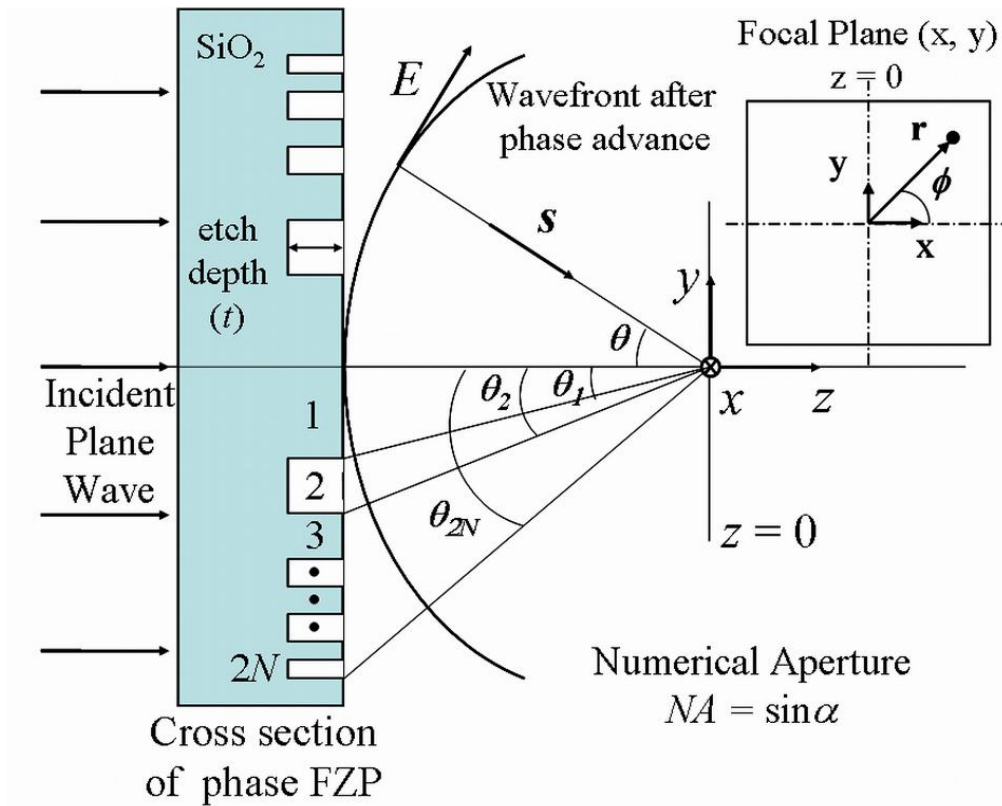

Figure 4.1 Schematic cross section of a binary phase FZP.

Integrations over ϕ are achieved using following identity:

$$\int_0^{2\pi} \cos n\phi \exp(ikr\cos(\phi-\gamma))d\phi = 2\pi i^n J_n(r)\cos n\gamma \tag{4.2}$$

$J_n(\rho)$ is the Bessel function of the first kind and n is the order of the Bessel function.

If the phase FZP is illuminated by a linearly polarized light, normalized cylindrical co-ordinates $u = kz\sin^2\alpha$ and $v = kr\sin\alpha$ can be used to simplify Equation (4.1) as shown below:

$$\left.\begin{aligned} E_x &= -iA(I_0 + I_2 \cos 2\phi) \\ E_y &= -iAI_2 \sin 2\phi \\ E_z &= -2AI_1 \cos\phi \end{aligned}\right\} \tag{4.3}$$

where $I_{0,}$, I_1 and I_2 are integrals defined as:

$$\left.\begin{aligned} I_0 &= \int_0^\alpha BC \sin\theta(1+\cos\theta) J_0\left(\frac{v\sin\theta}{\sin\alpha}\right)\exp\left(\frac{iu\cos\theta}{\sin^2\alpha}\right)d\theta \\ I_1 &= \int_0^\alpha BC \sin^2\theta J_1\left(\frac{v\sin\theta}{\sin\alpha}\right)\exp\left(\frac{iu\cos\theta}{\sin^2\alpha}\right)d\theta \\ I_2 &= \int_0^\alpha BC \sin\theta(1-\cos\theta) J_2\left(\frac{v\sin\theta}{\sin\alpha}\right)\exp\left(\frac{iu\cos\theta}{\sin^2\alpha}\right)d\theta \end{aligned}\right\} \tag{4.4}$$

The coefficient B (= $\cos^{-3/2}\boldsymbol{\theta}$) takes into account of the diffractive lensing for a diffractive zone plate [112]. To calculate the phase transfer function, C, the phase front due to the phase FZP can be treated as a combination of phase modulation introduced by two zone plates. Hence, Δ can be approximated by $\Delta \sim k(n-1)t$ where n is the refractive index of the FZP and t is the etch depth [103]. If the FZP has N full zones and θ_j (where $j = 0, 1, \ldots, 2N$) is the angle subtended by Fresnel zone boundaries (as indicated in Figure 4.1), it can be shown that

$$C = \begin{cases} \exp(i(\Delta-\delta))\exp(i\pi) & \text{for } \theta_{2N\text{-}2} \le \theta \le \theta_{2N\text{-}1} \\ \exp(-i\delta)\exp(i\pi) & \text{for } \theta_{2N\text{-}1} \le \theta \le \theta_{2N} \end{cases} \tag{4.5}$$

where N is an integer and $\delta = kf/\cos(\theta) - kf$ [113].

4.2 Rotationally Asymmetry of a Focal Spot under High NA Phase FZP

In the following investigation, it is assumed that the phase FZP is formed by etching 8 zones on a SiO_2 substrate (i.e., $N = 1, 2, \ldots, 8$) with $\Delta = \pi$ and $f = 0.5$ μm (i.e., NA = 0.996). Figure 4.2(a) plots the intensity profiles of all the electric field components observed at the focal plane of the phase FZP calculated from Equation (4.3) under the illumination of a linearly polarized (polarized along the x-axis) plane wave with λ = 633 nm. It is noted that the total intensity profile, $|E|^2(= |E_x|^2 + |E_y|^2 + |E_z|^2)$, is mainly determined by E_x and E_z. The profile of $|E|^2$ at the focal plane resembled the shape of a bone along the x-axis. The beamwidth is found to be 555 nm (0.87λ) and 250 nm (0.39λ) along the x- and y- axis respectively. This is because although all the parallel electric field vectors can add up arithmetically like scalars in the plane perpendicular to the polarization plane (i.e., $\phi = \pi/2$) as shown in the Figure 4.2(b-c), the field vectors in the other planes ($0 \leq \phi < \pi/2$) are partially canceled. As a result, the focal spot bears no longer rotational symmetry. In addition, the incident rays are severely bended after focused by the high NA system so that the field intensity along the z-axis is increased. This indicated that the linearly polarized (E_x) incident field gets 'depolarized' (i.e. electric field at the focus has significant E_x and E_y components) after focusing [111].

(a)

(b) **(c)**

Figure 4.2 (a) Near-field focusing characteristics of a phase FZP with 8 zones (NA = 0.996) under linearly polarized illumination obtained from the analytical model. Electric field intensity distribution shown at the focal plane of the phase FZP with $\Delta = \pi$. (b) Polarization vector distribution of a linearly polarized source. Cross-section shown is a *xy*-plane and polarization direction is along *x*-axis. (c) Polarization vectors after focusing of a linearly polarized beam by FZP.

The extent of depolarization depends upon the NA of the system. Figure 4.3 shows the intensity distribution of $|E|^2$, along the *x*-axis of the focal plane for different NA values. It is observed that the increase of NA broadens the beamwidth of the focal spot along the *x*-axis. This indicated that the degree of depolarization increases with the increase of NA of the phase FZPs. To characterize the extent of a focal spot distortion due to depolarization, a "depolarization ratio" is defined as $|E_x|^2/|E_z|^2$.

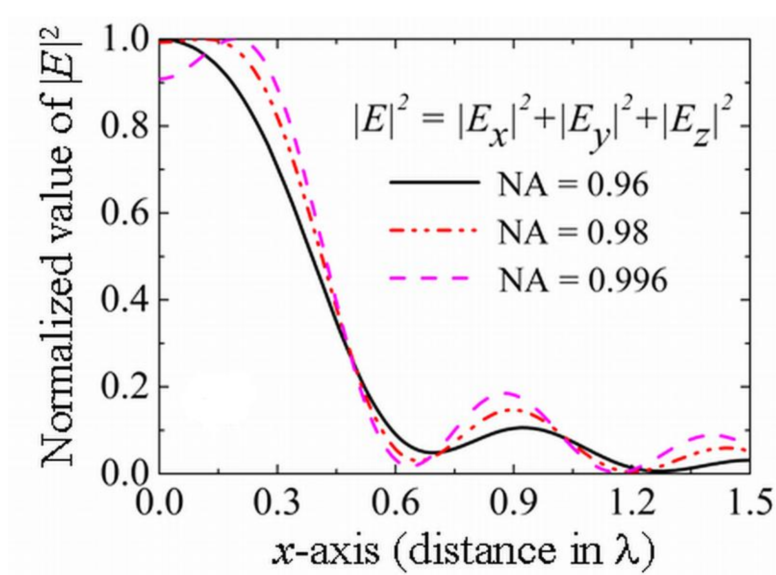

Figure 4.3 Plot of $/E/^2$ along the *x*-axis versus different NA.

Figure 4.4 shows the influence of phase difference, Δ, on the depolarization ratio. For a small value of Δ (i.e., low etch depths), the transformed wavefront approaches a profile as if it was focused by a low NA system (i.e., less bending of focused waves along the *z*-axis). Hence, better symmetric profile of focal spot can be obtained when compared to that with large value of Δ (i.e., high etch depth) [111]. However, the value of $|E_z|^2$ becomes more dominant with the increase of Δ.

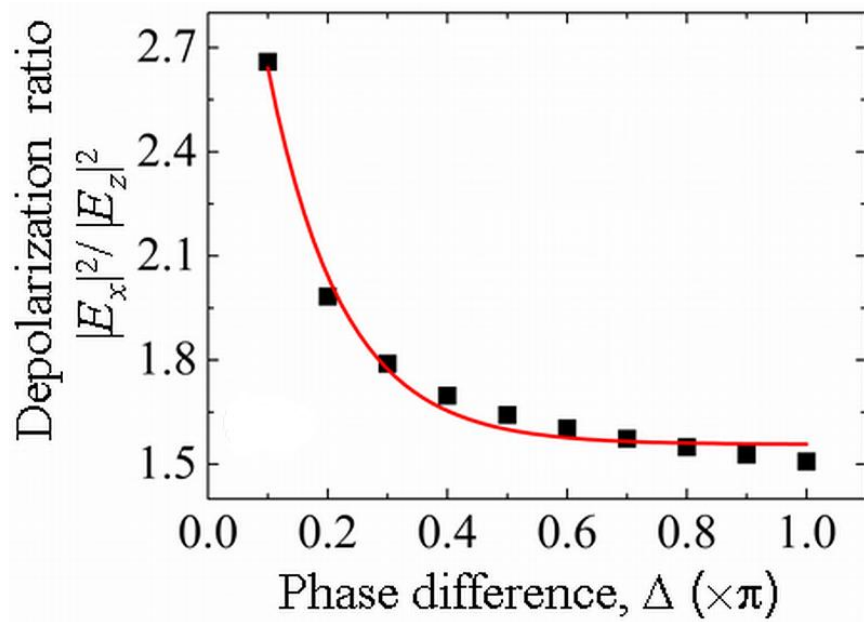

Figure 4.4 Depolarization ratio against phase difference, Δ, of the phase FZP for NA = 0.996.

4.3 Comparison with Exact Calculation with FDTD

Figure 4.2 is re-plotted in Figure 4.5 by using a finite-difference time-domain (FDTD) method. In the simulation, mesh size is set to 15×15×15 nm^3 and perfectly matched layer is used as the boundary conditions. Input source is a 633 nm wavelength linearly polarized plane wave and the phase FZP is assumed to have an etch depth of 692.5 nm (i.e., equivalent to $\Delta = \pi$). Figure 4.5 plots the intensity profiles of all the electric field components observed at the focal plane of the phase FZP. It is noted that the field distribution calculated from the FDTD method is close to that predicted from the analytical model. This implies that the analytical model, which does not account for the inhomogeneous waves, can match well with the FDTD calculation. The ignorance of inhomogeneous waves in the derivation of the analytical model is shown to be reasonable.

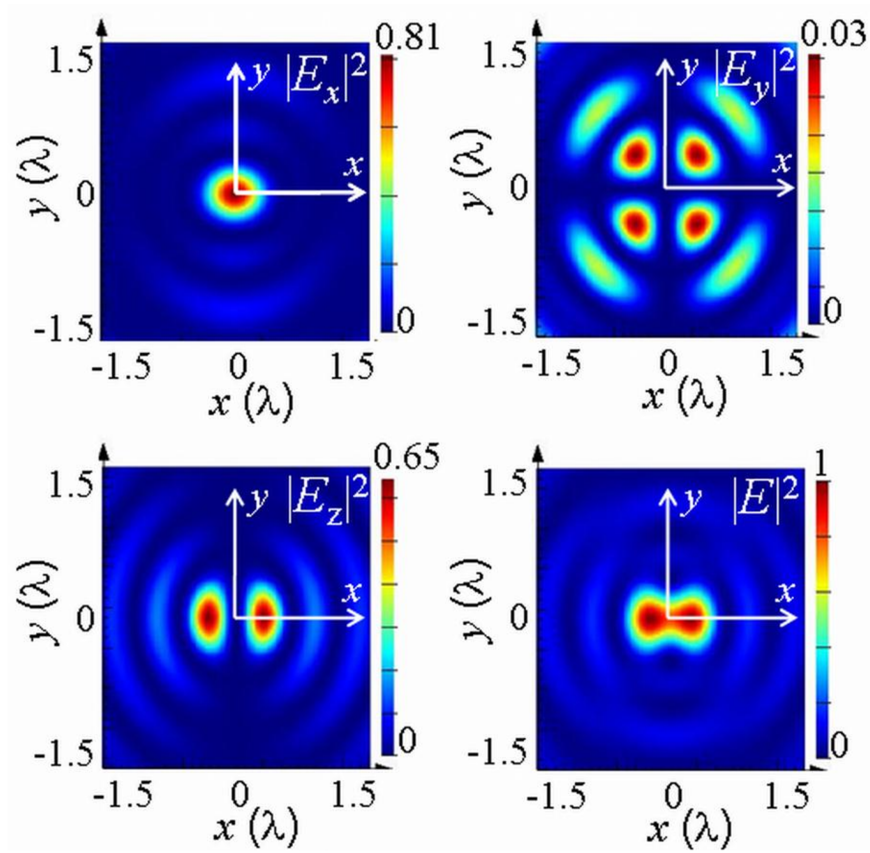

Figure 4.5 Near-field focusing characteristics of a phase FZP with 8 zones (NA = 0.996) under linearly polarized illumination obtained from FDTD simulation. Electric field intensity distribution observed at the focal plane of the phase FZP with etch depth of 692.5 nm.

Figure 4.6 shows the intensity distribution of $|E|^2$, $|E_x|^2$, and $|E_z|^2$, along the x-axis of the focal plane for the phase FZP with etch depth of 200 nm and 692.5 nm. Etch depth of 200 nm (692.5 nm) is equivalent to $\Delta = 0.29\pi$ (1.0π) at wavelength of 633 nm. A strong E_z component (i.e., $|E_z|^2/|E_x|^2 = 0.80$) can be seen for the etch depth equal to 692.5 nm. For the etch depth equal to 200 nm, E_z component is weakened (i.e., $|E_z|^2/|E_x|^2 = 0.23$). The focal spot, whose beamwidth along the *x*-axis is reduced to 0.79λ, is appeared to be more symmetric.

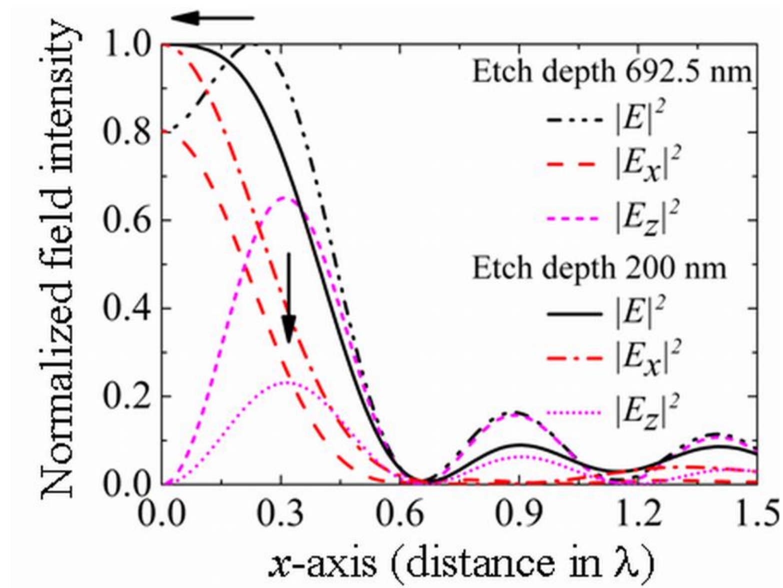

Figure 4.6 Plots of $|E|^2$, $|E_x|^2$ and $|E_z|^2$ along the x-axis for the phase FZP with etch depth of 200 and 692.5 nm.

Figure 4.7 plot gives detailed electric field intensity components distribution in focal plane for a phase zone plane with etch depth t = 200 nm. Total field intensity profile has a better symmetry when compared with corresponding profile with etch depth t = 692.5 nm (see Figure 4.5). It must be noted that, E_z component can still be seen with etch depth of 200 nm due to the high NA of the phase FZP. E_y field component is increased but its overall contribution towards the total intensity is still small and can be neglected. Thus, cross-section of a focal spot is elliptical with larger spot size along the polarization direction i.e. along x-axis.

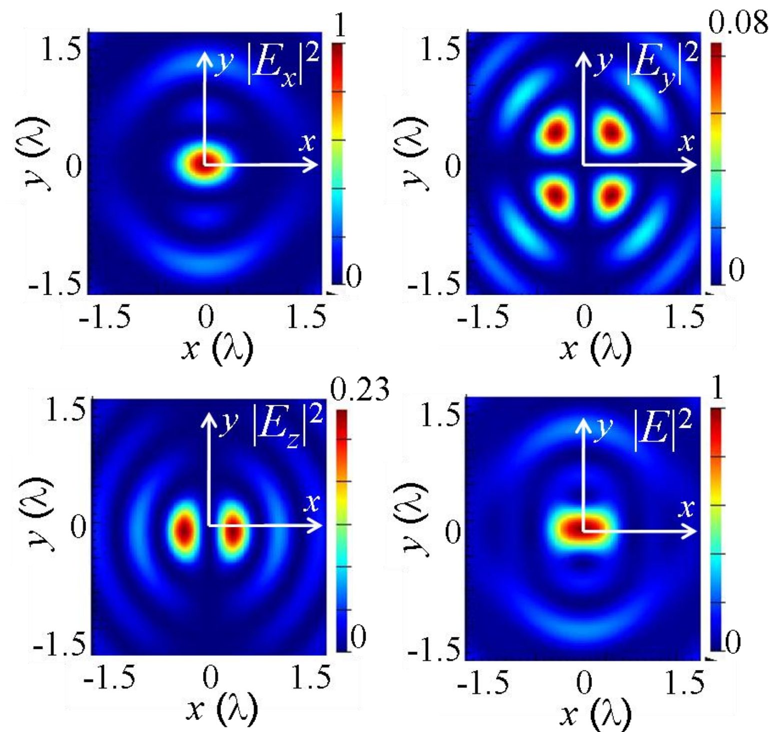

Figure 4.7 Near-field focusing characteristics of a phase FZP with 8 zones (NA = 0.996) under linearly polarized illumination obtained from FDTD simulation. Electric field intensity distributions observed at the focal plane of the phase FZP with etch depth of 200 nm.

Figure 4.8 plots the dependence of depolarization ratio on the etch depth of the phase FZP. It is observed that the depolarization ratio reduces with the decrease of etch depth. For an etch depth equal to π phase-shift, the influence of evanescent waves is minimized due to the constructive interference of diffraction waves so that the predicted results are close to that obtained from the FDTD method. For other etch depths, the proposed model shows deviation from the exact calculation. However, the overall trend is in agreement with the exact calculation.

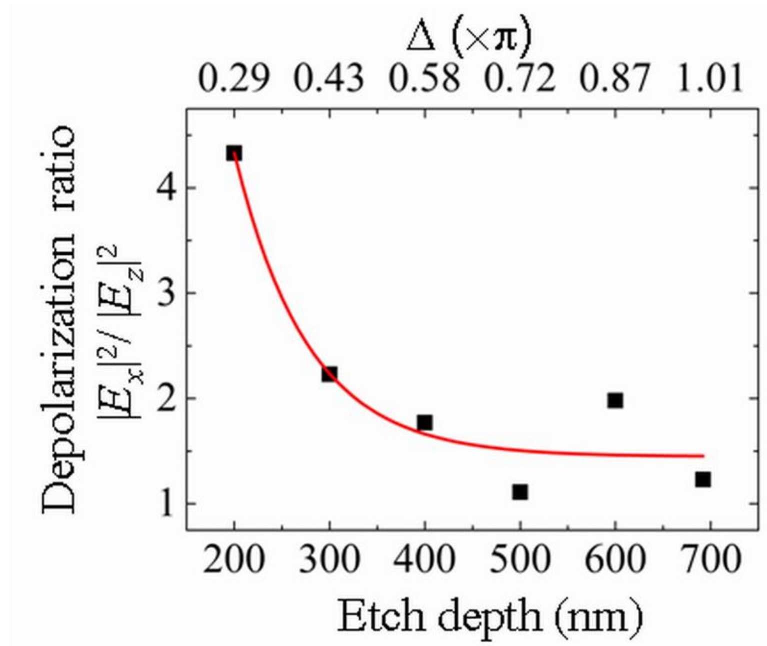

Figure 4.8 Depolarization ratio against etch depth of the phase FZP for NA = 0.996.

High numerical aperture effects can further be reduced by using focused beam following Gaussian distribution. Gaussian distribution has a Gaussian intensity profile given as:

$$I = I_0 \exp(-2\frac{r^2}{w^2}) \tag{4.6}$$

where w is the half width of the beam to the $1/e^2$ intensity point at some distance from the waist along the propagation axis, and r is the radial distance from the center of the beam.

It is evident from Equation (4.6), that most of the energy is concentrated around center and reduces along radial direction. To investigate further, Gaussian beams with a FWHM of 4 µm and 7 µm are considered. Figure 4.9 shows focal spot size (FWHM) of total field intensity along polarization direction (x-axis) is reduced

with the reduction in waist diameter of source beam. This is because Gaussian nature of the source makes lesser amount of energy available for diffraction from outer zones than from inner zones. Contribution of severely diffracted beams by outer zones is reduced and thus minimizing the depolarization effect due to presence of $|E_z|^2$. In the direction perpendicular to the polarization (y-axis), spot size found to be increasing with reducing source size. Along y-axis contribution of $|E_z|^2$ is zero as shown in Figure 4.7. It is interesting to note here that spot size of $|E_x|^2$ component of field intensity found to be increasing with reduction in source size. This suggests that outer zones of the FZP are important in reducing the focal spot size. However, increasing number of zones may reduce the spot size of $|E_x|^2$ component but at the same time, increased NA leads to increase in $|E_z|^2$ component and deteriorates the resolution.

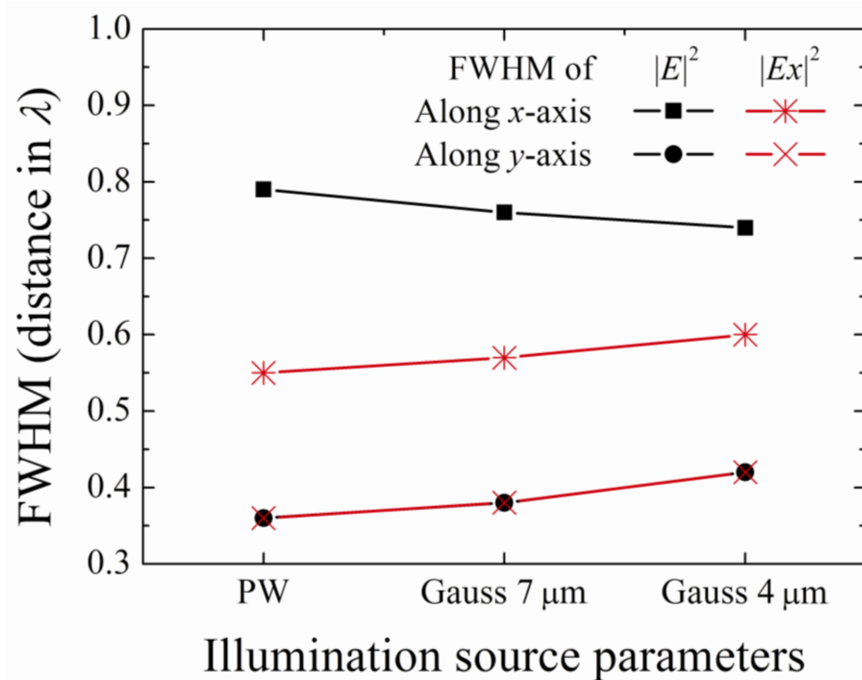

Figure 4.9 Effect of focused Gaussian source size (FWHM) on FWHM of focal spot. PW: Plane wave.

A flat-top Gaussian distribution is also investigated. In FDTD calculations, a flat-top distribution is implemented through the following equation for a super-Gaussian beam [114]:

$$I = I_0 \exp\left\{-2\left(\frac{r}{w}\right)^m\right\} \tag{4.7}$$

For values above m = 50, a flat-top profile is realized. When m = 2, the equation reduces to Equation 4.6 and Gaussian distribution can be achieved.

Figure 4.10 shows a normalized intensity profiles for beam width (FWHM) of 4 µm. Under Gaussian illumination, side lobes are distributed over a wider region due to interference effect by weakly diffracted field from outer zones. In contrast, with the flat-hat source, no field is present at zones lying outside the beam width of the source. Thus, side lobes are observed over a region limited by the beam width of a flat-hat illumination.

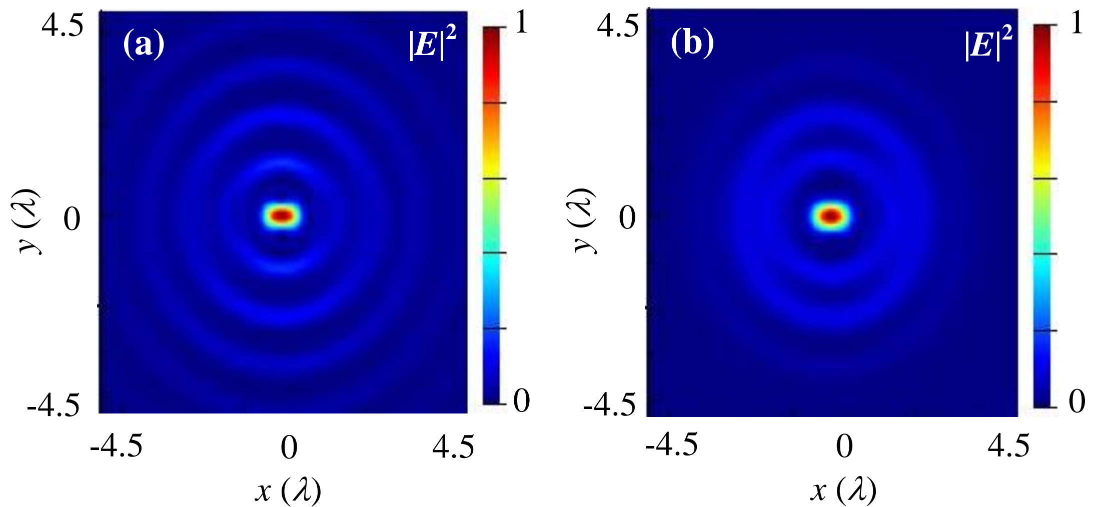

Figure 4.10 Comparison of flat-top and Gaussian illumination for phase FZPs. Detailed $|E|^2$ profile in the focal plane under illumination beam width (FWHM) of 4 µm for (a) a Gaussian source (b) a flat-top source.

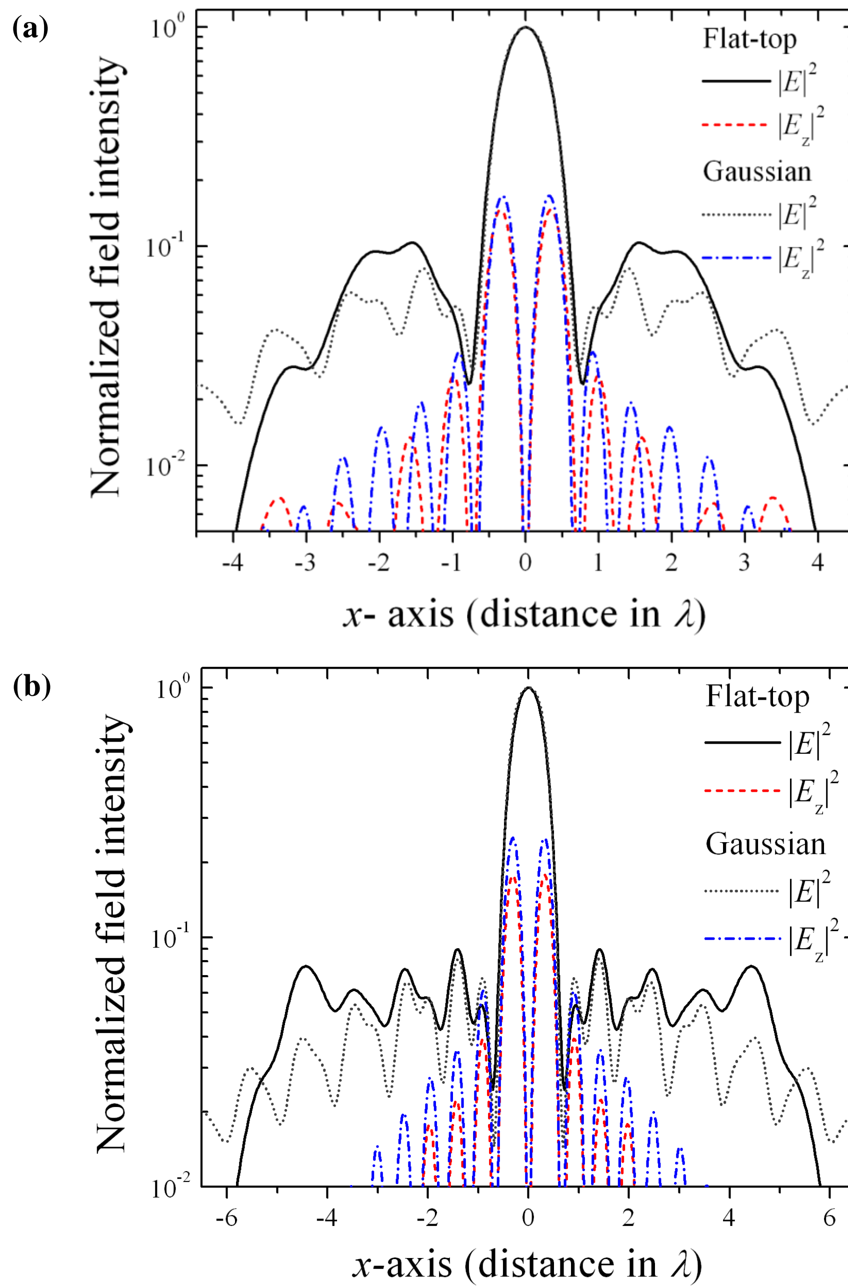

Figure 4.11 Comparison of flat-top and Gaussian illumination for phase FZPs. Detailed $|E|^2$ profile in the focal plane under illumination beam width (FWHM) of 4 μm for (a) a Gaussian source (b) a flat-top source.

Figure 4.11 plots field intensity profile along *x*-axis for beam width of (a) 4 μm and (b) 7 μm. Focal spot sizes remain the same under both Gaussian and flat-top Gaussian illuminations. This is because, in both cases, major contribution is from the fields diffracting from central zones. Intensity of side-lobes is found to be more with a

flat-top source than the side-lobe intensity observed for the Gaussian source. However, an effective numerical aperture of the FZP is reduced and hence the contribution of E_z component of the field is also reduced while using a flat-top source.

4.4 Amplitude FZP under Linearly Polarized Illumination

In order to investigate the focusing properties of amplitude FZP, a FZP having Au coating of 200 nm thickness is considered for FDTD simulations. Figure 4.12 shows detailed field distributions in the focal plane. Illumination source is linearly polarized along *x*-axis. As observed with the phase FZP, a total intensity distribution resembles a bone like shape in case of amplitude FZP. Distribution of intensity component along the incident polarization direction (E_x) shows an elliptical profile of focal spot. Amplitude FZP exhibits a dominating longitudinal field component (E_z) suggesting a strong presence of evanescent waves coupling with diffracted radiation. In fact, contribution of E_z component to the total field intensity is greater than the contribution of E_x component of the field. In case of phase FZP, as shown in Figure 4.6, by controlling etch depth of zones, it is observed that the output phase can be controlled such that the maximum intensity can be attained at the center of the focal spot (see Figure 4.7). However, with the amplitude FZPs, since focusing is attained with alternate transparent and opaque zones, phase manipulation is not as obvious as with phase FZPs. Thus, the focusing performance of amplitude FZPs is inferior because of poor diffraction efficiency and distorted focal profile when compared with phase FZPs.

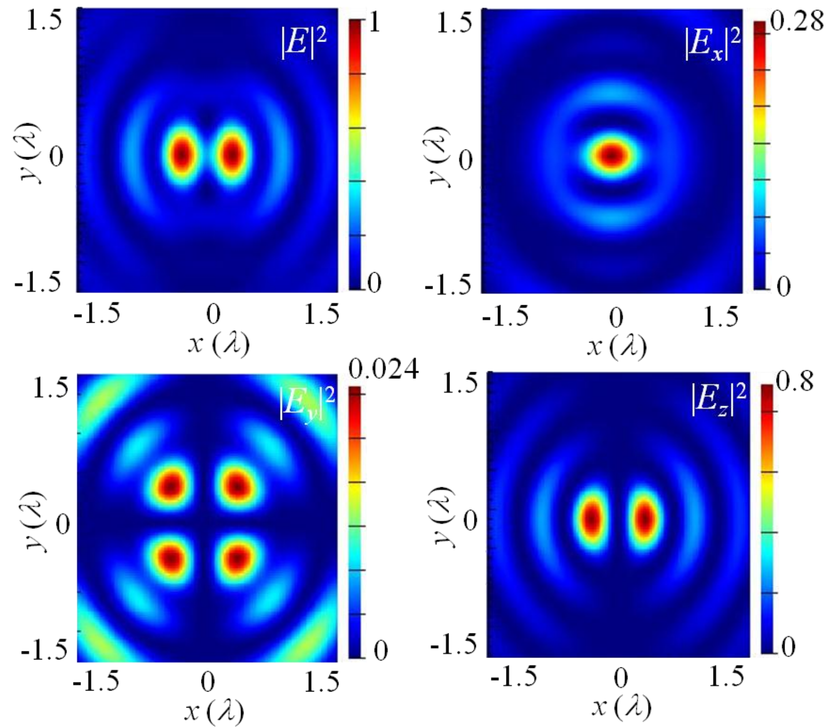

Figure 4.12 Detailed intensity distribution in the focal plane obtained by FDTD simulations for amplitude FZP (*Au* coating of 200 nm thickness) under linearly polarized illumination along *x*-axis.

4.5 Rotationally Symmetric Focusing using Circularly Polarized Illumination

As discussed in the section 4.2, linearly polarized illumination gives rise to asymmetry in the focal spot profile under high NA focusing elements. With the use of circular polarization, a symmetric profile of the focal spot may be achieved. To investigate it further, a circular polarization is implemented in FDTD calculation via superposition of two linearly polarized sources orthogonal to each other and having a phase shift of $\pi/2$ between them.

Figure 4.13 shows a field profile under circularly polarized illumination for a phase FZP. Total field intensity reveals a rotationally symmetric focal spot with a maximum intensity observed along the *z*-axis. The field components E_x and E_y have an

elliptical profile due to high numerical aperture effects as observed in the case with a linearly polarized illumination. It is interesting note that the field profile of E_z component which is of an annular ring. This is a result of homogeneous distribution of the incident field along in the *xy*-plane as the illumination is circularly polarized.

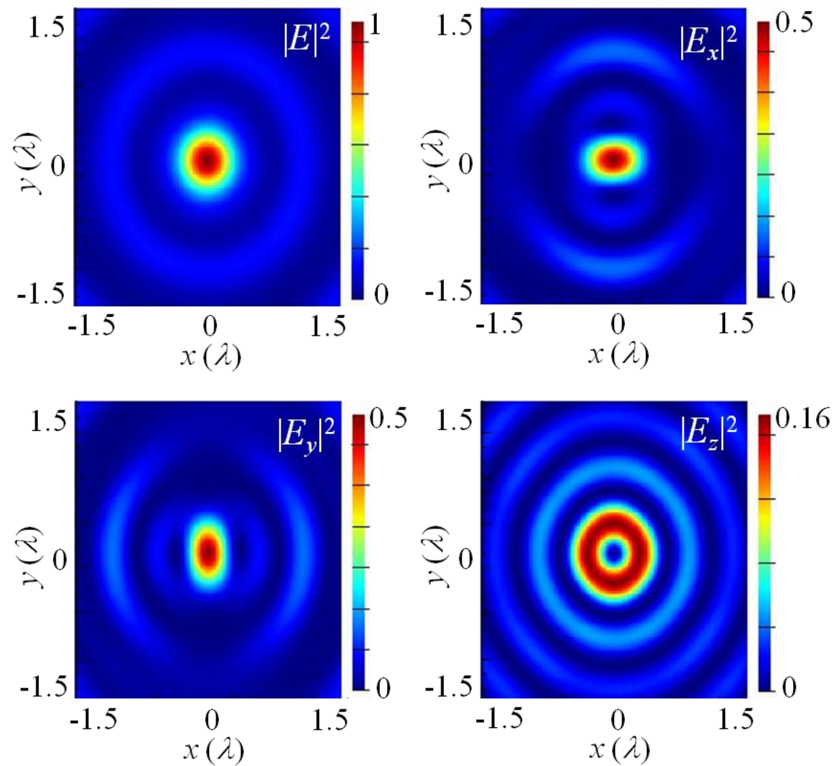

Figure 4.13 Detailed intensity distribution in the focal plane obtained by FDTD simulations for a phase FZP under circularly polarized illumination. Etch depth of 200 nm was used in a glass.

A comparison has been made with amplitude FZPs. As discussed in the section 4.4, with amplitude zone plates, E_z component of the field is dominating and hence under circularly polarized illumination the dominant E_z makes the maximum total field intensity point to shift away from the axis. As seen from

Figure 4.14(a), a dip in the intensity along the propagation axis (*z*-axis) is observed. However, the contribution of E_z towards the total intensity is reduced

because illumination energy is distributed along *x*- and *y*-axis. The net effect is a rotationally symmetric focal spot with a dip along *z*-axis as shown in Figure 4.14(b).

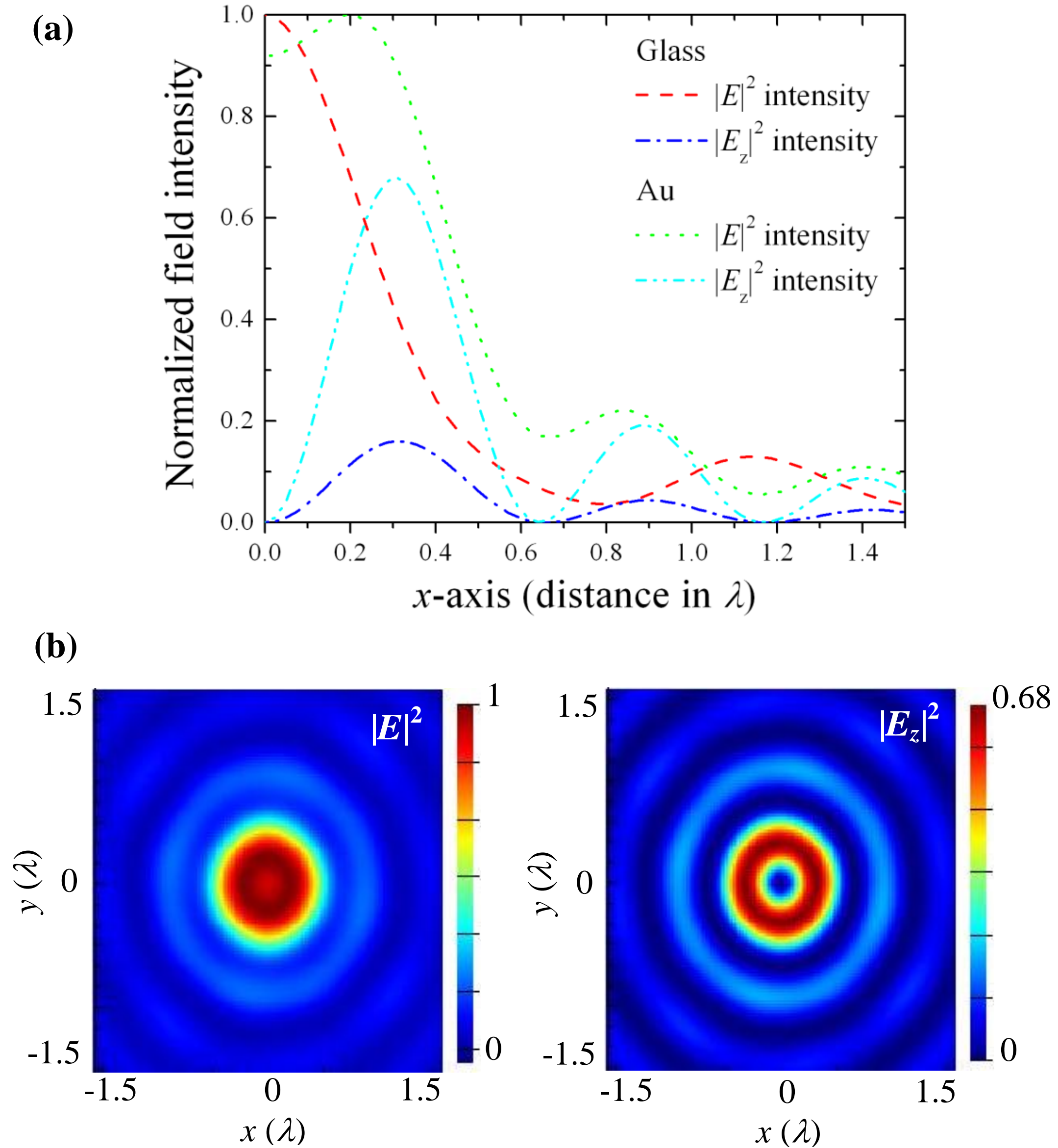

Figure 4.14 Comparison of phase and amplitude FZPs under circularly polarized illumination. (a) Plots of $|E|^2$ and $|E_z|^2$ along the *x*-axis for phase FZP (glass with etch depth of 200 nm) and amplitude FZP (Au coating of 200 nm thickness) in the focal plane. (b) Intensity distribution in the focal plane for amplitude FZP.

4.6 Rotationally Symmetric Focusing with Radially Polarized Illumination

Linear and circular polarized beams have state of polarization independent of the spatial co-ordinates in the cross-section of the beam. They are referred as homogeneous polarization states [115]. Radial polarization belongs to the category of beams having inhomogeneous state of polarization wherein state of polarization is dependent of spatial co-ordinates in the cross-section of the beam. Moreover, radial polarized beams obey radial symmetry in both amplitude and polarization, i.e. direction of field vector varies locally and points along radial direction away from the optical axis. Such beams are also termed as doughnut mode as field along the axis reduces to zero owing to the symmetry.

Radial polarization is gaining interest due to promising results in applications like material processing [116], optical data storage [117], microscopy [118], optical trapping [119] and plasmonic focusing [109, 120, 121]. The laser machining with a radially polarized beam can be about 2 times more efficient than with a linear polarized beam due to the polarization dependence of absorption of metal materials [122]. It has also been shown that, due to inherent symmetry, a radially polarized light beam can be focused to a much sharper spot than a linearly polarized light.[107, 108, 121, 123].

The axial symmetrically polarized mode can be viewed as the superposition of the two linearly polarized Hermite–Gauss HG_{01} and HG_{10} modes, if their planes of polarization are perpendicular to each other and the phase shift equals zero [124].

$$\left.\begin{aligned} E_r &= HG_{10}\overrightarrow{E_x} + HG_{01}\overrightarrow{E_y} \\ E_\phi &= HG_{01}\overrightarrow{E_x} + HG_{10}\overrightarrow{E_y} \end{aligned}\right\} \tag{4.8}$$

where E_r and E_ϕ denote radial and azimuthal polarization, respectively. Figure 4.15(a) shows polarization vector spatial distribution of radial and azimuthal polarized beams.

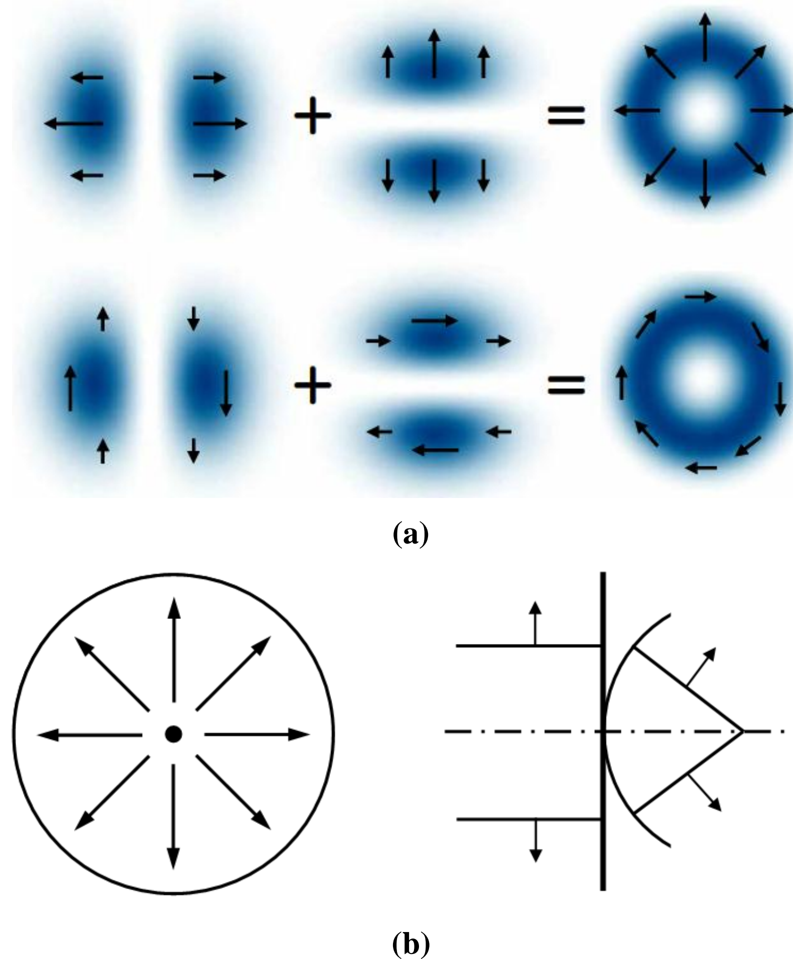

Figure 4.15 (a) Radial and azimuthal porlarization as a linear superposition of orthogonally polarized Hermit-Gaussian modes. (b) Polarization vectors after focusing of a radially polarized beam by FZP.

For azimuthally polarized field, a paraxial wave equation has been developed by Jordon and Hall [115]. The solution consists of a plane-wave propagation factor multiplied by a Bessel function of the first kind of order one, and a Gaussian factor, which describes the transverse characteristics of the beam. Further, Youngworth and Brown [125] have formulated a procedure to obtain the electric field in the paraxial region for radial and azimuthal polarization.

If the phase FZP is illuminated by a radially polarized light, Equation (4.1) can be rewritten as [125]:

$$\mathbf{E} = \begin{pmatrix} E_x \\ E_y \\ E_z \end{pmatrix} = \frac{-iA}{\pi} \int_0^{\alpha} \int_0^{2\pi} BC \exp(ik(\hat{\mathbf{s}} \bullet \mathbf{r})) \begin{pmatrix} \cos\theta\cos\phi \\ \cos\theta\sin\phi \\ \sin\theta \end{pmatrix} \sin\theta d\theta d\phi \tag{4.9}$$

In the image plane, azimuthal and radial components can be derived from cartesian components of the fields as:

$$\left.\begin{aligned} E_\phi &= E_y\cos\phi - E_x\sin\phi \\ E_r &= E_x\cos\phi + E_y\sin\phi \end{aligned}\right\} \tag{4.10}$$

Further, using Bessel-Gauss beam approximation [125, 126],

$$l_\theta = \exp\left(-\beta_0^2\left[\frac{\sin\theta}{\sin\alpha}\right]^2\right) J_1\left(2\beta_0\frac{\sin\theta}{\sin\alpha}\right) \tag{4.11}$$

where β_0 is the ratio between the pupil radius and the beam waist.

For a radial polarization, azimuthal component (E_ϕ) will be zero in image space. Hence, Equation (4.9) can be simplified to [111]:

$$\left.\begin{aligned} E_r &= A\int_0^{\alpha} BCl_\theta \sin(2\theta) J_1\left(\frac{v\sin\theta}{\sin\alpha}\right)\exp\left(\frac{iu\cos\theta}{\sin^2\alpha}\right)d\theta \\ E_z &= 2iA\int_0^{\alpha} BCl_\theta \sin^2\theta J_0\left(\frac{v\sin\theta}{\sin\alpha}\right)\exp\left(\frac{iu\cos\theta}{\sin^2\alpha}\right)d\theta \end{aligned}\right\} \tag{4.12}$$

It is interesting to investigate the focusing characteristics of a phase FZP under the illumination of a radially polarized light. This is because the radially polarized illumination bearing an azimuthal symmetry can produce a rotationally symmetric focal spot with a narrow focused beamwidth [108, 127]. For the case of radially polarized beam, the electric field vectors are oriented as shown in Figure 4.15(b). After focusing field vectors add in the focus to an axial component (E_z) and this is the case for all planes containing the optical axis. This is in contrast with the focusing under linear polarization as discussed (Figure 4.2(a)). Figure 4.16 compares $|E|^2$ ($=|E_z|^2 + |E_r|^2$) and $|E_r|^2$ of the focal spot obtained by Equation (4.12) and FDTD method for the SiO_2 phase FZP with NA = 0.996 and $\Delta = \pi$. It is noted that 1) our analytical model matched well with the FDTD method and 2) the beamwidth of the focal spot along the x-axis is significantly reduced from 555 to 250 nm when compared with the case under the illumination of linearly polarized light. Furthermore, it is found that the side lobe intensity is reduced from 20% to 15% of the axial intensity. The decrease in side lobe intensity may be attributed to the large intensity of $|E_z|^2$ at the centre of the focal plane. This suggested that the multiple apertures of phase FZP can focus the radially polarized light more effectively.

Figure 4.17 gives detailed break up of electric field intensity into Cartesian components. Contribution of the transverse components of the field (E_x and E_y) is reduced and incident energy is focused along axial direction. Hence a strong longitudinal component of the electric field (E_z) is observed. Total intensity profile is dominated by $|E_z|^2$ and the focal spot is rotationally symmetric [111].

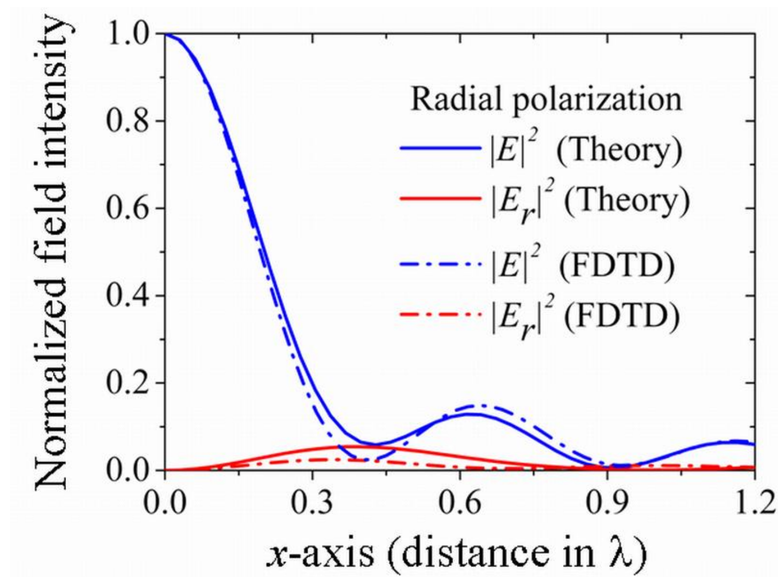

Figure 4.16 Plots of $|E|^2$ and $|E_r|^2$ along the x-axis for the phase FZP with 8 zones (NA = 0.996) and $\Delta = \pi$ under illumination of radially polarized light. Solid and dashed lines represent the calculation obtained from the analytical model and FDTD simulation respectively.

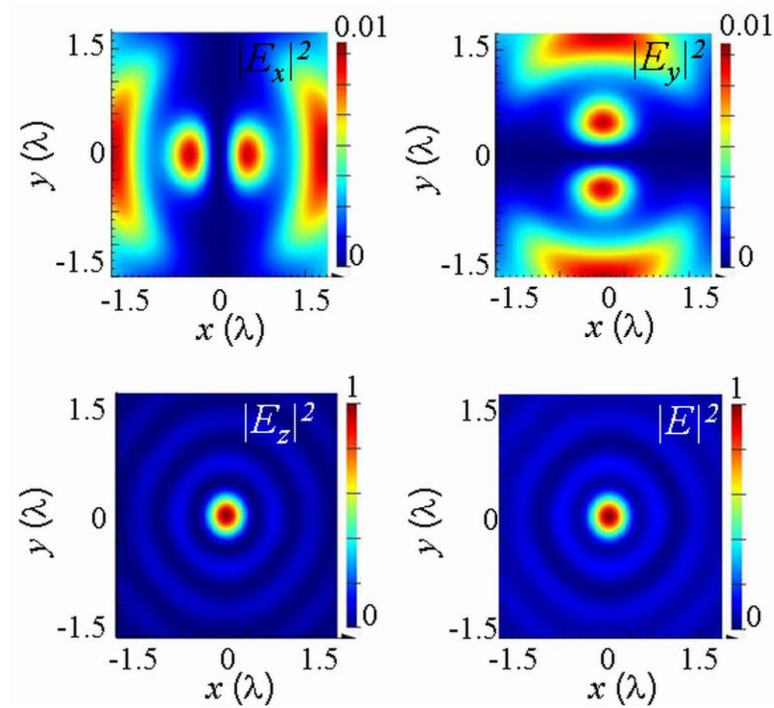

Figure 4.17 Detailed intensity distribution obtained by FDTD simulations for phase FZP under radially polarization illumination.

From the above analysis, it is evident that the use of radial polarization essentially achieves conversion of polarization from incident transverse polarization to focused longitudinal polarization. Moreover, such conversion is achieved with a tighter focal spot breaking the conventional resolution limits [111]. Such stronger longitudinal component may be useful with NSOM tips as strong field enhancement is demonstrated theoretically [128] when illuminated with longitudinally polarized light than transversely polarized light. Thus, much smaller spot size can be attained resulting in improved resolution for microscopic applications.

4.7 Summary

In summary, we have extended Richard and Wolf's vector formalism to predict the focusing behavior of high NA binary phase FZPs for linearly polarized and radially polarized light [111]. From the model, it is found that the high NA phase FZP under the illumination of linearly polarized light can produce rotationally asymmetric focal spot. This is because the value of $|E_z|^2$ is comparable with that of $|E_x|^2$ for the linearly polarized light after focusing by the phase FZPs. Furthermore, the value of $|E_z|^2$ can be reduced with the reduction of Δ (i.e. the etch depth). The results deduced from the proposed model shows qualitative agreement with that obtained from the FDTD method. Thus, the proposed formulation is useful in simplifying the analysis compared to rigorous diffraction calculations. The illumination of a radially polarized light can produce a rotationally symmetric focal spot. This is because the intensity of total electric field, $|E|^2$ $(= |E_z|^2 + |E_r|^2)$ is dominated by $|E_z|^2$. As a result, a focal spot with a beamwidth of 250 nm (0.39λ) can be obtained.

Chapter 5

Near-Field Focusing of Fresnel Zone Plates (FZP) Under Linearly Polarized Illumination: Fabrication and Characterization Issues

In this chapter, application of focused ion beam (FIB) technology to fabricate the Fresnel zone plates (FZP) on a metal-coated glass (amplitude FZP) and on a bare glass substrate (phase FZP) is discussed. Near-field focusing of a linearly polarized light by a large NA phase FZP is demonstrated experimentally. The focusing characteristics of phase FZP are measured by a near-field scanning optical microscope (NSOM).

5.1 Fabrication of FZP using FIB

In the present work, the FZP structure was realized by using a FIB technology (FEI quanta 200 3D dual-beam system). The instrument has a dual-beam capability combining a scanning electron microscope (SEM) and a FIB with the two beams focused at the same spot. The FIB system provides ion beam current in the range 1 pA to 20 nA with accelerating energies upto 30 keV.

5.1.1 Amplitude Zone Plates

In order to realize an amplitude zone paltes with an opaque coating on a glass substrate, complete milling of an opaque film exposing the glass beneath is required.

Overmilling i.e. milling a substantial portion of the glass can ensure a complete removal of the opaque film from the glass. But, overmilling in turn modifies the surface profile of the glass and may cause line broadening effect leading to the broadening of zone plate features. To know whether the glass surface has rearched or not during milling, an end point monitor (EPM) graphs can be recorded. Real-time EPM shows a sample absorbed current as a function of the sputtering time during FIB milling process. Sample absorbed current roughly follows a linear relationship with the ion beam current for the same material. Sample absorbed current signal includes the information from all the charged particles generated during the milling [129]:

$$I_{sample} = I_{Ib} + I_{se-} - I_{si+} \tag{5.1}$$

where I_{sample} is the sample absorbed current, I_{Ib} the incident ion beam current, I_{Se}- the current formed by ion-induced secondary electrons and I_{Si+} the current formed by ion-induced secondary ions.

Figure 5.1(a) shows the zone plate design used for FIB fabrication. The zone plate dimensions are based on the approximate formulation of Fresnel zone plates as given by Equation 3.3. Figure 5.1(b) shows SEM image of the zone plate structure milled on *Ag* coated glass. The EPM graph in shown in Figure 5.1(c), showing the sample absorbed current in the unit of *pA* against the sputtering time. Little variation of ion beam current or inhomogeneous composition of film material account for the noise in the curve. Drop in a specimen current is observed as milling reduces the thickess of *Ag* layer and glass i.e non-conductive surface is approached. Milling was terminated as decreasing current just starts to saturate at a lower value. This is an indication of a complete removal of exposed *Ag* film and a glass surface is open. Thus, the optimum milling time was identified and further used to create array of zone

plates. Similar procedure was adopted to optimize the milling time for other zone plate designs and are listed in Table 5.1.

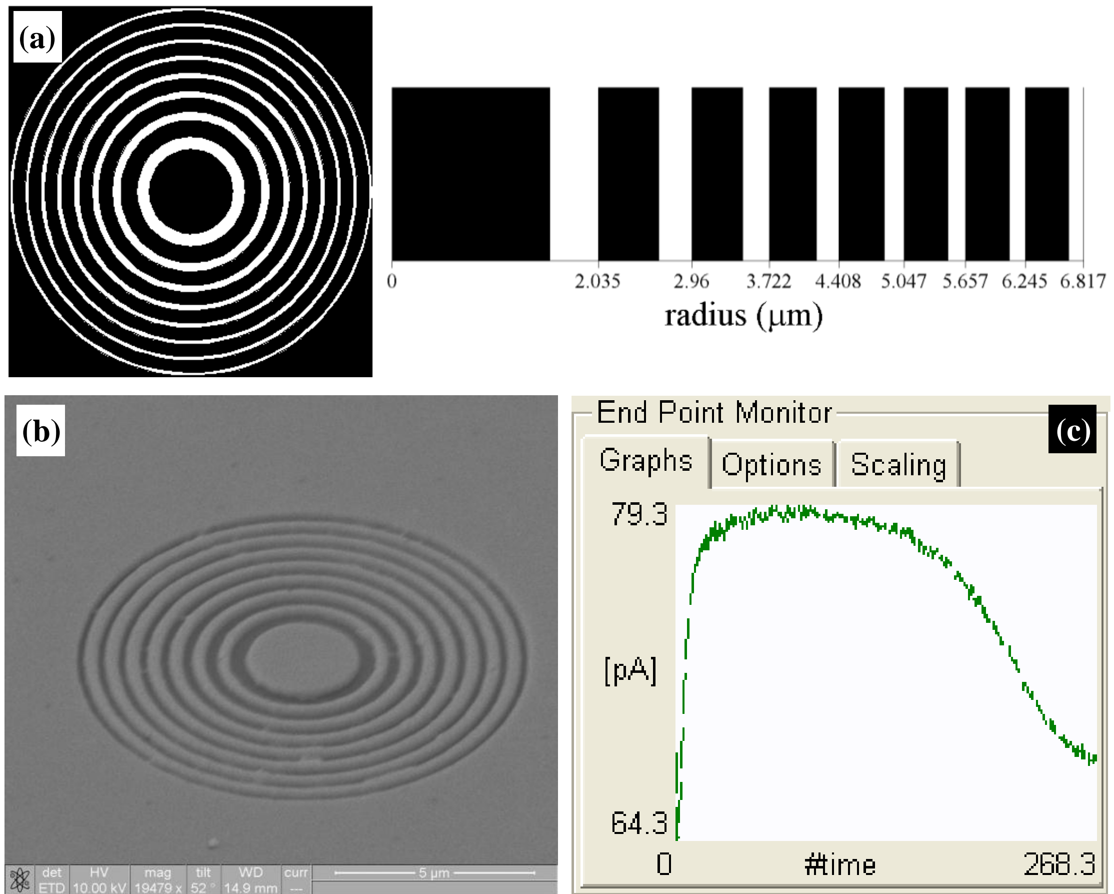

Figure 5.1 (a) Zone plate design used for fabrication (b) FIB milled zone plate on *Ag* coated glass (focal length 4 μm, λ = 488 nm) as per design shown in (a). (c) End point monitor graph for milling at beam current 30 pA, milling time 269 s.

Table 5.1 Optimized FIB milling time for different zone plate designs. Ion beam current = 30 pA, dwell time = 1 μs.

Focal length (μm)	**Wavelength (nm)**	**Diameter (μm)**	**Milling time (s)**
1.0	488	9.60	165
2.0	488	11.11	230
4.0	488	13.62	269
1.0	527	10.34	135
0.5	633	11.08	209
1.0	633	11.96	137

Figure 5.2 depicts SEM images of 4×4 arrays fabricated with the milling parameters listed in Table 5.1. Quality of the milled surface is mainly governed by the uniformity of *Ag* film. Careful observation of the patterns reveals that traces of *Ag* are not milled. To remove such traces prolonged milling is required. But, prolonged milling may damage the glass substrate and line broadening effect may broaden the fine features of the zone plate.

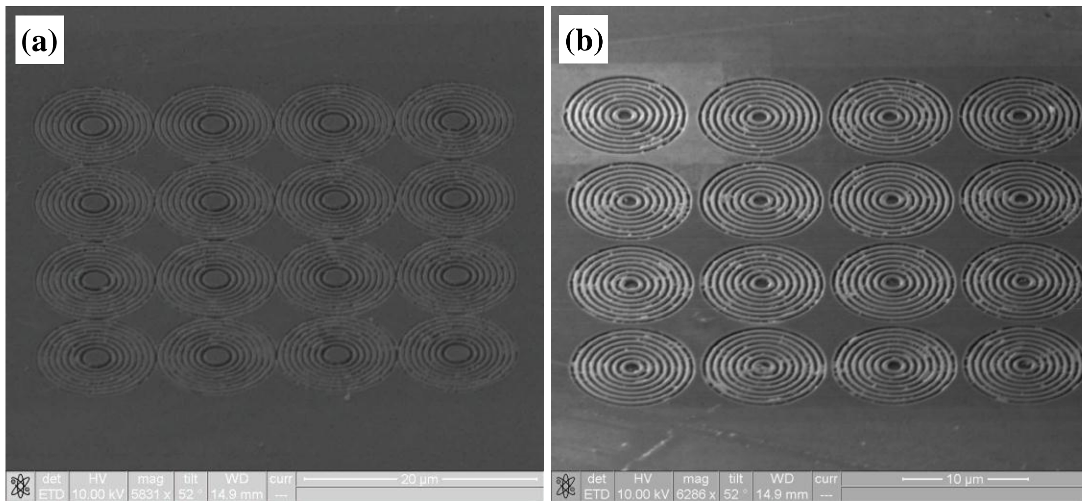

Figure 5.2 SEM images of zone plate arrays on *Ag* coated glass with focal length (a) 4 µm (λ = 488 nm) and (b) 1 µm (λ = 633 nm).

5.1.2 Phase FZP

To fabricate phase type FZPs, a glass substrate is used. However, poor conductivity of a bare glass may cause built up of charges under ion/electron beam exposure. In order to minimize the charging effects during fabrication, a conductive layer of ITO (~ 50 Ω/sq. inch) was coated on the glass substrate. Two different scanning modes are possible to pattern using FIB, i.e. serial and parallel milling. In case of serial milling all patterns defined on the screen are milled sequentially i.e. milling is not started on the next pattern unless completion of milling of one pattern. When selecting the parallel milling, all patterns are defined on the screen are milled simultaneously. Using

this approach, a temporal accumulation of surface charges, which may lead to shift of successive zones locations (see Figure 5.3), is avoided and a milled material redeposition is minimized.

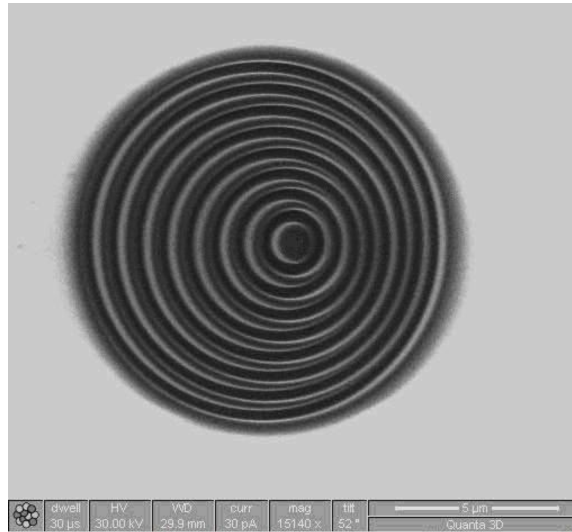

Figure 5.3 Pattern shift due to charge accumulation under serial milling with ion beam current of 30 pA.

Figure 5.4 (a) and (b) show FIB milled phase FZPs with focal lengths of 5 µm and 2 µm respectively on ITO coated glass. Lower beam current values ensures higher patterning resolution however the number of pixel to be milled (pattern size) put constraints on lowest current that can be used. Considering this fact, ion beam current was set at 50 pA with an accelerating voltage of 30 keV to mill a target depth of 200 nm. Resulting patterns were scanned with atomic force microscope (Dimension-3000 AFM from Digital Instruments) used in tapping mode for geometrical characterization. Figure 5.4(c) shows depth profile of FZP zones. The sidewalls are not vertical; instead, they are tilted by an angle in the range 50-60°. Non-vertical sidewalls are result of a Gaussian profile of the ion beam and redeposition of milled material onto the roots of sidewalls [130-132]. Such FIB milled trenches having a shape is similar to “V” often influences performance of the device [41, 133] and hence it is important to control the

tilt of the sidewalls. It is possible to control tilt in sidewalls by reducing beam current and dwell time as well as with the gas assisted etch (GAE). However, as described in Section 5.2.2, GAE results in change material characteristics due to implantation of gas molecules in addition to Ga^+ ions. We must note here tilt angles are overestimated, as AFM probes may not follow the exact groove profile. Such AFM measurement limitations arisen mainly due to the large cone angle (~ 34°) of the pyramid shaped probe [42].

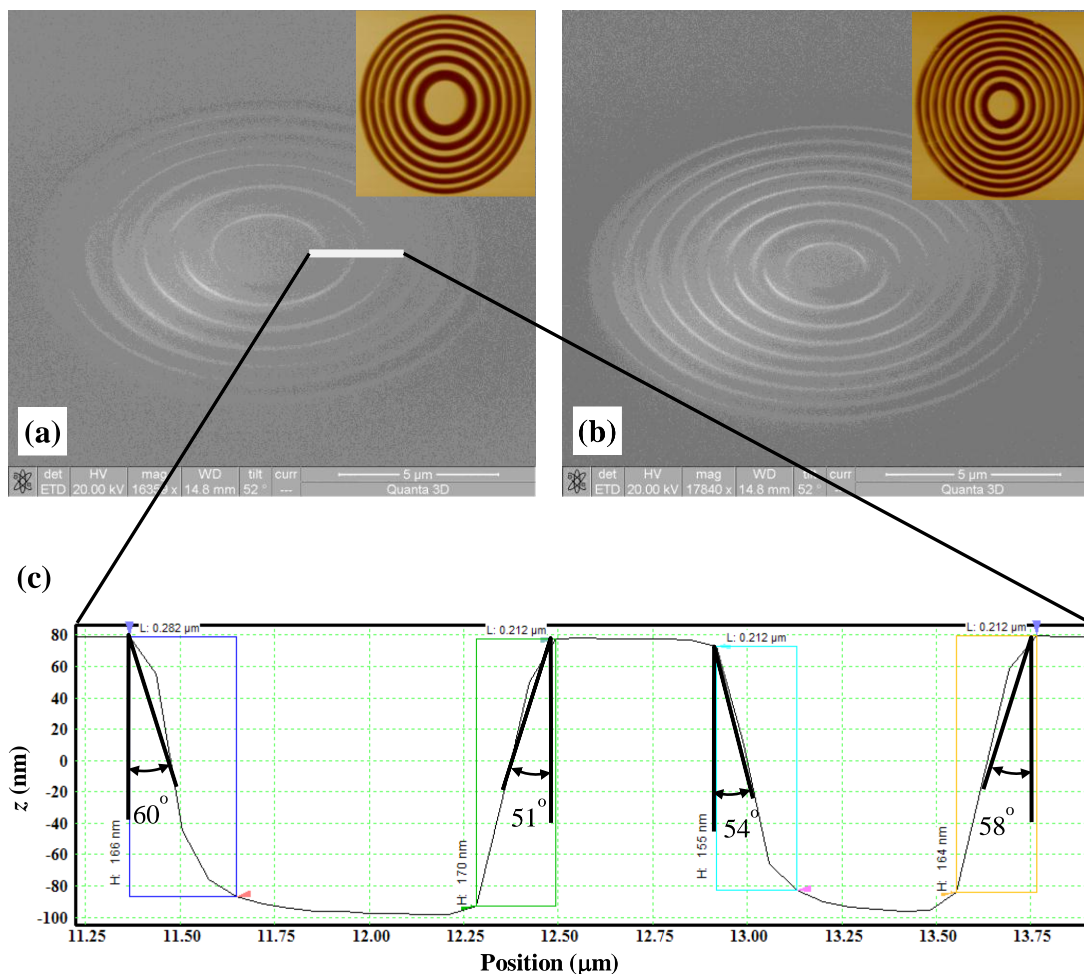

Figure 5.4 FIB fabricated phase FZPs in glass with focal lengths (a) f = 5 μm and (b) f = 2 μm (λ = 633 nm). Inset shows corresponding AFM scan image. (c) Zone profile by AFM measurements showing tilted sidewalls for a phase FZP shown in (a). For FIB milling, beam current was set to 50 pA with a dwell time of 1 μs.

For the case of a phase FZP with 500 nm focal length, we have studied the influence of non-vertical sidewalls on focusing characteristics with FDTD simulations. In order to represent tilted sidewalls, a refined mesh of 8 × 8 × 8 nm^3 is used in the FZP region and 15 × 15 × 15 nm^3 elsewhere. In order to minimize memory requirements, a 200 nm etch depth is used for simulations. Tilt of side walls is considered in two configurations: the designed zone width is maintained at 1) center and at 2) base of the zone depth as shown in Figure 5.5. The design is found to be more tolerant to the sidewall tilts if the designed zone width is maintained at the center because phase errors introduced are compensated due to the complementary nature of tilts above and below the centerline [134]. The focusing intensity is reduced by 20% when the tilt angle is 45°. However, with the other configuration, the intensity reduces by 75%. This may be attributed to increased diffractive scattering losses as the zone width is broadened across the zone height.

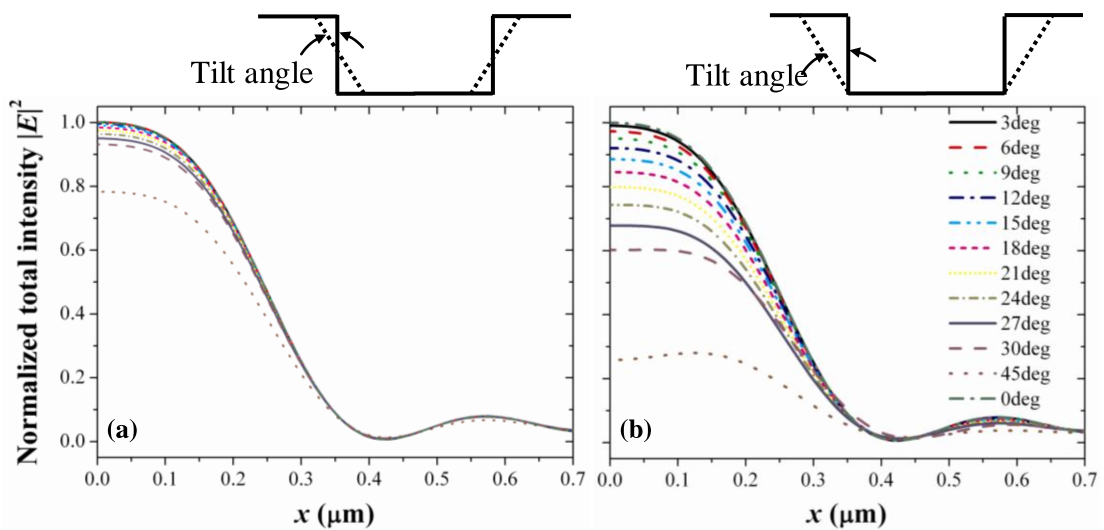

Figure 5.5 Influence of zone wall tilt on focusing intensity ($|E|^2$) of phase FZP calculated by FDTD simulations. The designed zone width is at (a) center and (b) bottom of groove. Intensities are normalized by electric field intensity calculated with vertical sidewalls (i.e. tilt angle = 0). Phase FZP has a focal length of 0.5 μm (λ = 633 nm).

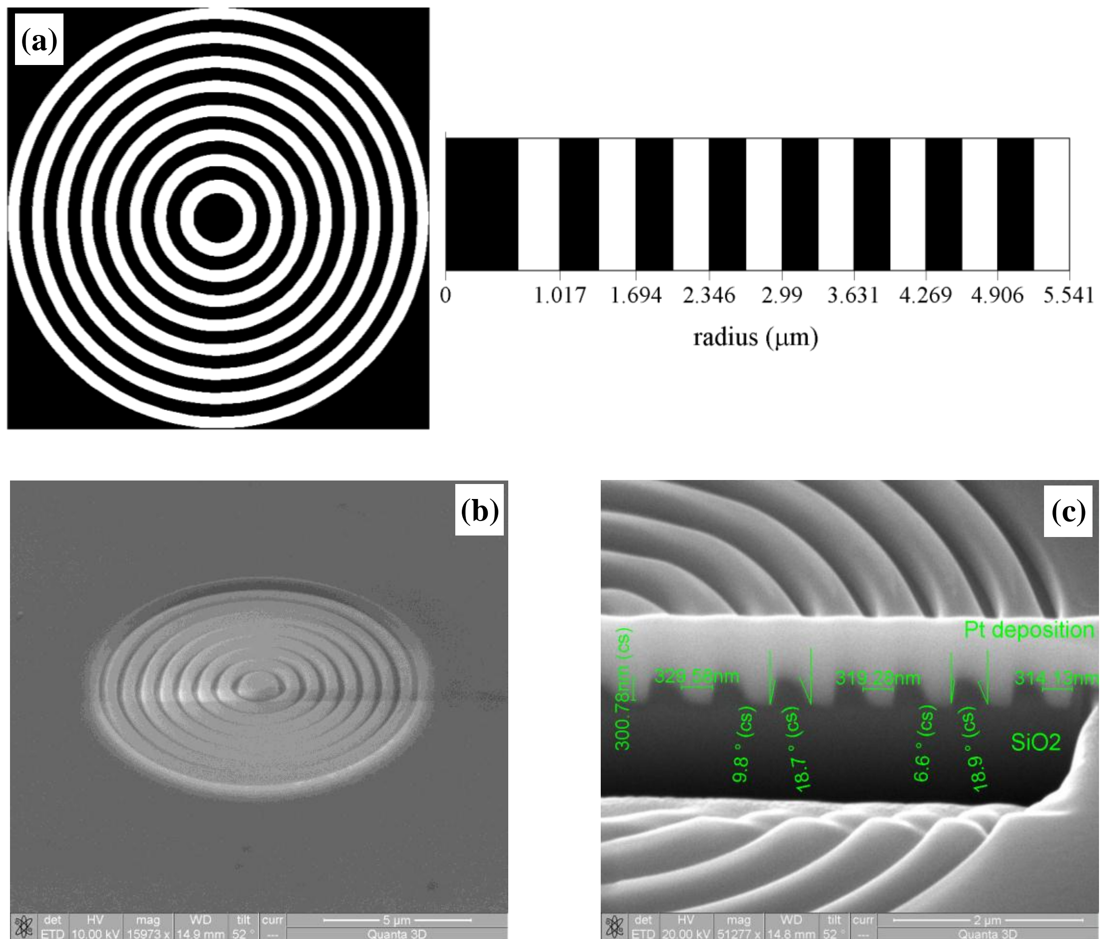

Figure 5.6 (a) FZP design for 500 nm focal length at λ = 633 nm and zone profile used for fabrication. (b) SEM image of phase FZP used for NSOM measurements. (c) SEM image of FIB sectioned phase FZP with focal length 0.5 μm. For fabrication, beam current was set to 30 pA and dwell time to 500 ns with a total milling time of 45 min. Design zone widths are observed at the center of zone depths.

Figure 5.6(a) shows the FZP design (500 nm focal length at λ = 633 nm). The variation in the zone width across different zones is small, so the zones might appear visually to have equal dimensions, but the zone plate designed is in fact of Fresnel type. For the fabrication of phase FZP with 500 nm focal length, we have used 30 pA beam current and 500 ns dwell time. A target 300 nm etch depth is considered to ease the fabrication. Lugstein et al [135] showed that for aspect ratios beyond one, redeposition becomes the dominant effect limiting aspect ratio. With these parameters,

FIB milling was carried out for approximately 45 min. Figure 5.6(c) shows a SEM sectional view of the FZP structure. Platinum was deposited at a beam current of 0.1 nA over the region to be sectioned in order to protect the structure during sectioning and to improve the contrast during imaging. Sidewall tilts are found to be less than 20° and the designed zone width is maintained at the center. For optical characterization, structure shown in Figure 5.6(b) is used. Near-field scanning optical microscope (NSOM) is used for this purpose and details are as described in following sections.

5.2 Optical Characterization using Near-field Scanning Optical Microscope (NSOM)

The first concept of the optical near-field microscope, which is to use a small aperture to image a surface with a resolution smaller than the wavelength of light, was proposed by Synge in 1928 [136]. In 1972, Ash and Nichols [137] first demonstrated a near-field resolution using microwaves. Twelve years later the first implementation of NSOM was reported by Pohl et al [138] and by Lewis et al [139]. Their experiments involved a subwavelength size aperture which they fabricated by coating the apex of a sharply tapered transparent glass tip with metal. In addition, they employed a feedback loop mechanism that maintained a constant distance of only a few nanometres. In 1991 Betzig et al [140] introduced the use of a single-mode optical fibers as near-field optical probes; this is still one of the most popular set ups.

In general, NSOM measurements are possible in configurations as shown in Figure 5.7. Transmission mode is suited for transparent samples while opaque samples can be analyzed with reflection mode. Further adaptations are possible depending upon application requirements. There are two types of NSOM probes: the aperture type and the apertureless type. An apertureless probe is essentially a sharp object,

which scatters the evanescent field into the far-field when placed closed to the surface. Scattered field is then collected by photo-diode. However, apertureless probes can scatter directly transmitted field i.e. far-field radiation, such probes are more suitable for scanning fields containing evanescent component only. An aperture type probe has dielectric transparent core coated with a reflective (usually metallic) coating. Such coating prevents the leaking of fields through the sides of the probe. The most common example is a tapered optical fiber coated with metal like aluminum. Aperture probes are available in the two popular configurations as shown in Figure 5.8. First type is micro-fabricated cantilever probes, which is structurally similar to the AFM cantilever probes except hollow subwavelength aperture in the pyramid shaped apex. Such cantilever probes can be produced with excellent reproducibility. The other type of probe is made from tapered optical fibers with thin metallic reflective coatings.

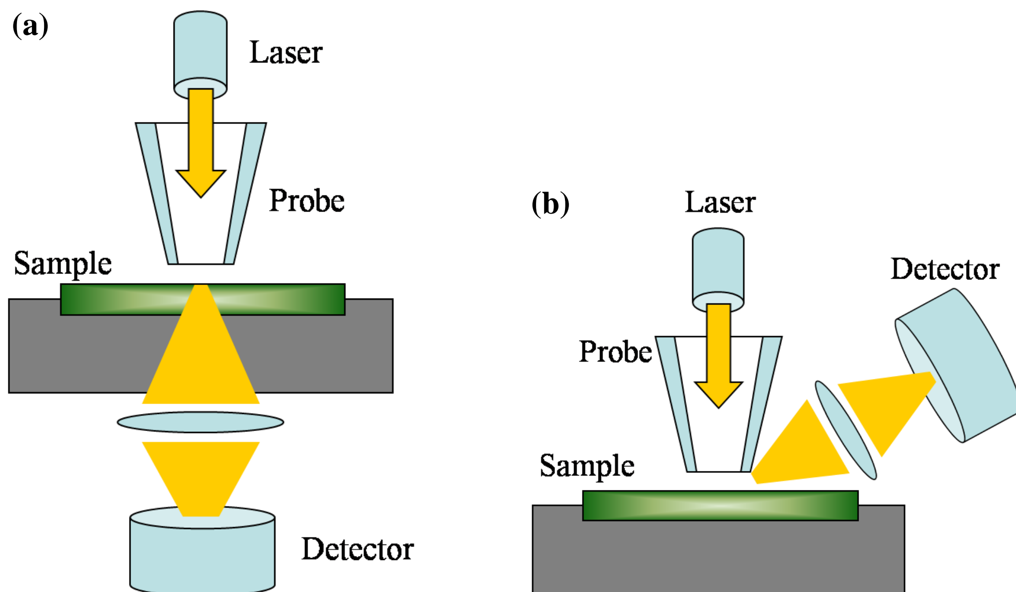

Figure 5.7 Various NSOM configurations: (a) Transmission mode and (b) Reflection mode.

The distance between the NSOM probe and the sample surface is controlled through a feedback mechanism that is independent of NSOM signal. Currently, most

instruments use one of the following two types of feedback: normal force or shear force. The normal force feedback mechanism is standard feedback mode used in AFM. However, this feedback mechanism is only possible with cantilevered NSOM probes with holes. In the shear force feedback [141, 142], or tuning fork feedback, the probe is mounted/glued to a tuning fork, which acts as a crystal resonator. With the aid of piezoelectric vibrator, the fork is set into oscillations parallel to the sample surface at a frequency close to the resonance frequency of the probe and quartz resonator system. Mechanical oscillations of the quartz induce a voltage response, which is used as an information signal about amplitude of the probe oscillation. Measurement of tip-surface interaction force is then made by recording the changes of amplitude and phase shift with respect to the driving voltage applied to the piezo-electrodes. As the probe approaches the sample surface, greater shear force is exerted on the fork and thus dampening the amplitude of the vibrations. As a result corresponding voltage response of fork is reduced. By monitoring voltage response, electronic control system then maintains a constant sample-probe distance during measurements. The effect of shear force is usually observed below 50 nm working distance depending upon quality factor of the tuning fork [142].

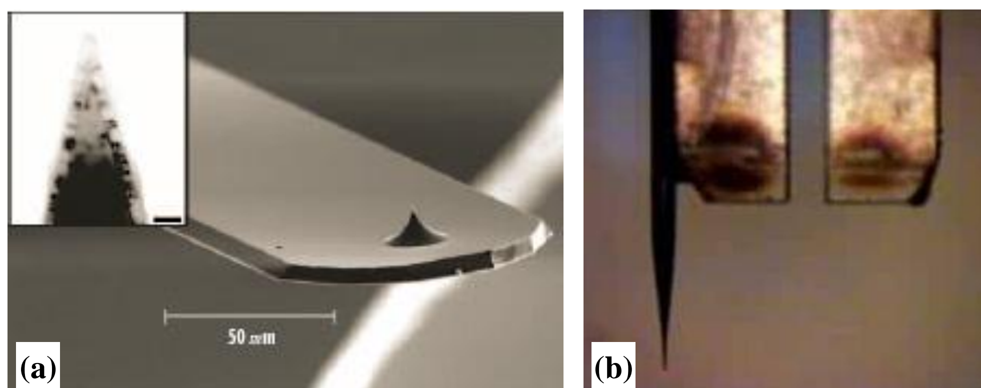

Figure 5.8 Commonly used NSOM probes (a) Cantilever probe [143] (b) Optical fiber probe attached to a tuning fork [144].

In the present work, optical measurements were carried out by a NSOM (NTEGRA NT-MDT) operating in a collection mode. Figure 5.9 shows the configuration of the measurement [134]. A linearly polarized helium-neon (@ 632.8 nm) laser, whose polarization angle can be adjusted by a half-wave plate, was used as the illumination source. The laser beam was weakly focused onto the substrate of the phase FZP by means of a microscope objective lens (Olympus UPLFLN/4X). An *Al*-coated probe, which was glued to a quartz tuning fork, was employed to collect a light emission from the surface of the phase FZP. The probe has an average aperture diameter of 100 nm in order to ensure a subwavelength resolution of the system. Light collected from the probe will then be coupled to a photomultiplier through an optical fiber. Electric field intensity was mapped to the phase FZP by scanning the probe over its entire surface. Using the tuning force sensing shear feedback mechanism of the NSOM system, the probe was kept in a constant distance above the surface of the phase FZP during the scanning process. For every pass of a scan at a certain height, the first pass was carried out at about 10 nm distance. With a reference to the first pass using a shear force feedback mechanism, the probe was moved to a required height above the surface. A topographical signal and optical signals were collected simultaneously for all measurements.

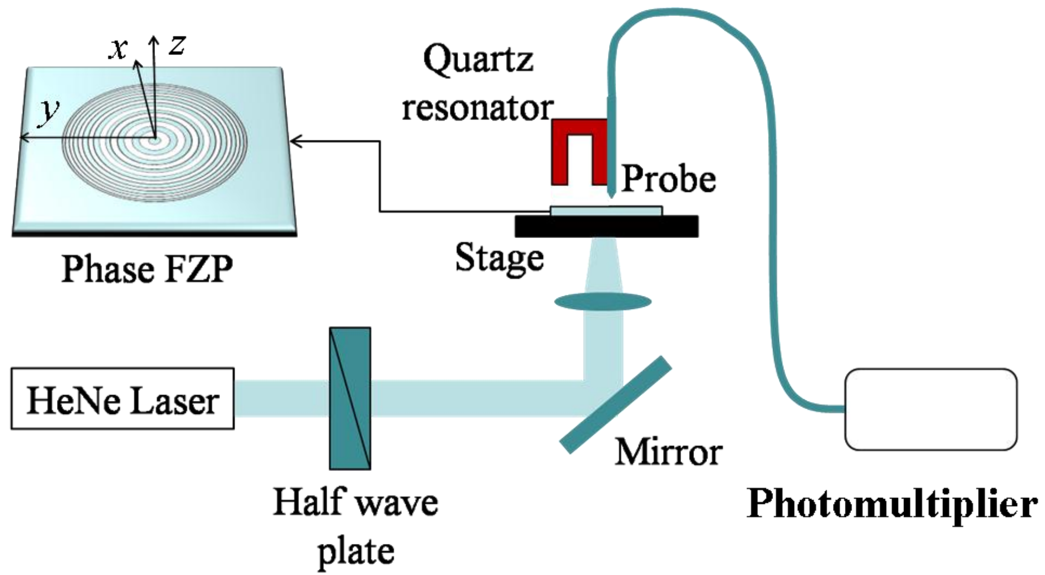

Figure 5.9 Near-field measurement set-up.

Figure 5.10(a) and (b) shows topographical profile obtained from NSOM measurements of the phase FZP, and SEM micrograph respectively. The etch depth of FZP is found to be about 300 nm.

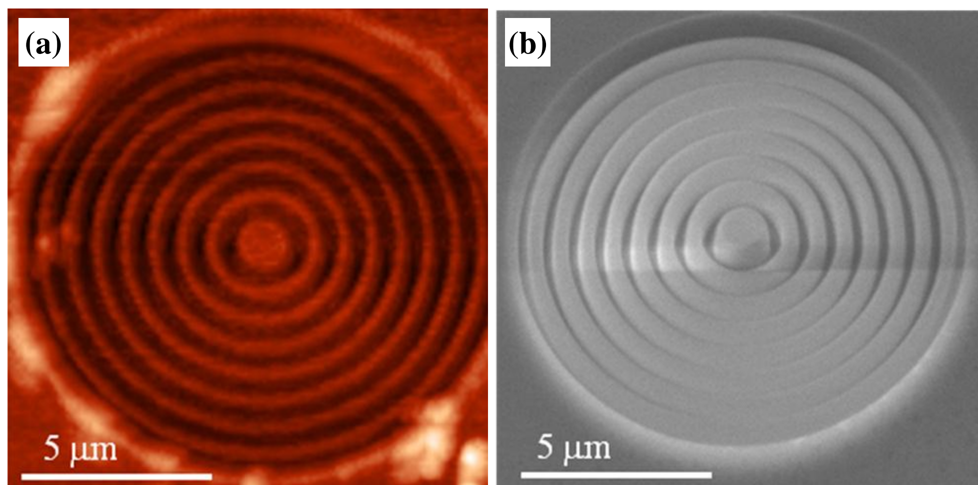

Figure 5.10 Topography of FIB fabricated FZP (a) NSOM topograph and (b) corresponding SEM micrograph for comparison.

5.3 Results

Figure 5.11 shows the intensity patterns of the illumination light after passing through the phase FZP. The intensity patterns on the *x*-*y* plane (i.e., parallel to the surface of the phase FZP) are measured from some distance, *z*, above the surface of the phase FZP. Figure 5.11(a) records the intensity pattern at $z \sim 10$ nm above the surface of the phase FZP. It is noted that the intensity pattern is dominated by the interference of diffracted evanescent waves. No focusing is observed at this value of *z*. Figure 5.11(b) to (d) show the focusing characteristics of the illumination light at a distance *z* varying between 525 and 750 nm from the surface of the phase FZP. It is observed that all the focal spots have a rotationally asymmetric profile. Focal spots are broadened along the *x*-axis (i.e. polarization direction) when compared to that along the *y*-axis. This is because the phase FZP bears a high numerical aperture (NA = 0.99). When a high NA focusing system is illuminated by a linearly polarized light, the vectorial nature of the light makes resolutions substantially different in the plane of polarization [105, 106]. Hence, the diffracted waves do not add up perfectly at the focus along the polarization direction. As a result, the focal spot appears to be broadened along the polarization direction. On the other hand, the high intensity is observed from the region outside the FZP structure is due to the direct transmission of illumination light through the glass substrate.

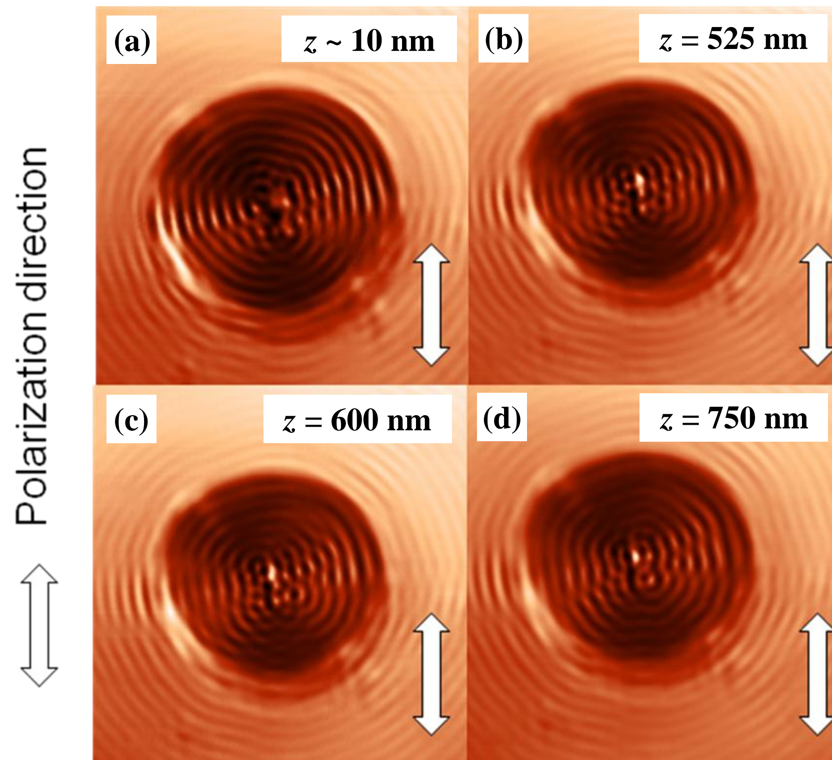

Figure 5.11 Profiles of electric field intensity after transmitted through the phase FZP at planes located at (a) z ~ 10 nm, (b) z = 525 nm, (c) z = 600 nm and (d) z = 750 nm from the surface of phase FZP. Incident polarization is shown with solid white arrow.

Focusing behavior of the phase FZP is also analyzed by using a complete vectorial FDTD simulation. In simulations, the etch depth of FZP was set at 300 nm. Figure 5.12(a) and (b) give the calculated total intensity profile of the focusing beam in the x-z (at y = 0 nm) and x-y (at z = 630 nm) planes respectively. It is observed that the focused beam has an asymmetric profile and is broadened along the polarization direction similar to that observed from the experiment results [134]. Figure 5.12(c) compares the electric field intensity obtained from FDTD simulation and NSOM measurements along the propagation direction (i.e., z-axis) at the location x = 0 and y = 0. Experimental results have shown that the focal length of the phase FZP is about 700 nm and this value is close to that obtained from the FDTD calculation (i.e., 630 nm).

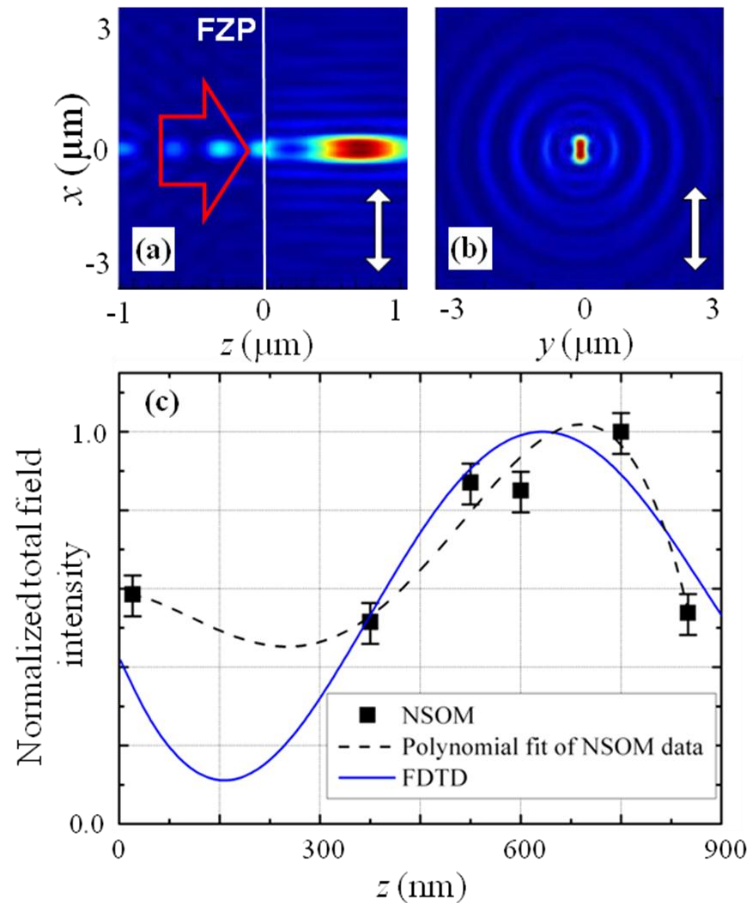

Figure 5.12 Plot of normalized total electric field intensity, $|E|^2$, after transmitted through the phase FZP along (a) *x*-*z* plane and (b) the focal (*x*-*y*) plane located at z = 630 nm obtained from the FDTD simulation. The incident polarization is shown with a solid white arrow. (c) Comparison of total intensity obtained by FDTD results and NSOM measurements along propagation direction (*z*-axis). Error bar depicts forth-order polynomial fit to NSOM data standard deviations (upper error bars) and measurement error (lower error bars).

However, the designed focal length of FZP based on Equation (4.1) is 500 nm, which is much shorter than the measured focal length. This is because Equation (4.1) fails to take into account the coupling between diffracted and evanescent waves under high NA focusing condition in the design of FZPs. On the other hand, highly intense focusing is seen over a distance of 250 nm (i.e., from z = 500 to 750 nm) along the *z*-direction. Such an elongated depth of focus is also in agreement with FDTD calculations shown in Figure 5.12(a).

Figure 5.13(a) and (b) show measured focal field profiles at a distance z equal to 600 and 750 nm respectively from the surface of the phase FZP. The FDTD calculation of the focal field profile is also plotted in the figures for comparison. The measured focal field profiles along the x- and y-axes are agreed qualitatively with that of the FDTD results. The spot size (FWHM) is measured to be about 600 and 400 nm along the x- and y-axis respectively in the plane of maximum intensity (i.e. z = 750 nm), see Figure 5.13(b). As the illumination light has a wavelength of 632.8 nm, it is verified that the phase FZP can achieve subwavelength focusing of the light beam. It is also observed from the figures that the focal spots along y-axis are accompanied by high intensity side lobes. As focal spot along the y-axis is tighter than that along the x-axis, the intensities of the side lobes must increase due to the principle of energy conservation. Such high-intensity side lobes have been predicted during tighter focusing with the aid of aperture plates [145, 146] and often deteriorate the resolution. However, the intensity of side lobes obtained from the measurement is found to be higher than that obtained from the FDTD calculation. This may be due to the poor diffraction efficiency of the incident waves by the zones of the phase FZP. Nevertheless, the consistency between experimental results and computer simulations has verified that the use of phase FZPs to achieve high efficiency near-field focusing is practicable [134].

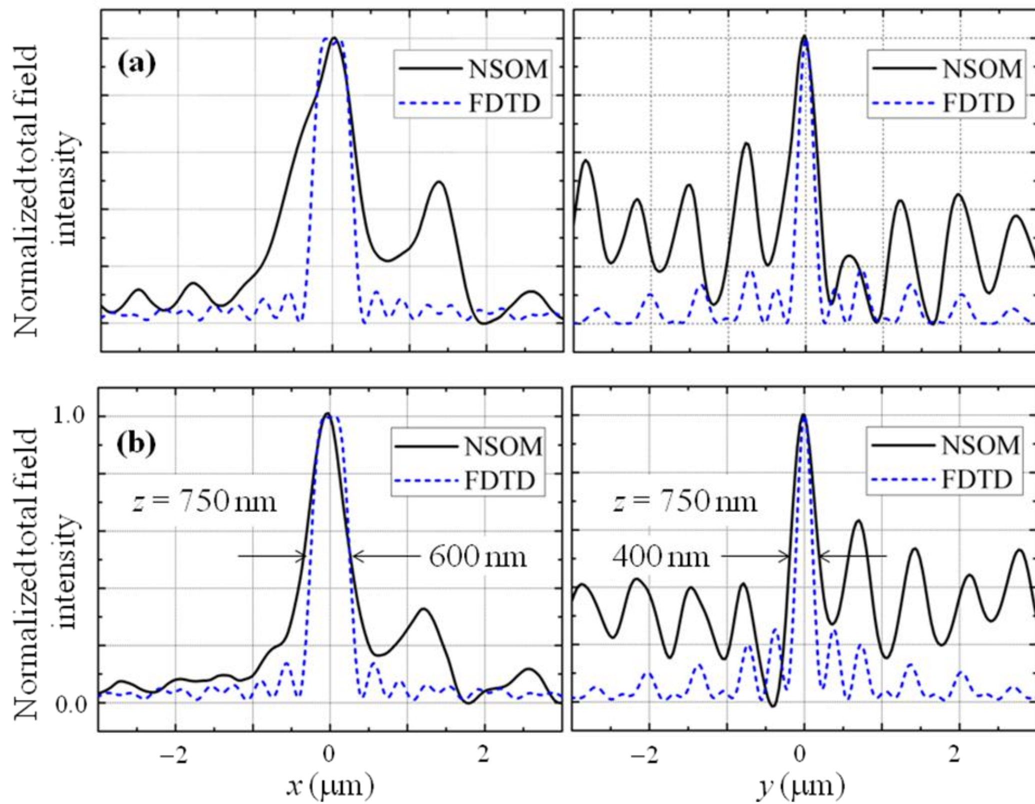

Figure 5.13 Plot of normalized total field intensity, $/E/^2$, after passing through the phase FZP in the *x*-*y* plane obtained from the NSOM measurement (solid lines) and FDTD simulation (dashed lines). (a) z = 600 and (b) z = 750 nm.

The excitation of side lobes can be attributed to the poor diffraction efficiency of the zones of the phase FZP. This is mainly due to the FIB fabrication process induced structural damage to the phase FZP. Ion-solid interaction in FIB is inherently destructive as it involves ion implantation into the target surface (i.e., glass substrate), redeposition or selectively removal of target atoms [147, 148]. Optical properties of the target material such as refractive index may be altered by the ion-beam bombardment [149]. In this case, Ga^+ is used to bombard the target so that the change of refractive index of the substrate glass is inevitable. Moreover, such an index change is not uniform across all the zones of the phase FZP. This is because each zone is exposed to different ion dose due to different zone width during FIB etching process. In addition, ion induced damage extent in the scanned surface is different along the

beam direction and orthogonal to it [150]. As a result, index variations over the phase FZP can change the phase retardation of the individual zone of the FZP leading to an inefficient diffraction. Another issue arising from the use of FIB is that the milled trenches deviates from the designed vertical sidewalls as discussed in Section 5.3.2. Hence phase retardation introduced by etch depth is not in congruence with the design value and thus causing deviation from the predicted focusing performance.

Another source of errors may be associated with the NSOM measurement. The coupling of the electric field through the probe may change the value of the true field and thus introduce errors in the measurement. In the previous studies, it was reported that the coupling of in-plane ($|E_x|^2$) field components to the NSOM probe is more efficient than that of the out-of-plane components ($|E_z|^2$) [151, 152]. Thus, NSOM probes may not exhibit equal sensitivity to all field components, the total intensity measured may deviate from the actual intensity value.

5.4 Summary

A binary phase FZP has been designed and fabricated on a glass substrate by using FIB for the first time to achieve a near-field focusing in the visible spectrum [134]. From the NSOM measurement, it is found that near-field focusing of a linearly polarized light to an asymmetric spot with subwavelength beamwidth can be achieved by the phase FZP. The rotational asymmetry of a focal spot is due to the high NA of the phase FZP. In addition, the phase FZP has demonstrated an elongated depth of focus (~ 250 nm) which may be used to realize auto-focusing feature in the optical systems. Although there are some deviations between the measurement and calculation values of the side lobes, the experimental results are in qualitative agreement with that obtained from the FDTD simulation.

Chapter 6

Design and Analysis of Two-Dimensional High-Index-Contrast Grating (HCG) Surface-Emitting Lasers

This chapter focuses on a novel subwavelength grating with high-index-contrast used as high reflective mirrors. A polarization independent 2-dimensional grating is designed and analyzed. Further, feasibility of such gratings in realization of surface emitting laser cavity is demonstrated theoretically.

6.1 High-Index-Contrast Grating (HCG)

6.1.1 Distributed Bragg Reflectors (DBR)

To get a coherent, monochromatic light of a laser beam requires a pair of mirrors at opposite ends of a photon-generating active medium. Photons of a specific frequency undergo multiple reflections between the mirrors, piling up energy with each pass as shown in Figure 6.1(a). At saturation level, the light energy is transferred into a laser beam. Early versions semiconductor lasers used easy-to-fabricate cleaved crystal facets as the reflective mirrors at either end of the cavity. However, such cleaved crystal yields reflectivity about 30%. For example, GaN has the refractive index of about 2.5 at λ = 400 nm, which leads to a reflectivity of only 18% even for a perfectly smooth facet. Such a low reflectivity is inefficient for low-power consumption

applications. To compensate for low mirror efficiency, a larger internal gain is required and the cavity is less frequency-selective.

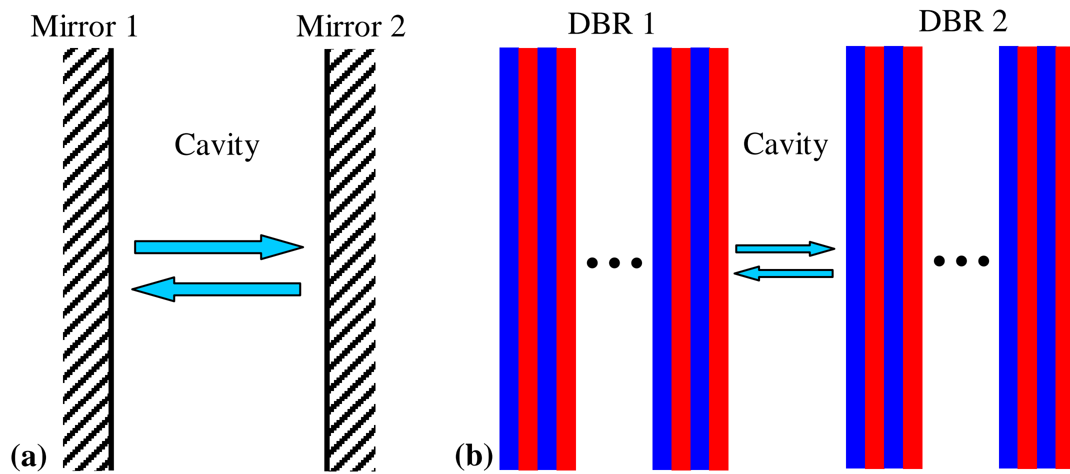

Figure 6.1 (a) Concept of laser cavity with mirrors at opposite ends. (b) Distributed Bragg reflector (DBR) pairs as a replacement of conventional crystal facet mirrors.

High reflectivity can be attained with the use of distributed Bragg reflectors (DBR). The DBR utilizes a diffraction grating built into the structure in the vicinity of the active region to provide strong wavelength selectivity [153]. For surface emitting lasers, DBR is formed via growth of alternating dielectric layers to take advantage of standing wave patterns formed in such structures (see Figure 6.1(b)). The refractive index contrast allows a small amount of light to be reflected from each pair of alternating layers. A strongly reflected coherent beam results from gradual built up of the light from multiple pairs.

However, DBRs are limited by their low refractive index contrast due to epitaxial growth constraints. Thus, to attain high reflectivity, large numbers of DBR pairs with alternating refractive indices are needed. For example, a 11.5 pairs ZnO/Al_2O_3 (index contrast of ~ 0.33 at λ = 385 nm) (see Figure 6.2(a-b)) and 60 pairs of $Al_{0.2}Ga_{0.8}N/GaN$ DBR (index contrast of ~ 0.08 at λ = 378 nm) are required to

attain a peak reflectivity above 99% [154]. Thus, reflectors based on DBR may have dimensions in many micrometers and hence are difficult to integrate with modern compact optical devices. The fabrication of highly reflective DBRs is difficult due to the epitaxial growth constraints of semiconductor dielectric layers with low-index-contrast. Other disadvantage of DBR is due to their narrow bandwidth of reflection, usually of order of tens of nanometers. In an alternative approach, an air-gap DBR structure consisting of alternating layers of air and semiconductor material is proposed in horizontal [155] and vertical configurations [156]. Out of these configurations, vertical configuration is more challenging from the fabrication point of view. Due to higher refractive index contrast, higher reflectivity is reported even with 3 air/semiconductor pairs (see Figure 6.2(c-d)). Higher etch depth requirements often results in non-vertical side walls due fabrication process constraints. The reflectivity is strongly affected by the tilt of the sidewall. It can be seen from Figure 6.2(d) even 5° tilt is side-wall results in a reduction of reflective to 50-60%. Such structures may serve following advantages over epitaxial DBR structure [156]: Higher reflectivity per period due to the high index of refraction difference between air and semiconductor, a wider stop band and a lower effective cavity length enabling a lower threshold current and a single mode operation. However, air/semiconductor DBR configuration is more suited for edge emitting lasers due to horizontal nature of the structure.

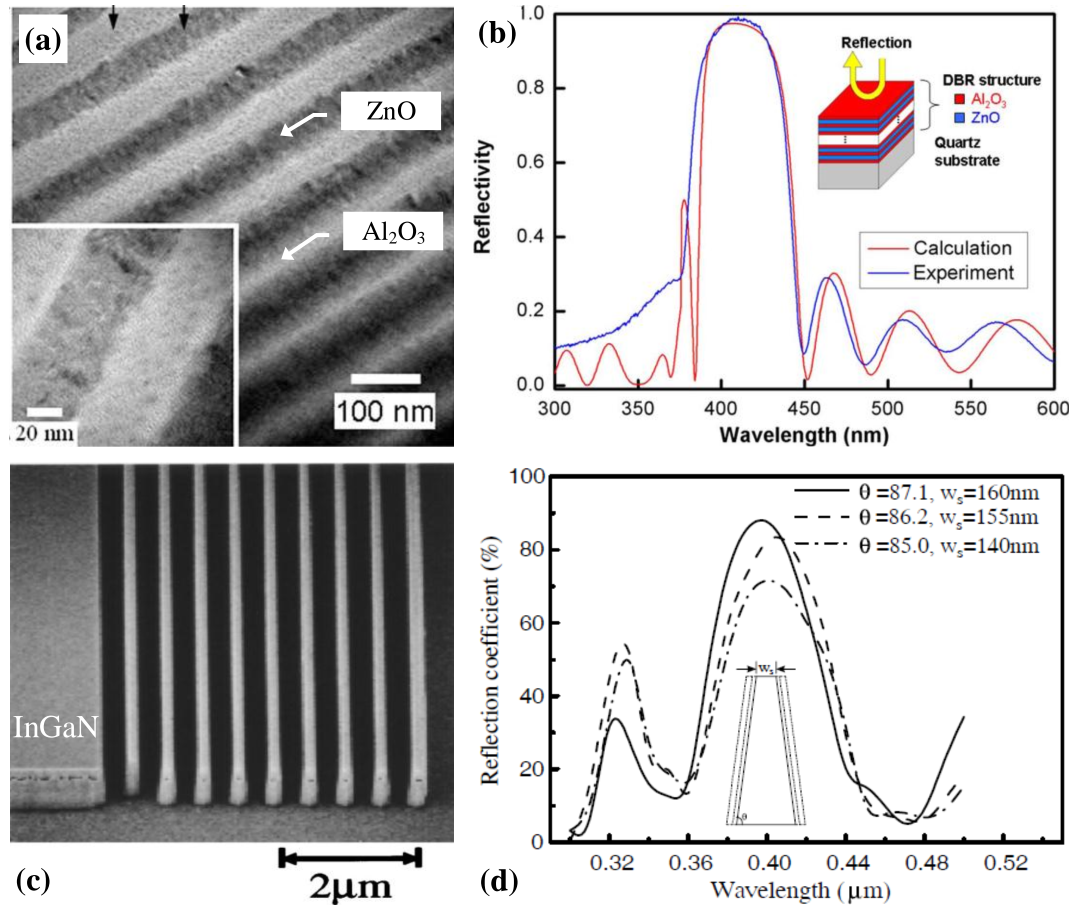

Figure 6.2 (a) Multilayer DBR configuration with Al_2O_3/ZnO thin films and (b) reflection spectra with 11.5 pairs of Al_2O_3/ZnO [155]. (c) Air/semiconductor DBR configuration with InGaN and (d) theoretical reflection spectra with 3 pairs of air/InGaN [157, 158].

6.1.2 HCG Mirrors

6.1.2.1 HCG Concept and Properties

Recently, extensive studies have been concentrated on the use of one-dimensional (1D) high-index-contrast subwavelength gratings (HCGs) as the broadband reflectors [159, 160]. HCG construction is simple as shown in Figure 6.3(a) which consists of a single-layer 1D-grating (i.e., periodic stripes with high-index-contrast) sandwiched in-between two low-index cladding layers. The HCGs can provide a high reflectivity (i.e., > 99%) over a broadband region (i.e., > 15% of the operating wavelength).

Matues et al [159, 160] have demonstrated high reflection (> 99%) over a broadband region more than 30% with the use of HCG made in poly-silicon (high index material, 3.48) on silica (low index material, 1.47) (see Figure 6.3(b)).

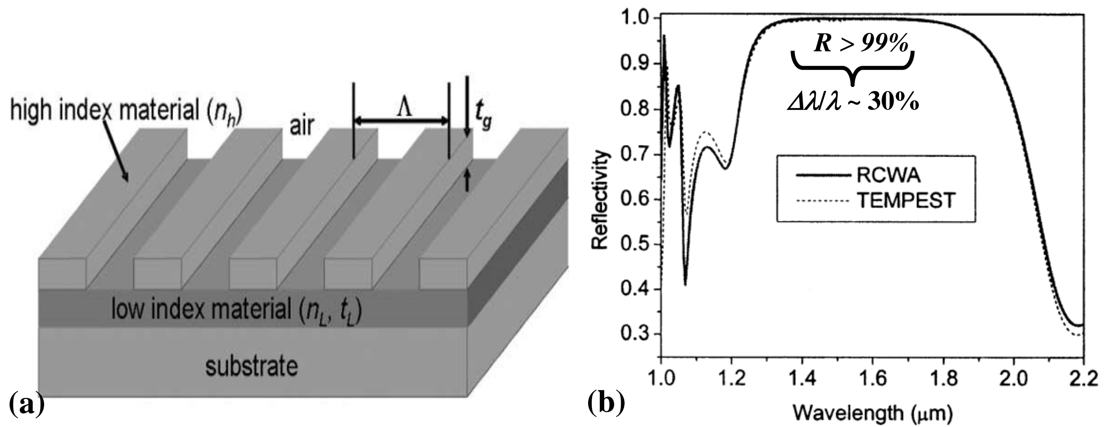

Figure 6.3 (a) Concept of a high-index-contrast (HCG) grating (b) reflectivity by HCG showing broadband reflection ($\Delta\lambda/\lambda$ ~ 30%) [159].

High reflectivity of 1D-HCGs can be explained by the mechanism of guided-mode resonance (GMR). The periodic modulation of refractive index generates counter-propagating leaky modes inside the grating structure. Under phase matching conditions, these counter-propagating leaky modes establish standing waves and give rise to GMR. [161-163]. As a result, the leaky modes re-radiate reflectively through the resonant interaction with the grating. It is noted that the high reflective zone of the 1D HCGs is arisen from the blend of the adjacent leaky modes [164]. Hence, if the number and spectral location of the leaky modes is controlled, it is possible to introduce a dip to the high reflective zone (i.e., a cavity mode of the HCGs).

HCG parameters can be tuned in order to act as a narrow-band mirror. Such property is useful in attaining a high-Q resonator. For example, for HCG with $Al_{0.6}Ga_{0.4}As$ with n = 3.0789 at λ = 1.55 μm, as shown in Figure 6.4, the reflectivity spectrum has a sharp asymmetric line shape under TE-polarized illumination at normal

incidence angle [165]. The reflectivity pattern is similar to the typical Fano resonance. The Q-factor of the HCG reflector is calculated as high as > 500 000.

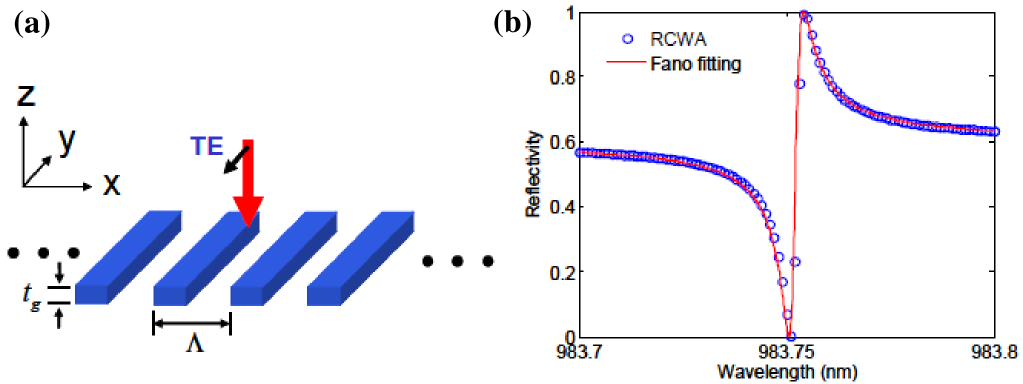

Figure 6.4 (a) HCG structure under TE polarized illumination. (b) Simulated reflectivity spectrum of HCG grating and corresponding fitted Fano resonance line shape. Q factor is ~500,000 [165].

6.1.2.2 HCG Applications

The use of HCG was proposed to replace the top DBR mirror of vertical-cavity surface-emitting lasers (VCSELs) [166-168]. The design and fabrication of VCSELs can be further simplified if the use of DBRs can be completely avoided. As shown in Figure 6.5(a), top DBR of VCSEL has been replaced by HCG and air-gap is electrostatically tuned to shift the output wavelength of the device. Air-gap can be replaced with thick oxide gap (see Figure 6.5(b)) as proposed by Chung et al [169]. This would simplify the fabrication process, as sacrificial etching needed to create an air-gap is complex than oxidation process. In addition, the device will have a better mechanical stability.

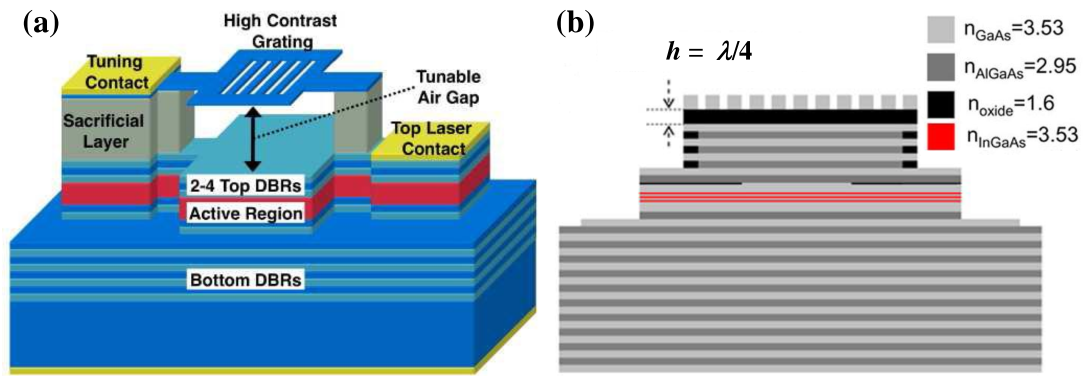

Figure 6.5 Application of 1-dimensional high-index-contrast grating (HCG) in VCSEL (a) suspended HCG as a top mirror with tunable air-gap [168] (b) HCG with thick ($h = \lambda/4$) oxide gap [169].

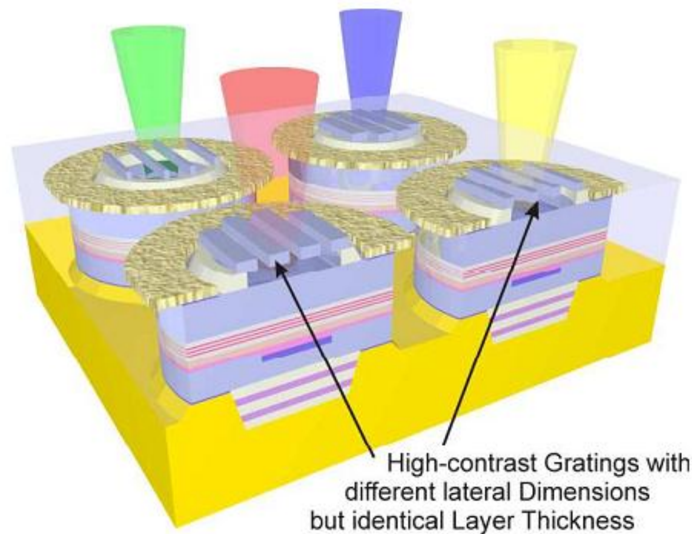

Figure 6.6 Schematic of multi-wavelength HCG-VCSEL array design [170].

Monolithically-integrated, low cost, high-speed, multi-wavelength (MW) sources are important in various high bandwidth applications. MW VCSEL may be cost effective due to their surface normal emission characteristic and compatibility with wafer scale manufacturing and testing. DBR/VCSEL based MW source arrays are fabricated utilizing layer thickness variations involves complicated processes and not readily scalable to large arrays. Karagodsky et al [170] proposed a MW-VCSEL by using HCG as top mirror. As shown in Figure 6.6, each source has a top HCG

mirror with different lateral dimensions. Lasing wavelength can be tuned over a large wavelength range by moderate changes in lateral HCG parameters (grating period and duty cycle). Wavelength tuning via lateral dimensions of HCG, which solely depends on lithography process, makes the device easy to fabricate as vertical dimensions (layer thickness) are kept constant.

HCG grating is reported to exhibit a large fabrication tolerance. Zhou et al [171] has demonstrated about ±30% fabrication tolerance while maintaining high (>99.5%) reflectivity. For VCSEL application, the HCG structure was shown to tolerate grating spacing variation from 80 to 120 nm (~ ±30%) and 40 nm change (~ ±10%) in grating period. As shown in Figure 6.7, white dots represents grating spacing and periods of different fabricated HCG-VCSEL devices successfully lased. Such a high tolerance to design parameters makes it possible to opt for low-cost and high-throughput fabrication process for HCG based devices on large volume basis.

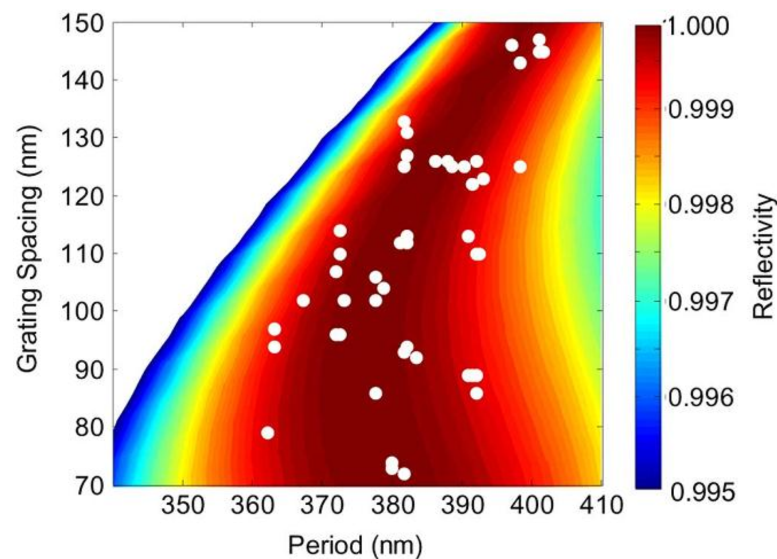

Figure 6.7 HCG grating reflectivity when used as a top mirror of VCSEL (λ = 840 nm). The white dots represents fabricated HCG-VCSEL parameters that led to lasing [171].

All applications discussed so far uses HCG under normal illumination mode. High reflectivity of HCG under glancing incidence angle has been exploited by Zhou et al [172] in order to realize hollow-core waveguides. Hollow-core waveguides exhibit ultra-low loss, nonlinearity and dispersion due to the absence of the core material. A hollow-core photonic crystal optical fiber is reported to have loss of ~ 0.001 dB/m [173] however loss in chip-based DBR hollow-core waveguide is still high (loss ~ 10 dB/m) [174]. Figure 6.8(a) shows schematic of HCG based waveguide wherein two high reflective HCGs are used with periods along propagation direction. It was reported that such waveguides show loss of 0.01 db/m with reasonable tolerance to the variations in HCG dimensions (Figure 6.8 (b)). As seen from Figure 6.8(c), the electric field outside the waveguide is negligible compared to the field at the hollow core.

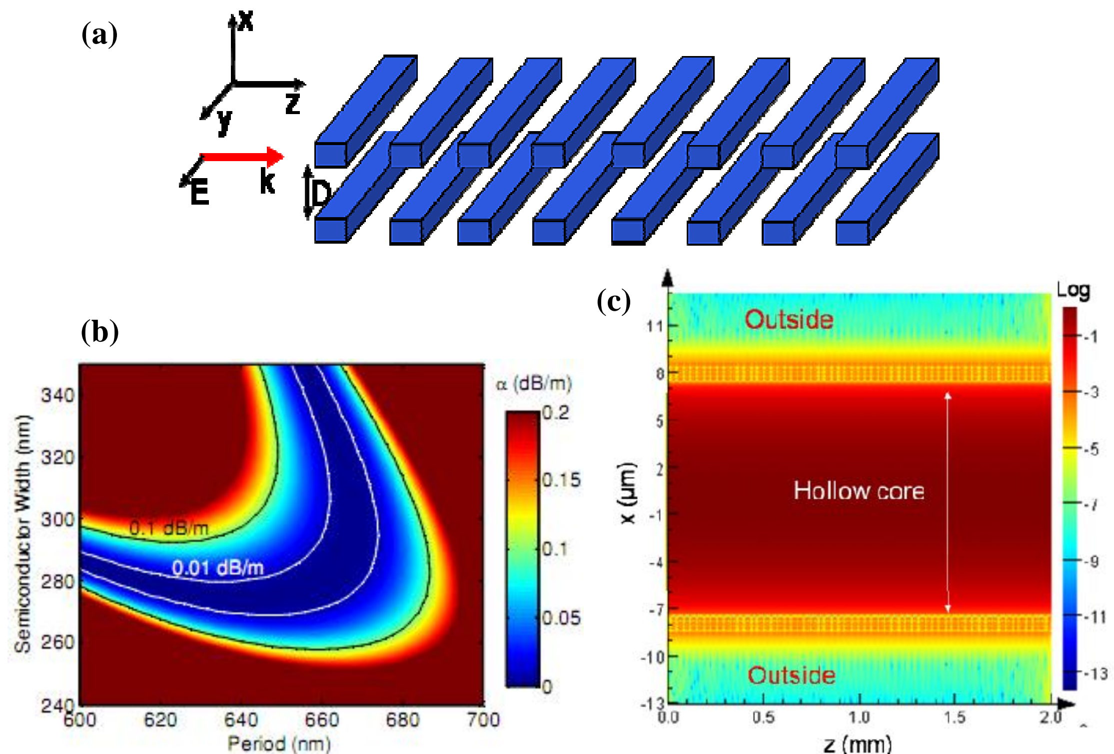

Figure 6.8 (a) Hollow-core slab waveguide with high reflective 1D HCG (b) Waveguide loss as function of grating period and semiconductor width (c) Electric field intensity profile of hollow-core HCG waveguide [172].

6.2 Design and Analysis

The case of a two-dimensional (2D) HCG is investigated, in which a single-layer grating is constructed by a 2D high-index-contrast of square periodic lattice [175]. Figure 6.9 shows the schematic of a proposed 2D HCG considered in our studies. It is assumed that the square periodic lattice is constructed by a layer of high-index periodic lattice with refractive index of n_H. The square periodic lattice is supported by a layer of low-index buffer layer, which has refractive index and thickness of n_L and t_{buf} respectively, laid on a substrate. The top surface of the square periodic lattice is surrounded by air. In order to understand how laser cavity can be formed within the 2D HCGs, the corresponding reflection and transmission characteristics are analyzed and compared with that of the 1D HCGs. It is assumed that the structure of 1D HCGs is identical to that of the 2D HCGs except that the 2D grating (i.e., square periodic lattice) is replaced by infinite long periodic stripes with the same period.

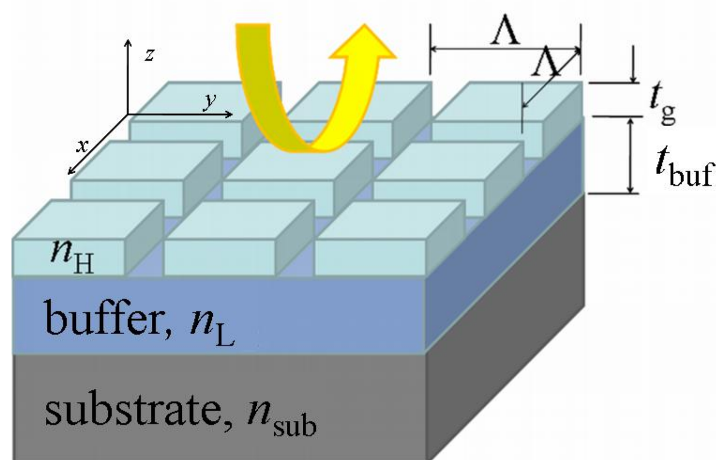

Figure 6.9 Schematic of a 2D HCG. Thickness of grating layer, t_g, was set to 460 nm. The refractive indices of grating layer, buffer layers and substrate were set to n_H = 3.48, n_L = 1.45 and n_{sub} = 3.48 respectively.

Figure 6.10 shows the reflection and transmission spectra of the 1D and 2D HCGs. The period, Λ, and height, t_g, of the 1D- and 2D-gratings were set to 700 and 460 nm respectively and the corresponding thickness of buffer layer, t_{buf}, was set to infinite in the calculation. In addition, Poly-silicon (n_H = 3.48) and SiO_2 (n_L = 1.45) were assumed to be high-index layer and buffer layer respectively with negligible absorption loss. A 3-D finite-difference time-domain (FDTD) method was used to investigate the reflection and transmission characteristics of the HCGs. Mesh was set at 7×7×7 nm^3. In addition, periodic boundary condition was used in the FDTD calculation to approximate the periodicity of the 1D- and 2D- gratings.

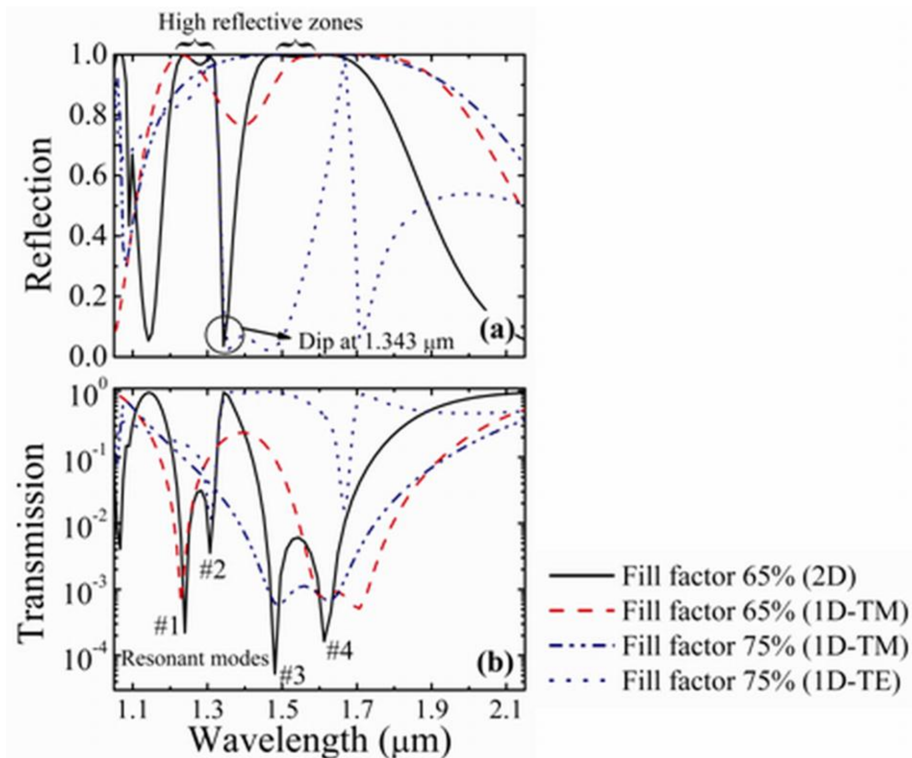

Figure 6.10 Plot of (a) reflection and (b) transmission spectra of 1D and 2D HCGs. The HCGs have same period (Λ = 700 nm) and thickness of gratings (t_g = 460 nm) and were supported by an infinite thick buffer layer (i.e., $t_{buf} = \infty$).

1D HCG with fill factor of 75% shows broadband reflection for the illumination of TM polarized light. Two closely spaced leaky modes (at 1.49 and 1.63

μm) can be seen from the transmission spectrum. These modes interact with the waveguide grating leading to efficient reflection [176]. Each mode corresponds to a high reflective mode (i.e., transmittance approaching zero) due to GMR. For the illumination of TE polarized light, the reflection spectrum is a narrow band. This is evident from the corresponding transmission spectrum, which shows wide spacing of the weak leaky modes. For 1D HCG with a fill factor of 65%, one extra isolated leaky mode appears at a shorter wavelength (1.229 μm). As a result, the wide spectral spacing of the leaky modes contributes to a shallow and wide dip in the reflection spectrum. On the other hand, for the case of 2D HCG with a fill factor of 65%, four leaky modes appeared in the transmission spectrum. It is noted that the leaky modes #1 (1.239 μm), #2 (1.306 μm) and #3 (1.48 μm), #4 (1.612 μm) contribute to the high reflective regions centered at ~1.3 and ~1.6 μm respectively. Mode #2 is an extra leaky mode appearing in the transmission spectra of the 2D HCG when compared to that of the 1D HCG with the same fill factor. Furthermore, the presence of a mode #2 leads to a significant drop of the reflectivity at ~1.343 μm (i.e., the reflection dip). In other words, the presence of multiple modes, which cause the separation of GMR location, is due to 2D nature of the grating. As a result, a dip in the reflection spectrum is obtained. This dip of the reflectivity represents the formation of a resonant cavity mode of the 2D HCG [175].

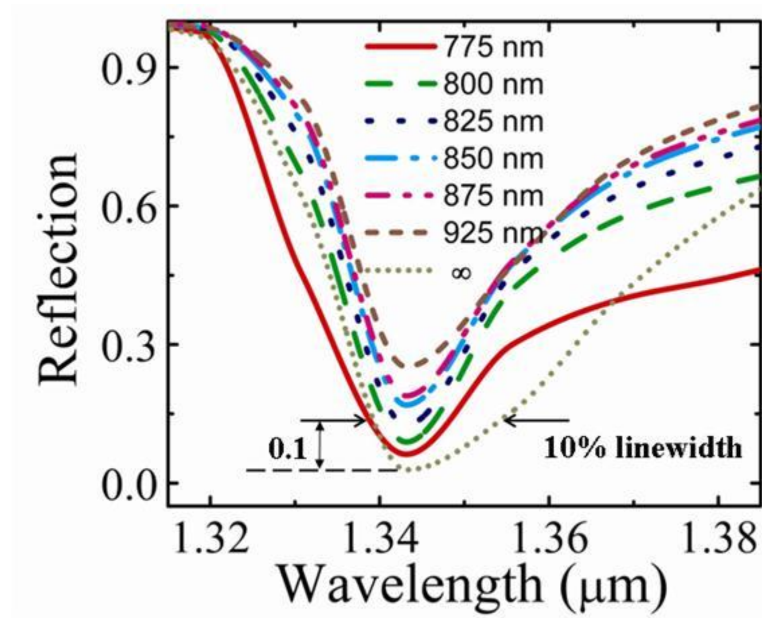

Figure 6.11 Reflection spectra of 2D HCGs with varying thickness of buffer layer (i.e., t_{buf} varies between 775 and 925 nm).

In order to verify that the formation of cavity mode is due to the 2D nature of the grating instead of Fabry-Perot resonance, the value of t_{buf} is allowed to vary between 775 and 925 nm (see Figure 6.11). It is observed that when t_{buf} increases from 775 to 925 nm, the reflectivity at the dip wavelength of ~1.343 μm increases from 7% to ~ 25%. However, the minimum value of the reflection dip (~3%) occurs only when $t_{buf} = \infty$. This suggests that the dip in the reflection spectrum is due to the 2D nature of the grating and the cavity mode is not formed inside the buffer layer. However, the buffer layer has influence on the fineness of the reflection dip.

It can be shown that there is a proportional relationship between the wavelength of the reflection dip and the dimensions of the grating. For a 1D HCG, the resonant conditions of resonant leaky modes can be determined by eigen-equations [177]:

$$\left.\begin{aligned} \tan(\kappa_i t_g) &= \frac{\kappa_i\left(\gamma_i+\delta_i\right)}{\left(\kappa_i^2-\gamma_i\delta_i\right)} && \text{(TE mode)} \\ \tan(\kappa_i t_g) &= \frac{n_g^2\kappa_i\left(n_L^2\gamma_i+\delta_i\right)}{n_L^2\kappa_i^2-n_g^4\gamma_i\delta_i} && \text{(TM mode)} \end{aligned}\right\} \quad (6.1)$$

where i is an integral denoting the diffraction order of grating, βi $(= k[n_g\sin\theta - i\lambda/\Lambda])$ is effective propagation constant of the waveguide grating, k $(= 2\pi/\lambda)$ is the wavevector in free space, θ is the incidence angle to the normal of the grating, λ is the resonant wavelength, and n_g is the effective reflective index of the grating layer. The parameters $\kappa_i(=\sqrt{n_g^2k^2-\beta_i^2})$, $\gamma_i(=\sqrt{\beta_i^2-k^2})$, and $\delta_i(=\sqrt{\beta_i^2-n_L^2k^2})$ are defined as the wave vectors within the grating layer, air and buffer layer respectively. If the resonant wavelength λ increases to $Y\lambda$ by a factor of Y, it can also be shown that the values of β_i, κ_i, γ_i and δ_i can be reduced to β_i/Y, κ_i/Y, γ_i/Y and δ_i/Y respectively if $\theta = 0$ and Λ increases by a factor of Y. In order to satisfy Equation (6.1) for this new resonant wavelength, t_g has to be increased to Yt_g. Hence, there is a proportional relationship between resonant wavelength and the dimensions of the grating. For our 2D HCGs with the dimensions of grating identical in both x and y directions (see Figure 6.9), the corresponding eigen-equations and phase matching conditions are similar to that of the 1D grating. Therefore, the proportional relationship should also be held for the 2D HCGs. In order to demonstrate this scalable property of the 2D HCGs numerically, a design with a reflection dip located at a wavelength of 1.343 μm was used for the calculation. The corresponding values of, Λ, fill factor, t_g and t_{buf}, were set to 700 nm, 65%, 460 nm and 825 nm respectively. Reflection dip at wavelength of 1.55 and 2 μm can be achieved by scaling up Λ, t_g and t_{buf}, altogether by a factor 1.157 and 1.489 respectively as shown in Figure 6.12. It can be seen that the wavelength of reflection dips and reflection patterns are similar for all the three cases under investigation.

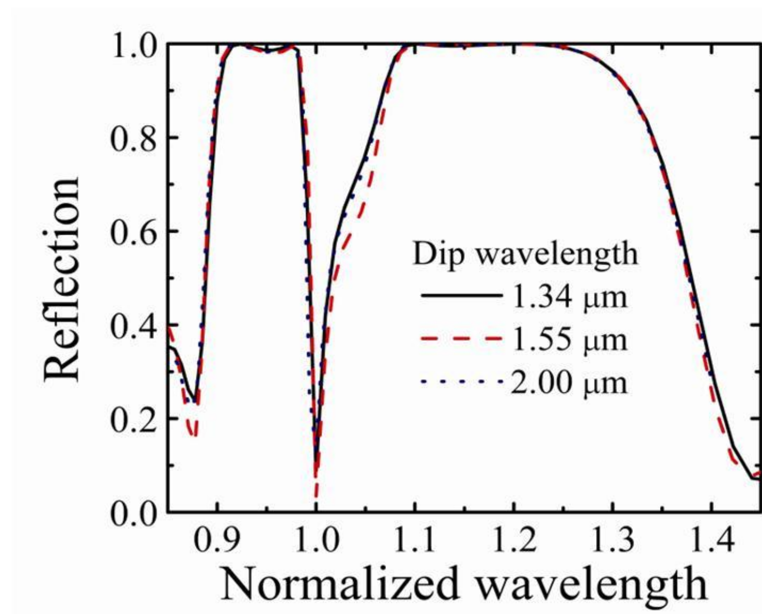

Figure 6.12 Plot of the reflection spectra of the HCGs versus normalized wavelength (i.e., normalized to the wavelength of the reflection dip). For the reflection dip at 1.343 μm, the dimensions of 2D HCG were set to Λ = 700 nm, fill factor = 65%, t_g = 460 nm and t_{buf} = 825 nm. For a reflection dip at 1.55 and 2 μm, the corresponding dimensions of 2D HCG were scaled by a factor of 1.157 and 1.489 respectively

6.3 Influence of Design Parameters on the Performance of 2D HCG

Figure 6.13 plots the reflection spectra of the 2D-HCGs with Λ, as the variable. It is observed that two high reflective zones are only emerging at Λ ~700 nm with a dip located at wavelength of ~1.342 μm. The dependence of reflection spectra on the fill factor of the 2D-HCGs is also shown in Figure 6.13(b). It is noted that two broad reflective zones can be obtained with fill factor ~65% and the corresponding location of the dip is at wavelength of ~1.342 μm. However, other values of fill factor will not allow the formation of a narrow dip in between the two broad reflection zones. Figure 6.13(c) shows the variation of reflection spectra with t_g. It is observed that the two broad reflection zones can be obtained for a wider range of t_g (i.e., between 450 and 460 nm) with the wavelength of the dip located at ~1.342 μm. From the above

calculation, it is shown that the formation of resonant cavity mode is strongly dependent on the values of Λ and fill factor. This may be the reason why resonant characteristics of the 2D HCGs have not been discovered. From the above calculation, it is noted that a narrow dip at ~1.342 μm can be obtained from the 2D-HCG with Λ ~700 nm and fill factor ~65%. In addition, the reflectivity of the surrounding reflective zones can be larger than 99%. Figure 6.13(d) plots the reflectivity of the 2D HCGs with optimized values of Λ (= 700 nm), fill factor (= 65%) and t_g (=450 nm) versus the polarization angle of the normal incident wave. It is observed that the symmetric configuration of the 2D-HCG causes its reflectivity insensitive to the angle of incident polarization. This indicated that the formation of resonant cavity mode is mainly due to the 2D nature of the symmetric grating.

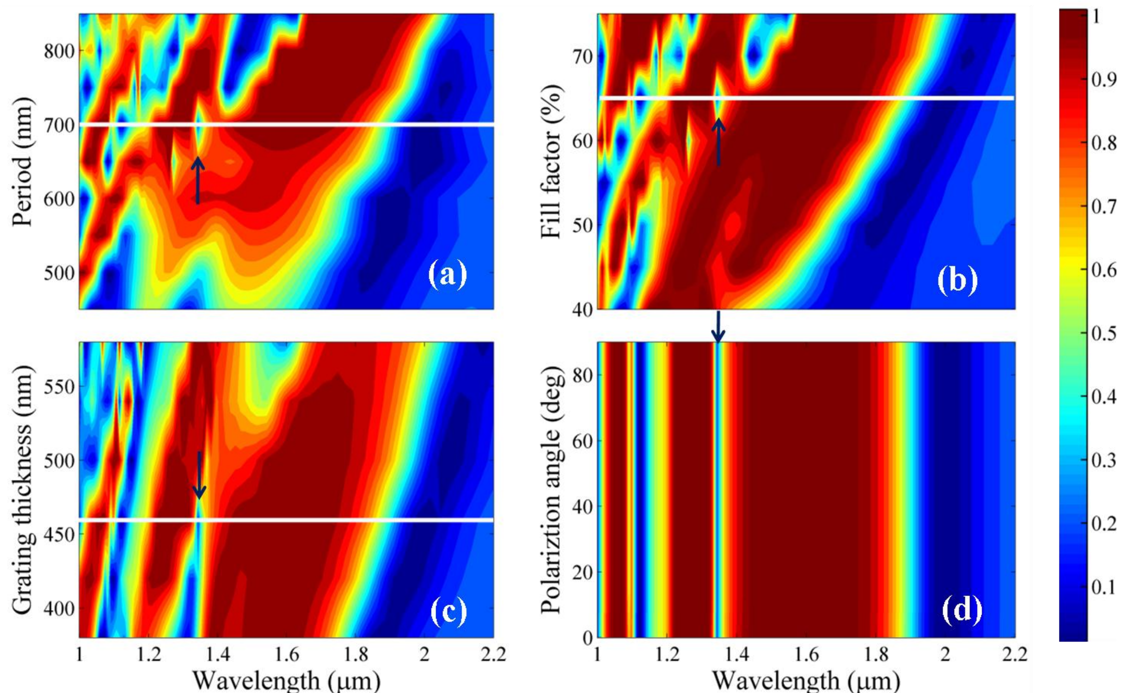

Figure 6.13 Influence of (a) period of grating (Λ) (b) fill factor (c) grating thickness (t_g) and (d) polarization angle on the reflectivity of 2D HCG.

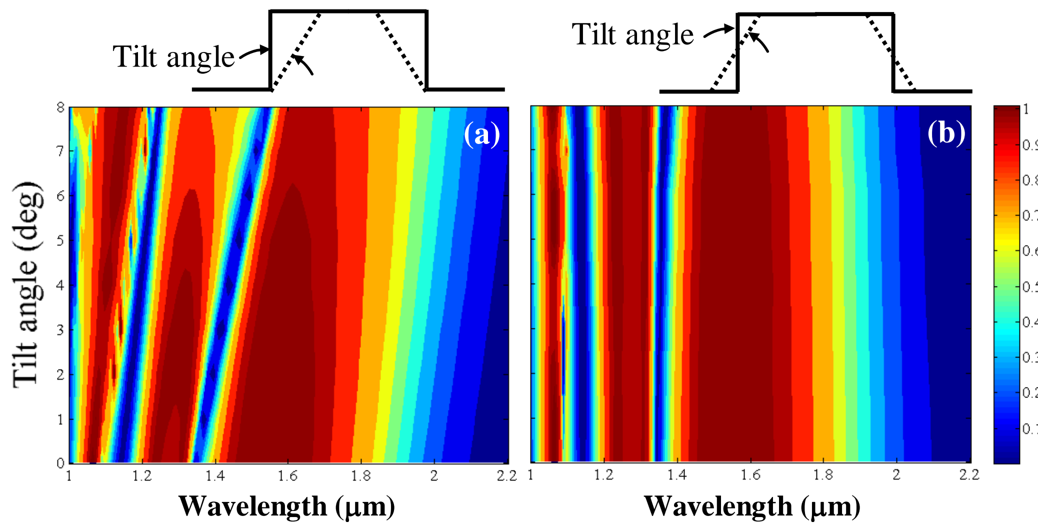

Figure 6.14 Influence of sidewall tilt angle on reflection characteristics: (a) the bottom width of the grating remains constant (b) the middle width of the grating remains constant. 0 deg implies vertical side walls. HCG parameters are: $\Lambda = 700$ nm, fill factor = 65%, $t_g = 460$ nm.

Figure 6.14 shows the influence of a sidewall tilt angle on the reflection characteristics of the grating. From fabrication point of view, producing exact vertical wall is difficult hence; the device performance with non-vertical sidewalls is a crucial concern. We consider two modes by which tilted sidewalls may occur: First, the bottom width of the grating remains constant (same as designed width) and corresponding reflectivity is shown in Figure 6.14(a), and second, the middle width of the grating remains constant (same as designed width) and corresponding reflectivity is as shown in Figure 6.14(b). It is observed that keeping middle width constant makes the device more tolerant to tilt angles when compared with the other configuration. With increase in tilt angle, dip wavelength is shifted towards longer wavelength. However, the shift is more with loss in reflectivity in case of constant bottom width configuration. This is because an effective index of the grating remains almost same if middle width does not allowed to be altered. However, in the other case, device will get an extra air space and the effective index will be reduced. The effect will be similar

to that of increasing fill factor (see Figure 6.13(b)). Reflectivity loss is observed with increase in the air space due to diffractive spreading loss [178].

6.4 Surface Emitting Laser with 2D HCG

Conventional 1D 2nd order grating structure using low-index contrast has been used to fabricate surface emitting lasers [179]. The proposed 2D grating can also be applied to realize surface-emitting lasers by inserting a thin active layer between the grating and buffer layers. However, the 2D grating structure, which need not to be a 2nd order grating, is necessary to have high-index-contrast. This is because high-index-contrast between the grating and buffer layers is essential to achieve high reflective zones and a sharp reflection dip. Reduced index contrast below 2 (i.e., $n_H/n_L < 2$) may lead to loss in reflectivity and poor Q factor of the device. Hence, refractive index and peak gain wavelength of the active layer should be close to the buffer layer and wavelength of the reflection dip respectively. If the buffer layer was assumed to be made by SiO_2, which has a refractive index of 1.45 at a wavelength of 1.343 μm, Nd:YAG can be used as an active layer. Hence, the refractive index, n_{act}, and the peak gain wavelength of the active layer can be set to be 1.82 and 1.343 μm respectively [180] in the calculation. In addition, the thickness of the active layer, t_{act}, was assumed to be 100 nm. In our analysis, a Lorentz model [181] was used to implement the gain material into FDTD algorithm. In this case, the corresponding permittivity, ε, can be expressed as

$$\varepsilon(\omega) = \varepsilon_o + \frac{\varepsilon_{Lor}\omega_o^2}{\omega_o^2 - 2i\omega\delta_{Lor} - \omega^2} \tag{6.2}$$

where ε_o = 3.3124, ω_0 = 1.4×10^3 THz (~1.343 μm), and δ_{Lor} = 31.4 THz (~ 50 nm). The emission spectra observed from the surface of the 2D HCGs can be calculated by a Fourier transform of the electric fields.

Two configurations of the 2D-HCG laser, i.e., with 1) t_{buf} = 725 nm and 2) t_{buf} = ∞, are considered in the studies. Figure 6.15 plots the emission spectra of the 2D-HCG laser at threshold. Sharp resonance is observed at ~1.34 μm for the case t_{buf} = ∞. However, the resonance wavelength shifted to ~1.342 μm for the case t_{buf} = 725 nm. This is because the effective refractive index of the buffer layer is slightly increased due to the influence of substrate (which is assumed to have refractive index larger than the buffer layer) so that the resonant frequency of the standing wave inside the 2D grating is slightly shifted. For the case of t_{buf} = ∞, Q factor is found to be ~925. This large value of Q is expected from the reflection spectrum of the 2D HCG with t_{buf} = ∞ as the corresponding reflectivity is the lowest at the dip wavelength (see Figure 6.11). On the other hand, although the presence of buffer layer will increase the reflectivity of the reflection dip, the reduction of 10% linewidth of the reflection dip (see Figure 6.11) can compensate for the increase of reflectivity so that the value of Q factor can be improved. The inset of Figure 6.15 shows the Q factor of the 2D HCGs with different values of t_{buf}. The corresponding reflectivity and 10% linewidth of the reflection dip are also plotted in the figure. It is observed that the magnitude of reflection increases with t_{buf} but the linewidth of the reflection dip reaches a minimum for t_{buf} between 725 and 775 nm. As a result, a maximum value of Q factor equal to 1032 can be obtained at t_{buf} = 725 nm. However, the Q factor does not improve for the value of t_{buf} other than 725 nm.

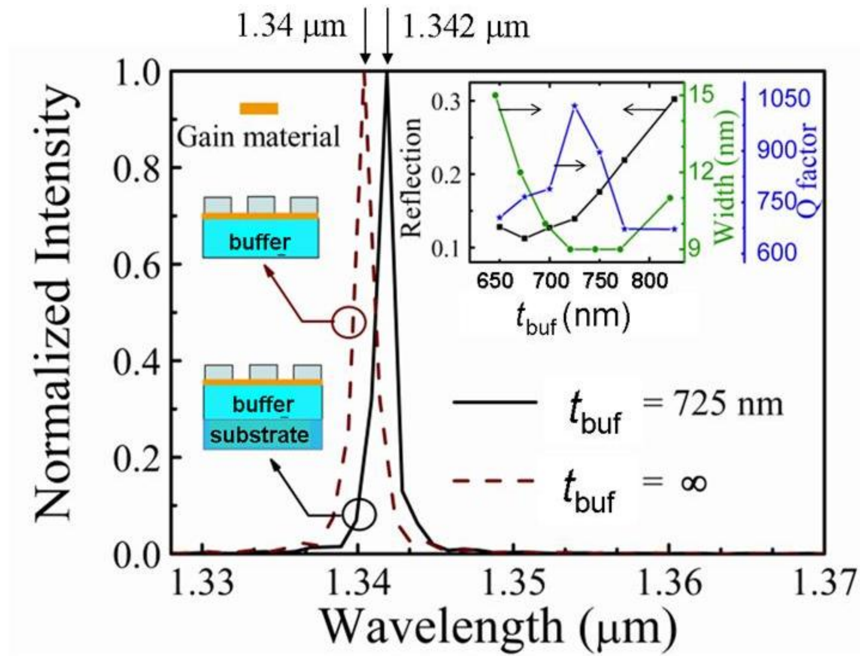

Figure 6.15 Surface emission spectra of 2D HCG lasers with t_{buf} of 725 nm and infinite thick. The inset shows the reflectivity and 10% linewidth (defined as the width of the dip spectrum at a level 10% above the reflection dip, see Figure 6.9) of the reflection dip, as well as the Q factor of the 2D HCGs versus t_{buf}.

6.5 Summary

In summary, the reflection characteristics of 2D HCGs were investigated. In contrast to 1D HCGs, symmetric nature of 2D HCG makes it insensitive to the incident polarization. With suitable selection of Λ, fill factor and t_{buf} of the 2D HCGs, cavity resonant (i.e., a dip of the reflectivity) can be observed from the corresponding reflection spectrum [175]. The excitation of cavity mode (i.e., the dip) in 2D HCGs can be explained by the excitation of extra resonant leaky mode (#2 mode in Figure 6.10(b)) causing the formation of two high reflective zones in the reflection spectrum. It is noted that there is a very narrow range of Λ, fill factor and t_g to generate the cavity mode. By inserting a thin active layer between the grating and buffer layers, a 2D HCG surface-emitting laser with Q factor as high as 1032 can be realized and the value of Q factor is dependent on thickness of the buffer layer [175].

Chapter 7

Conclusions and Future Work

"*I almost wish I hadn't gone down the rabbit-hole - and yet - it's rather curious, you know, this sort of life*!" said Alice.

This chapter summarizes the conclusions of this thesis and suggests related areas for further research.

7.1 Conclusions

1) We have carried out a study of amplitude and phase type Fresnel zone plates (FZP) with ultra-short focal lengths ($\sim\lambda$) under visible wavelength (λ = 633 nm). The FZP design was based on classical optical theory and implications of using such design in the near-field focusing were studied. Following are main conclusions [95]:

   - FZPs for near-field focusing exhibits unique characteristics of focal shift, elongated depth of field (DoF) and the suppression of higher order foci. The shift of focal length and elongation of DoF can be optimized by controlling the number of zones and the choice of film thickness of the FZPs. Suppression of higher order foci improves diffraction efficiency, as diffracted energy is concentrated in the first order focus only. However, it is necessary for the focal length of the FZPs to be less than ~10 times the operating wavelength.

- This work shows a unique behavior, which is more appropriately explained by the diffraction of evanescent, fields inside the subwavelength feature of the transparent zones in FZPs.
- Phase FZP can be obtained by realizing the required zones through etching on the glass substrate so that no opaque coating is required. It is found that the phase zone plates can support high-intensity focal spot with subwavelength size. The peak transmission intensity is found to be 5 times higher than those from *Ag*-coated FZPs.

2) With high numerical-aperture (NA) focusing elements, vector nature of illumination i.e. polarization plays a critical role in defining the focal spot profile [111].

- A simple analytical model for high NA phase FZP is presented based on Richard and Wolf's vector diffraction theory. The formalism shows agreement with the exact solution obtained by FDTD method. The deviations from exact solution are due to influence of evanescent waves present in the near-field and are not accounted in the model.
- High NA phase FZP under the illumination of linearly polarized light produces rotationally asymmetric focal spot. Furthermore, the value of transverse components can be reduced to certain extent by introducing phase modulation with the reduction of the etch depth.
- The illumination of a radially polarized light can produce a rotationally symmetric focal spot. As a result, a focal spot with beamwidth of 250 nm (0.39λ) is shown to be possible with phase FZP.

3) Both amplitude and phase FZPs have been fabricated by using FIB technology. NSOM measurements are carried out to study the focusing behavior [134].

- With sample current monitoring through the end point monitor (EPM) feature of FIB, amplitude type FZP fabrication is demonstrated on metal-coated glass substrate.
- Phase FZPs are fabricated on glass substrate with ITO coating. Tilt in sidewalls is observed due to Gaussian distribution of ion beam and redeposition of milled material. Impact of tilt of sidewalls on the focusing performance is evaluated and it is found that sidewall tilt angle upto 30° can change the focusing intensity by just 10% provided the designed zone widths are maintained at the center of the zone depth. Further, the tilt angle is reduced by using lower beam current and dwell time values.
- From the NSOM measurement, with a phase FZP of 500 nm focal length (λ = 633 nm) it is shown that near-field focusing of a linearly polarized light to an asymmetric spot with a subwavelength beam-width is possible. The focusing characteristics are in agreement with the FDTD results. Deviations are attributed to FIB induced damage in the material and NSOM probe coupling issues.

4) The properties of 2D subwavelength high-index-contrast grating (HCG) are investigated and their application in realizing surface-emitting laser is demonstrated [175].

- 2D HCG reflection spectrum consists of a transmission dip surrounded by high reflective zones. The reason behind the dip is decoupling of guided mode resonance with the introduction of 2nd dimension.
- There exists a very narrow range of grating period, fill factor and grating thickness to generate cavity modes.

- By inserting a thin active layer between the grating and buffer layers, a 2D HCG surface-emitting laser with Q factor as high as 1032 can be realized. The value of Q factor is dependent on thickness of the buffer layer.
- In contrast to 1D HCGs, symmetric nature of 2D HCG makes it insensitive to the incident polarization. Such property may also be well suited for applications in amplifiers and optical filters.

7.2 Future Work

Related areas for further research can include the following:

1) A rigorous diffraction theory for subwavelength FZPs for near-field focusing may be developed in order to predict accurate focusing behavior.
2) Under linear polarization, rotationally asymmetric focusing is observed from high NA FZP. A further optimization of FZP design may be carried out with an objective to improve rotational symmetry of focusing. This is because, although radial polarization yields a perfect rotational symmetric focusing, the linear polarization is still popular due to easy optics.
3) FIB fabrication induced damage to FZP structure and its impact on focusing characteristics can be studied in detail by identifying the extent of damage to geometry and optical properties of the material. Comparative evaluation with other fabrication processes may be followed.
4) NSOM probe is known to be sensitive to certain field components. In addition, the material of the probe may cause change in near-field parameters. A further theoretical and experimental study can be carried out with different probes in order to throw more light on coupling phenomenon and related issues with NSOM measurements.

5) In this work, focusing by FZP in free air space is investigated. However, in application like optical data storage/lithography, interfaces among various media with different optical properties are encountered. The effect on such interfaces can be studied theoretically and experimentally.

References

[1] G. E. Moore, "Cramming more components onto integrated circuits," *Electron. Mag.* **38(8)**, 114-117 (1965).

[2] M. Ohtsu, "Near-field optical microscopy and application to nanophotonics," in *Optical Imaging and Microscopy*. vol. 87, P. Török and F.-J. Kao, Eds., 2nd ed Berlin / Heidelberg: Springer, 2007.

[3] B. D. F. Casse, W. T. Lu, Y. J. Huang, and S. Sridhar, "Nano-optical microlens with ultrashort focal length using negative refraction," *Appl. Phys. Lett.* **93(5)**, 053111 (2008).

[4] E. Abbe, "Beiträge zur theorie des mikroskops und der mikroskopischen wahrnehmung," *Arch. Microsc. Anat.* **9(1)**, 413-418 (1873).

[5] L. Rayleigh, "On the theory of optical images with special reference to the microscope," *Philos. Mag.* **5(42)**, 167-195 (1896).

[6] S. M. Mansfield and G. S. Kino, "Solid immersion microscope," *Appl. Phys. Lett.* **57(24)**, 2615-2616 (1990).

[7] T. Yano, S. Shibata, and T. Kishi, "Fabrication of micrometer-size glass solid immersion lens," *Appl. Phys. B* **83(2)**, 167-170 (2006).

[8] D. Marks and P. S. Carney, "Near-field diffractive elements," *Opt. Lett.* **30(14)**, 1870-1872 (2005).

[9] S. Sinzinger and J. Jahns, *Microoptics*, 2nd ed. Weinheim: WILEY-VCH GmbH & Co. KgaA, (2003).

[10] D. A. Fletcher, K. E. Goodson, and G. S. Kino, "Focusing in microlenses close to a wavelength in diameter," *Opt. Lett.* **26(7)**, 399-401 (2001).

[11] R. Merlin, "Radiationless electromagnetic interference: Evanescent-field lenses and perfect focusing," *Science* **317(5840)**, 927-929 (2007).

[12] J. Y. Lee, B. H. Hong, W. Y. Kim, S. K. Min, Y. Kim, M. V. Jouravlev, R. Bose, K. S. Kim, I. C. Hwang, L. J. Kaufman, C. W. Wong, and P. Kim, "Near-field focusing and magnification through self-assembled nanoscale spherical lenses," *Nature* **460(7254)**, 498-501 (2009).

[13] M. W. Farn, "Binary gratings with increased efficiency," *Appl. Opt.* **31(22)**, 4453-4458 (1992).

[14] P. Lalanne, S. Astilean, P. Chavel, E. Cambril, and H. Launois, "Blazed binary subwavelength gratings with efficiencies larger than those of conventional echelette gratings," *Opt. Lett.* **23(14)**, 1081-1083 (1998).

[15] J. Kirz, "Phase zone plates for X-rays and the extreme UV," *J. Opt. Soc. Am.* **64(3)**, 301-309 (1974).

[16] S. Rehbein, R. B. Doak, R. E. Grisenti, G. Schmahl, J. P. Toennies, and C. Woll, "Nanostructuring of zone plates for helium atom beam focusing," *Microelectron. Eng.* **53(1)**, 685-688 (2000).

[17] W. Chao, B. D. Harteneck, J. A. Liddle, E. H. Anderson, and D. T. Attwood, "Soft X-ray microscopy at a spatial resolution better than 15 nm," *Nature* **435(7046)**, 1210-1213 (2005).

[18] R. Menon, A. Patel, D. Gil, and H. I. Smith, "Maskless lithography," *Mat. Today* **8(2)**, 26-33 (2005).

[19] D. Gil, R. Menon, T. Xudong, H. I. Smith, and D. J. D. Carter, "Parallel maskless optical lithography for prototyping, low-volume production, and research," *J. Vac. Sci. Technol. B* **20(6)**, 2597-601 (2002).

[20] L. Feng, K. A. Tetz, B. Slutsky, V. Lomakin, and Y. Fainman, "Fourier plasmonics: Diffractive focusing of in-plane surface plasmon polariton waves," *Appl. Phys. Lett.* **91(8)**, 081101-3 (2007).

[21] Y. Fu, W. Zhou, L. E. N. Lim, C. L. Du, and X. G. Luo, "Plasmonic microzone plate: Superfocusing at visible regime," *Appl. Phys. Lett.* **91(6)**, 061124 (2007).

[22] L. Novotny and B. Hecht, *Principles of Nano-Optics*. Cambridge: Cambridge University Press, (2006).

[23] U. C. Fischer and H. P. Zingsheim, "Submicroscopic pattern replication with visible light," *J. Vac. Sci. Technol.* **19(4)**, 881-885 (1981).

[24] J. B. Pendry, "Negative Refraction Makes a Perfect Lens," *Phys. Rev. Lett.* **85(18)**, 3966-3969 (2000).

[25] R. A. Shelby, D. R. Smith, and S. Schultz, "Experimental Verification of a Negative Index of Refraction," *Science* **292(5514)**, 77-79 (2001).

[26] R. H. Ritchie, "Plasma losses by fast electrons in thin films," *Phys. Rev.* **106(5)**, 874-881 (1957).

[27] T. W. Ebbesen, H. J. Lezec, H. F. Ghaemi, T. Thio, and P. A. Wolff, "Extraordinary optical transmission through sub-wavelength hole arrays," *Nature* **391(6668)**, 667-669 (1998).

[28] X. Y. Lu, Y. Huang, Z. M. Tang, Q. Y. Hong, Z. Y. Lu, Y. P. Zhong, W. H. Ye, and L. Y. Liu, "Use of surface plasmon resonance (SPR) sensor for real time in situ study of adsorption of proteins onto surface of polyurethane," *Chin. J. Biomed. Eng.* **22(2)**, 164-70 (2003).

[29] P. Ginzburg, D. Arbel, and M. Orenstein, "Gap plasmon polariton structure for very efficient microscale-to-nanoscale interfacing," *Opt. Lett.* **31(22)**, 3288-3290 (2006).

[30] H. J. Lezec, A. Degiron, E. Devaux, R. A. Linke, L. Martin-Moreno, F. J. Garcia-Vidal, and T. W. Ebbesen, "Beaming light from a subwavelength aperture," *Science* **297(5582)**, 820-822 (2002).

[31] L. Martin-Moreno, F. J. Garcia-Vidal, H. J. Lezec, A. Degiron, and T. W. Ebbesen, "Theory of highly directional emission from a single subwavelength aperture surrounded by surface corrugations," *Phys. Rev. Lett.* **90(16)**, 167401 (2003).

[32] W. L. Barnes, A. Dereux, and T. W. Ebbesen, "Surface plasmon subwavelength optics," *Nature* **424(6950)**, 824-830 (2003).

[33] Z. Liu, J. M. Steele, W. Srituravanich, Y. Pikus, C. Sun, and X. Zhang, "Focusing surface plasmons with a plasmonic lens," *Nano Lett.* **5(9)**, 1726-1729 (2005).

[34] Z. Liu, J. M. Steele, H. Lee, and X. Zhang, "Tuning the focus of a plasmonic lens by the incident angle," *Appl. Phys. Lett.* **88(17)**, 171108 (2006).

[35] W. Nomura, M. Ohtsu, and T. Yatsui, "Nanodot coupler with a surface plasmon polariton condenser for optical far/near-field conversion," *Appl. Phys. Lett.* **86(18)**, 181108 (2005).

[36] L. L. Yin, V. K. Vlasko-Vlasov, J. Pearson, J. M. Hiller, J. Hua, U. Welp, D. E. Brown, and C. W. Kimball, "Subwavelength focusing and guiding of surface plasmons," *Nano. Lett.* **5(7)**, 1399-1402 (2005).

[37] Z. Sun and H. K. Kim, "Refractive transmission of light and beam shaping with metallic nano-optic lenses," *Appl. Phys. Lett.* **85(4)**, 642-644 (2004).

[38] C. Min, P. Wang, X. Jiao, Y. Deng, and H. Ming, "Beam focusing by metallic nano-slit array containing nonlinear material," *Appl. Phys. B* **90(1)**, 97-99 (2008).

[39] H. Shi, C. Wang, C. Du, X. Luo, X. Dong, and H. Gao, "Beam manipulating by metallic nano-slits with variant widths," *Opt. Express* **13(18)**, 6815-6820 (2005).

[40] Y. Fu, W. Zhou, L. E. N. Lim, C. Du, H. Shi, C. T. Wang, and X. Luo, "Transmission and reflection navigated optical probe with depth-tuned surface corrugations," *Appl. Phys. B* **86(1)**, 155-158 (2007).

[41] Y. Q. Fu, W. Zhou, L. E. N. Lim, C. Du, H. Shi, C. T. Wang, and X. Luo, "Influence of V-shaped plasmonic nanostructures on beam propagation," *Appl. Phys. B* **86(3)**, 461-466 (2007).

[42] Y. Fu, W. Zhou, L. E. N. Lim, C. Du, X. Luo, Z. Zhao, X. Dong, H. Shi, and C. Wang, "Geometrical characterization issues of plasmonic nanostructures with depth-tuned grooves for beam shaping," *Opt. Eng.* **45(10)**, 10800 (2006).

[43] H. Shi, C. Du, and X. Luo, "Focal length modulation based on a metallic slit surrounded with grooves in curved depths," *Appl. Phys. Lett.* **91(9)**, 093111-3 (2007).

[44] S. Kim, Y. Lim, H. Kim, J. Park, and B. Lee, "Optical beam focusing by a single subwavelength metal slit surrounded by chirped dielectric surface gratings," *Appl. Phys. Lett.* **92(1)**, 013103-3 (2008).

[45] J. Wang and W. Zhou, "Subwavelength beaming using depth-tuned annular nanostructures," *J. Mod. Opt.* **56(7)**, 919-926 (2009).

[46] J. Wang and W. Zhou, "An annular plasmonic lens under illumination of circularly polarized light," *Plasmonics* **4(3)**, 1557-1955 (2009).

[47] M. V. Berry and S. Popescu, "Evolution of quantum superoscillations and optical superresolution without evanescent waves," *J. Phys. A* **39(22)**, 6965-6977 (2006).

[48] F. M. Huang, N. Zheludev, Y. Chen, and F. J. G. de Abajo, "Focusing of light by a nanohole array," *Appl. Phys. Lett.* **90(9)**, 091119-3 (2007).

[49] F. M. Huang, Y. Chen, F. J. Garcia De Abajo, and N. I. Zheludev, "Optical super-resolution through super-oscillations," *J. Opt. A* **9(9)**, S285-S288 (2007).

[50] F. M. Huang, T. S. Kao, V. A. Fedotov, Y. Chen, and N. I. Zheludev, "Nanohole array as a lens," *Nano Lett.* **8(8)**, 2469-2472 (2008).

[51] X. Wang, J. Fu, X. Liu, and L. M. Tong, "Subwavelength focusing by a micro/nanofiber array," *J. Opt. Soc. Am. A* **26(8)**, 1827-1833 (2009).

[52] J. D. J. Stigliani, R. A. J. Mittra, and R. G. SemOnin, "Resolving power of a zone plate," *J. Opt. Soc. Am.* **57(5)**, 610-611 (1967).

[53] G. S. Waldman, "Variations on the Fresnel zone plate," *J. Opt. Soc. Am.* **56(2)**, 215-217 (1966).

[54] J.-A. Sun and A. Cai, "Archaic focusing properties of Fresnel zone plates," *J. Opt. Soc. Am. A* **8(1)**, 33-35 (1991).

[55] A. Dubra and J. A. Ferrari, "Diffracted field by an arbitrary aperture," *Am. J. Phys.* **67(1)**, 87-92 (1999).

[56] H. Osterberg and L. W. Smith, "Closed solutions of Rayleigh's diffraction integral for axial points," *J. Opt. Soc. Am.* **51(10)**, 1050-1054 (1961).

[57] A. S. Marathay and J. F. McCalmont, "On the usual approximation used in the Rayleigh-Sommerfeld diffraction theory," *J. Opt. Soc. Am. A* **21(4)**, 510-516 (2004).

[58] Y. Zhang and C. Zheng, "Axial intensity distribution behind a Fresnel zone plate," *Opt. Laser. Technol.* **37(1)**, 77-80 (2005).

[59] Y. V. Kopylov, A. V. Popov, and A. V. Vinogradov, "Application of the parabolic wave equation to X-ray diffraction optics," *Opt. Commun.* **118(5-6)**, 619-636 (1995).

[60] Y. V. Kopylov, A. V. Popov, and A. V. Vinogradov, "Diffraction phenomena inside thick Fresnel zone plates," in *1995 URSI International Symposium on Electromagnetic Theory, 23-26 May 1995*, USA, 1996, pp. 1815-22.

[61] G. Schneider, "Zone plates with high efficiency in high orders of diffraction described by dynamical theory," *Appl. Phys. Lett.* **71(16)**, 2242-2244 (1997).

[62] J. Maser and G. Schmahl, "Coupled wave description of the diffraction by zone plates with high aspect ratios," *Opt. Commun.* **89(2-4)**, 355-362 (1992).

[63] A. N. Kurokhtin and A. V. Popov, "Simulation of high-resolution x-ray zone plates," *J. Opt. Soc. Am. A* **19(2)**, 315-324 (2002).

[64] E. Noponen, J. Turunen, and A. Vasara, "Parametric optimization of multilevel diffractive optical elements by electromagnetic theory," *Appl. Opt.* **31**, 5910-5912 (1992).

[65] E. Noponen, J. Turunen, and A. Vasara, "Electromagnetic theory and design of diffractive-lens arrays," *J. Opt. Soc. Am. A* **10(3)**, 434-443 (1993).

[66] Y. Sheng, D. Feng, and S. Larochelle, "Analysis and synthesis of circular diffractive lens with local linear grating model and rigorous coupled-wave theory," *J. Opt. Soc. Am. A* **14**, 1562-1568 (1997).

[67] B. H. Kleemann and R. Guther, "Zonal diffraction efficiencies and imaging of micro-Fresnel lenses," *J. Mod. Opt.* **45(7)**, 1405-1420 (1998).

[68] H. Ichikawa, K. Masuda, and T. Ueda, "Analysis of micro-Fresnel lenses with local grating theory and its comparison with fully electromagnetic methods," *J. Opt. Soc. Am. A* **26(9)**, 1938-1944 (2009).

[69] D. W. Prather, M. S. Mirotznik, and J. N. Mait, "Boundary integral methods applied to the analysis of diffractive optical elements," *J. Opt. Soc. Am. A* **14(1)**, 34-43 (1997).

[70] J. N. Mait, D. W. Prather, and M. S. Mirotznik, "Binary subwavelength diffractive-lens design," *Opt. Lett.* **23(17)**, 1343-1345 (1998).

[71] J. N. Mait, D. W. Prather, and M. S. Mirotznik, "Design of binary subwavelength diffractive lenses by use of zeroth-order effective-medium theory," *J. Opt. Soc. Am. A* **16(5)**, 1157-1167 (1999).

[72] M. S. Mirotznik, D. W. Prather, J. N. Mait, W. A. Beck, S. Shi, and X. Gao, "Three-dimensional analysis of subwavelength diffractive optical elements with the finite-difference time-domain method," *Appl. Opt.* **39(17)**, 2871-2880 (2000).

[73] L. Kipp, M. Skibowski, R. L. Johnson, R. Berndt, R. Adelung, S. Harm, and R. Seemann, "Sharper images by focusing soft X-rays with photon sieves," *Nature* **414(6860)**, 184-188 (2001).

[74] Q. Cao and J. Jahns, "Focusing analysis of the pinhole photon sieve: individual far-field model," *J. Opt. Soc. Am. A* **19(12)**, 2387-2393 (2002).

[75] Q. Cao and J. Jahns, "Nonparaxial model for the focusing of high-numerical-aperture photon sieves," *J. Opt. Soc. Am. A* **20(6)**, 1005-1012 (2003).

[76] R. Menon, D. Gil, G. Barbastathis, and H. I. Smith, "Photon-sieve lithography," *J. Opt. Soc. Am. A* **22(2)**, 342-345 (2005).

[77] Y. Fu, C. Du, W. Zhou, and L. E. N. Lim, "Nanopinholes-based optical superlens," *Res. Lett. Phys.* **2008**, 148505 (2008).

[78] M. J. Simpson and A. G. Michette, "Imaging properties of modified Fresnel zone plates," *Opt. Acta* **31(4)**, 403-413 (1984).

[79] G. Saavedra, W. D. Furlan, and J. A. Monsoriu, "Fractal zone plates," *Opt. Lett.* **28(12)**, 971-973 (2003).

[80] Q. Cao and J. Jahns, "Comprehensive focusing analysis of various Fresnel zone plates," *J. Opt. Soc. Am. A* **21(4)**, 561-571 (2004).

[81] Q. Cao and J. r. Jahns, "Modified Fresnel zone plates that produce sharp Gaussian focal spots," *J. Opt. Soc. Am. A* **20(8)**, 1576-1581 (2003).

[82] W. D. Furlan, G. Saavedra, and J. A. Monsoriu, "Fractal zone plates produce axial Irradiance with fractal profile," *Opt. Photon. News* **14(12)**, 31 (2003).

[83] P. Srisungsitthisunti, O. K. Ersoy, and X. F. Xu, "Laser direct writing of volume modified Fresnel zone plates," *J. Opt. Soc. Am. B* **24(9)**, 2090-2096 (2007).

[84] P. Srisungsitthisunti, O. K. Ersoy, and X. F. Xu, "Volume Fresnel zone plates fabricated by femtosecond laser direct writing," *Appl. Phys. Lett.* **90(1)**, 011104 (2007).

[85] J. M. Finlan, K. M. Flood, and R. J. Bojko, "Efficient f/1 binary-optics microlenses in fused silica designed using vector diffraction theory," *Opt. Eng.* **34(12)**, 3560-3564 (1995).

[86] M. Schmitz and O. Bryngdahl, "Rigorous concept for the design of diffractive microlenses with high numerical apertures," *J. Opt. Soc. Am. A* **14(4)**, 901-906 (1997).

[87] M. Schmitz and O. Bryngdahl, "Rigorous analysis and design of diffractive cylindrical lenses with high numerical and large geometrical apertures," *Opt. Commun.* **153(1-3)**, 118-124 (1998).

[88] E. Hasman, V. Kleiner, G. Biener, and A. Niv, "Polarization dependent focusing lens by use of quantized Pancharatnam–Berry phase diffractive optics," *Appl. Phys. Lett.* **82(3)**, 328-330 (2002).

[89] Z. Bomzon, G. Biener, V. Kleiner, and E. Hasman, "Space-variant Pancharatnam-Berry phase optical elements with computer-generated subwavelength gratings," *Opt. Lett.* **27(13)**, 1141–1143 (2002).

[90] Di Feng, Y. Yan, G. Jin, and S. Fan, "Beam focusing characteristics of diffractive lenses with binary subwavelength structures," *Opt.Commun.* **239(4-6)**, 345–352 (2004).

[91] N. S. Di Feng, Lishuang Feng, Pan Ou and and C. Zhang, "Generation of an extended depth of focus using diffractive micro-lenses with binary structures in the non-paraxial domain," *J. Opt. A (Pure Appl. Opt.)* **11(6)**, 065704 (2009).

[92] D. Attwood, *Soft X-Rays and Extreme Ultraviolet Radiation: Principles and Applications.* Cambridge: Cambridge University Press, (2000).

[93] E. D. Palik, *Handbook of optical constants of solids II* Boston: Academic Press, (1991).

[94] H. Raether, *Surface plasmons on smooth and rough surfaces and on gratings*. Berlin: Springer-Verlag, (1988).

[95] R. G. Mote, S. F. Yu, B. K. Ng, W. Zhou, and S. P. Lau, "Near-field focusing properties of zone plates in visible regime - New insights," *Opt. Express* **16(13)**, 9554-9564 (2008).

[96] H. J. Lezec and T. Thio, "Diffracted evanescent wave model for enhanced and suppressed optical transmission through subwavelength hole arrays," *Opt. Express* **12(16)**, 3629-3651 (2004).

[97] Y. Li, "Predictions of Rayleigh's diffraction theory for the effect of focal shift in high-aperture systems," *J. Opt. Soc. Am. A* **25(7)**, 1835-1842 (2008).

[98] T. D. Beynon and R. M. R. Strange, "Computational study of diffraction patterns for near-field Fresnel and Gabor zone plates," *J. Opt. Soc. Am. A* **17(1)**, 101-106 (2000).

[99] R. Menon, "Zone Plate Array Lithography (ZPAL): Simulations and System Design," Master of Science, Electrical Engineering and Computer Science, Massachusetts Institute of Technology, (2000).

[100] H. F. Ghaemi, T. Thio, D. E. Grupp, T. W. Ebbesen, and H. J. Lezec, "Surface plasmons enhance optical transmission through subwavelength holes," *Phys. Rev.* **58(11)**, 6779-6782 (1998).

[101] T. Thio, K. M. Pellerin, R. A. Linke, H. J. Lezec, and T. W. Ebbesen, "Enhanced light transmission through a single subwavelength aperture," *Opt. Lett.* **26(24)**, 1972-1974 (2001).

[102] M. H. Horman, "Efficiences of zone plates and phase zone plates," *Appl. Opt.* **6(11)**, 2011-2013 (1967).

[103] A. R. Jones, "The focal properties of phase zone plates," *British J. Appl. Phys. D* **2(12)**, 1789-91 (1969).

[104] B. Lai, W. B. Yun, D. Legnini, Y. Xiao, J. Chrzas, P. J. Viccaro, V. White, S. Bajikar, D. Denton, F. Cerrina, E. Di Fabrizio, M. Gentili, L. Grella, and M. Baciocchi, "Hard X-ray phase zone plate fabricated by lithographic techniques," *Appl. Phys. Lett.* **61(16)**, 1877-9 (1992).

[105] B. Richards and E. Wolf, "Electromagnetic diffraction in optical systems. II. Structure of the image field in an aplanatic system," *Proc. Royal Soc. A* **253**, 358-379 (1959).

[106] R. Dorn, S. Quabis, and G. Leuchs, "The focus of light - Linear polarization breaks the rotational symmetry of the focal spot," *J. Mod. Opt.* **50(12)**, 1917-1926 (2003).

[107] H. F. Wang, L. P. Shi, B. Lukyanchuk, C. Sheppard, and C. T. Chong, "Creation of a needle of longitudinally polarized light in vacuum using binary optics," *Nat. Photon.* **2(8)**, 501-505 (2008).

[108] R. Dorn, S. Quabis, and G. Leuchs, "Sharper focus for a radially polarized light beam," *Phys. Rev. Lett.* **91(23)**, 2339011-2339014 (2003).

[109] J. Wang, W. Zhou, and A. K. Asundi, "Effect of polarization on symmetry of focal spot of a plasmonic lens," *Opt. Express* **17(10)**, 8137-8143 (2009).

[110] M. G. Moharam and T. K. Gaylord, "Three-dimensional vector coupled-wave analysis of planar-grating diffraction," *J. Opt. Soc. Am. A* **73(9)**, 1105-1112 (1983).

[111] R. G. Mote, S. F. Yu, W. Zhou, and X. F. Li, "Subwavelength focusing behavior of high numerical-aperture phase Fresnel zone plates under various polarization states," *Appl. Phys. Lett.* **95(19)**, 191113 (2009).

[112] R. Oron, J. L. Guedalia, N. Davidson, A. A. Friesem, and E. Hasman, "Anomaly in a high-numerical-aperture diffractive focusing lens," *Opt. Lett.* **25(7)**, 439-441 (2000).

[113] V. P. Kalosha and I. Golub, "Toward the subdiffraction focusing limit of optical superresolution," *Opt. Lett.* **32(24)**, 3540-3542 (2007).

[114] R. Menzel, *Photonics: Linear and Nonlinear Interactions of Laser Light and Matter*, 2nd ed. Berlin Heidelberg: Springer-Verlag, (2007).

[115] R. H. Jordan and D. G. Hall, "Free-space azimuthal paraxial wave equation: the azimuthal Bassel-Gauss beam solution," *Opt. Lett.* **19(7)**, 427-429 (1994).

[116] A. V. Nesterov and V. G. Niziev, "Laser beams with axially symmetric polarization [and application to laser cutting and inertial fusion]," *J. Phys. D* **33(15)**, 1817-22 (2000).

[117] K. Wan-Chin, P. No-Cheol, Y. Yong-Joong, C. Hyun, and P. Young-Pil, "Investigation of near-field imaging characteristics of radial polarization for application to optical data storage," *Opt. Rev.* **14(4)**, 236-42 (2007).

[118] Y. Shuangyang and Z. Qiwen, "Third-harmonic generation microscopy with tightly focused radial polarization," *J. Opt. A* **10(12)**, 125103 (2008).

[119] Z. Qiwen, "Trapping metallic Rayleigh particles with radial polarization," *Opt. Express* **12(15)**, 3377-3382 (2004).

[120] A. Yanai and U. Levy, "Plasmonic focusing with a coaxial structure illuminated by radially polarized light," *Opt. Express* **17(2)**, 924-932 (2009).

[121] F. I. Baida and A. Belkhir, "Superfocusing and light confinement by surface plasmon excitation through radially polarized beam," *Plasmonics* **4(1)**, 51-59 (2009).

[122] M. Meier, V. Romano, and T. Feurer, "Material processing with pulsed radially and azimuthally polarized laser radiation," *Appl. Phys. A* **86(3)**, 329-334 (2007).

[123] S. Quabis, R. Dorn, M. Eberler, O. Glockl, and G. Leuchs, "Focusing light to a tighter spot," *Opt. Commun.* **179(1-6)**, 1-7 (2000).

[124] Q. Zhan, "Cylindrical vector beams: from mathematical concepts to applications," *Adv. Opt. Phot.* **1(1)**, 1-57 (2009).

[125] K. S. Youngworth and T. G. Brown, "Inhomogenous polarization in scanning optical microscopy," in *Three-Dimensional and Multidimensional Microscopy: Image Acquisition Processing VII, 23-24 Jan. 2000*, USA, 2000, pp. 75-85.

[126] K. Youngworth and T. Brown, "Focusing of high numerical aperture cylindrical-vector beams," *Opt. Express* **7(2)**, 77-87 (2000).

[127] G. M. Lerman and U. Levy, "Effect of radial polarization and apodization on spot size under tight focusing conditions," *Opt. Express* **16(7)**, 4567-4581 (2008).

[128] W. Chen and Q. Zhan, "Numerical study of an apertureless near field scanning optical microscope probe under radial polarization illumination," *Opt. Express* **15(7)**, 4106-4111 (2007).

[129] L. R. Harriott, A. Wagner, and F. Fritz, "Integrated-circuit repair using focused ion-beam milling," *J. Vac. Sci. Technol. B* **4(1)**, 181-184 (1986).

[130] L. Frey, C. Lehrer, and H. Ryssel, "Nanoscale effects in focused ion beam processing," *Appl. Phys. A* **76(7)**, 1017-1023 (2003).

[131] H. W. Li, D. J. Kang, W. T. S. Huck, and M. G. Blamire, "Focused ion beam fabrication of silicon print masters," *Nanotechnol.* **14(2)**, 220-223 (2003).

[132] A. A. Tseng, I. A. Insua, J. S. Park, B. Li, and G. P. Vakanas, "Milling of submicron channels on gold layer using double charged arsenic ion beam," *J. Vac. Sci. Technol. B* **22(1)**, 82-89 (2004).

[133] Y. Q. Fu, W. Zhou, L. E. N. Lim, C. Du, H. Shi, C. T. Wang, and X. Luo, "A practical V-shaped nano-aperture flanked with surface corrugations for beam focusing," *J. Comp. Th. Nanosc.* **4(3)**, 614-618 (2007).

[134] R. G. Mote, S. F. Yu, A. Kumar, W. Zhou, and X. F. Li, "Experimental demonstration of near-field focusing of a phase micro-Fresnel zone plate (FZP) under linearly polarized illumination," *Appl. Phys. B* **102(1)**, 95-100 (2011).

[135] A. Lugstein, B. Basnar, J. Smoliner, and E. Bertagnolli, "FIB processing of silicon in the nanoscale regime," *Appl. Phys. A* **76(4)**, 545-548 (2003).

[136] E. H. Synge, "Method for extending microscopic resolution into the ultra-microscopic region," *Phil. Mag.* **6**, 356-362 (1928).

[137] E. A. Ash and G. Nicholls, "Super-resolution aperture scanning microscope," *Nature* **237(5357)**, 510-512 (1972).

[138] D. W. Pohl, W. Denk, and M. Lanz, "Optical stethoscopy: Image recording with resolution $\lambda/20$," *Appl. Phys. Lett.* **44(7)**, 651-653 (1984).

[139] A. Lewis, M. Isaacson, A. Harootunian, and A. Muray, "Development of a 500 Å spatial resolution light microscope: I. light is efficiently transmitted through λ/16 diameter apertures," *Ultramicroscopy* **13(3)**, 227-231 (1984).

[140] E. Betzig, J. K. Trautman, T. D. Harris, J. S. Weiner, and R. L. Kostelak, "Breaking the diffraction barrier: optical microscopy on a nanometric scale," *Science* **251(5000)**, 1468-1470 (1991).

[141] E. Betzig, P. L. Finn, and J. S. Weiner, "Combined shear force and near-field scanning optical microscopy," *Appl. Phys. Lett.* **60(20)**, 2484-2486 (1992).

[142] K. Karrai and R. D. Grober, "Piezoelectric tip-sample distance control for near field optical microscopes," *Appl. Phys. Lett.* **66(14)**, 1842-1844 (1995).

[143] S. Gautsch, *Using microtechnology to get to nanotechnology*, Updated: 2 Sept. 2004, Retrived:15 Mar. 2010 <http://machinedesign.com/article/using-microtechnology-to-get-to-nanotechnology-0902>

[144] F. Giorgis, *Scanning near-field optical microscopy (SNOM or NSOM) - Different methods of operation*, Updated: 21 Apr. 2005, Retrived:15 Mar. 2010 <http://www.azonano.com/details.asp?ArticleID=1205>

[145] H. Liu, Y. Yan, D. Yi, and G. Jin, "Design of three-dimensional superresolution filters and limits of axial optical superresolution," *Appl. Opt.* **42(8)**, 1463-1476 (2003).

[146] T. R. M. Sales and G. M. Morris, "Diffractive superresolution elements," *J. Opt. Soc. Am. A* **14(7)**, 1637-1646 (1997).

[147] B. Basnar, A. Lugstein, H. Wanzenboeck, H. Langfischer, E. Bertagnolli, and E. Gornik, "Focused ion beam induced surface amorphization and sputter processes," *J. Vac. Sc. Technol. B* **21(3)**, 927-930 (2003).

[148] I. Chyr, B. Lee, L. C. Chao, and A. J. Steckl, "Damage generation and removal in the Ga^+ focused ion beam micromachining of GaN for photonic applications," *J. Vac. Sc. Technol. B* **17(6)**, 3063-3067 (1999).

[149] Y. Fu and N. K. A. Bryan, "Investigation of physical properties of quartz after focused ion beam bombardment," *Appl. Phys. B* **B80(4-5)**, 581-585 (2005).

[150] W. Brezna, H. Wanzenbock, A. Lugstein, E. Bertagnolli, E. Gornik, and J. Smoliner, "Focussed ion beam induced damage in silicon studied by scanning capacitance microscopy," *Semicond. Sci. Technol.* **18**, 195–198.

[151] L. Zhaowei, J. M. Steele, W. Srituravanich, P. Yuri, S. Cheng, and Z. Xiang, "Focusing surface plasmons with a plasmonic lens," *Nano Lett.* **5(9)**, 1726-1729 (2005).

[152] G. M. Lerman, A. Yanai, and U. Levy, "Demonstration of nanofocusing by the use of plasmonic lens illuminated with radially polarized light," *Nano Lett.* **9(5)**, 2139-2143 (2009).

[153] S. Wang, "Principles of distributed feedback and distributed Bragg-reflector lasers," *IEEE J. Quantum Electron.* **QE-10(4)**, 413-427 (1974).

[154] K. E. Waldrip, J. Han, J. J. Figiel, H. Zhou, E. Makarona, and A. V. Nurmikko, "Stress engineering during metalorganic chemical vapor deposition of AlGaN/GaN distributed Bragg reflectors," *Appl. Phys. Lett.* **78(21)**, 3205-3207 (2001).

[155] S. H. Tsang, S. F. Yu, S. P. Lau, H. Y. Yang, and X. F. Li, "Suppression of random lasing modes in polycrystalline ZnO thin-film by using distributed Bragg reflector," *IEEE Photonics Technol. Lett.* **21(8)**, 549-551 (2009).

[156] R. Sharma, E. D. Haberer, C. Meier, E. L. Hu, and S. Nakamura, "Vertically oriented GaN-based air-gap distributed Bragg reflector structure fabricated using band-gap-selective photoelectrochemical etching," *Appl. Phys. Lett.* **87(5)**, 051107 (2005).

[157] H. Wang, M. Kumagai, T. Tawara, T. Nishida, T. Akasaka, N. Kobayashi, and T. Saitoh, "Fabrication of an InGaN multiple-quantum-well laser diode featuring high reflectivity semiconductor/air distributed Bragg reflectors," *Appl. Phys. Lett.* **81(25)**, 4703-4705 (2002).

[158] H. Wang, T. Tawara, M. Kumagai, T. Saitoh, and N. Kobayashi, "Novel design to fabricate high reflectivity GaN-based semiconductor/air distributed bragg reflector with the tilt of vertical sidewall," *Jap. J. Appl. Phys. 2* **41(6B)**, L682-L684 (2002).

[159] C. F. R. Mateus, M. C. Y. Huang, Y. Deng, A. R. Neureuther, and C. J. Chang-Hasnain, "Ultrabroadband mirror using low-index cladded subwavelength grating," *IEEE Photonics Technol. Lett.* **16(2)**, 518-520 (2004).

[160] A. E. Willner, "All mirrors are not created equal," *Nature Photon.* **1(2)**, 87-88 (2007).

[161] A. Hardy, D. F. Welch, and W. Streifer, "Analysis of second-order gratings," *IEEE J. Quantum Electron.* **25(10)**, 2096-105 (1989).

[162] Y. Ding and R. Magnusson, "Resonant leaky-mode spectral-band engineering and device applications," *Opt. Express* **12(23)**, 5661-5674 (2004).

[163] Y. Ding and R. Magnusson, "Band gaps and leaky-wave effects in resonant photonic-crystal waveguides," *Opt. Express* **15(2)**, 680-694 (2007).

[164] R. Magnusson and M. Shokooh-Saremi, "Physical basis for wideband resonant reflectors," *Opt. Express* **16(5)**, 3456-3462 (2008).

[165] Y. Zhou, M. Moewe, J. Kern, M. C. Huang, and C. J. Chang-Hasnain, "Surface-normal emission of a high-Q resonator using a subwavelength high-contrast grating," *Opt. Express* **3(12)**, 17282-17287 (2008).

[166] M. C. Y. Huang, Y. Zhou, and C. J. Chang-Hasnain, "A surface-emitting laser incorporating a high-index-contrast subwavelength grating," *Nature Photon.* **1(2)**, 119-122 (2007).

[167] M. C. Y. Huang, Y. Zhou, and C. J. Chang-Hasnain, "A nanoelectromechanical tunable laser," *Nature Photon.* **2**, 180 (2008).

[168] C. Chase, Y. Zhou, and C. J. Chang-Hasnain, "Size effect of high contrast gratings in VCSELs," *Opt. Express* **17(26)**, 24002-24007 (2009).

[169] C. Il-Sung, J. Mork, P. Gilet, and A. Chelnokov, "Subwavelength grating-mirror VCSEL with a thin oxide gap," *IEEE Photonics Technol. Lett.* **20(2)**, 105-107 (2008).

[170] V. Karagodsky, B. Pesala, C. Chase, W. Hofmann, F. Koyama, and C. J. Chang-Hasnain, "Monolithically integrated multi-wavelength VCSEL arrays using high-contrast gratings " *Opt. Express* **18(2)**, 694-699 (2010).

[171] Y. Zhou, M. C. Y. Huang, and C. J. Chang-Hasnain, "Large fabrication tolerance for VCSELs using high-contrast grating," *IEEE Photon. Technol. Lett.* **20(6)**, 434-436 (2008).

[172] Y. Zhou, V. Karagodsky, B. Pesala, F. G. Sedgwick, and C. J. Chang-Hasnain, "A novel ultra-low loss hollow-core waveguide using subwavelength high-contrast gratings," *Opt. Express* **17(3)**, 1508-1517 (2009).

[173] P. Roberts, F. Couny, H. Sabert, B. Mangan, D. Williams, L. Farr, M. Mason, A. Tomlinson, T. Birks, J. Knight, and P. St. J. Russell, "Ultimate low loss of hollow-core photonic crystal fibres," *Opt. Express* **13(1)**, 236-244 (2005).

[174] Y. Sakurai and F. Koyama, "Control of group delay and chromatic dispersion in tunable hollow waveguide with highly reflective mirrors," *Jpn. J. Appl. Phys.* **43**, 1091-1093 (2004).

[175] R. G. Mote, S. F. Yu, W. Zhou, and X. F. Li, "Design and analysis of two-dimensional high-index-contrast grating surface-emitting lasers," *Opt. Express* **17(1)**, 260-265 (2009).

[176] D. Rosenblatt, A. Sharon, and A. A. Friesem, "Resonant grating waveguide structures," *IEEE J. Quantum Electron.* **33(11)**, 2038-59 (1997).

[177] S. S. Wang and R. Magnusson, "Theory and applications of guided-mode resonance filters," *Appl. Opt.* **32**, 2606-2613 (1993).

[178] T. F. Krauss and R. M. De La Rue, "Optical characterization of waveguide based photonic microstructures," *Appl. Phys. Lett.* **68(12)**, 1613-1615 (1996).

[179] T. Kobayashi, Y. Kanamori, and K. Hane, "Surface laser emission from solid polymer dye in a guided mode resonant grating filter structure," *Appl. Phys. Lett.* **87(15)**, 151106 (2005).

[180] D. Sauder, A. Minassian, and M. J. Damzen, "Laser operation at 1.3 μm of 2at% doped crystalline Nd:YAG in a bounce geometry," *Opt. Express* **15(6)**, 3230-3235 (2007).

[181] A. Taflove and S. C. Hagness, *Computational Electrodynamics: the finite difference time-domain method*. Boston: Artech House, (2005).

Appendix A

Scalar Diffraction Integrals

The scalar diffraction theories are based on Kirchoff's boundary conditions stated as [1]:

1. The linear dimensions of the diffracting aperture are large compared with the wavelength.
2. The point of observation is sufficiently away (>> λ) to the plane of the aperture.

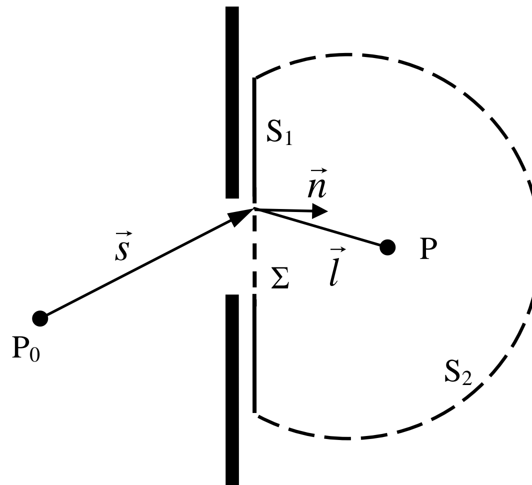

Figure A.1 Diffraction by an arbitrary aperture

Consider a plane opaque screen with an aperture Σ as shown in Figure A.1. Kirchoff's diffraction integral, which is obtained as a rigorous solution of the Helmholtz equation, can be written as:

$$U(P) = \frac{1}{4\pi}\iint_{\Sigma}\left[\frac{\partial U}{\partial n}G - U\frac{\partial G}{\partial n}\right]dS \tag{A.1}$$

In Kirchoff's formulation, the free-space Green's function is used [1]:

$$G_{Kirchoff} = \frac{\exp(ikl)}{l} \tag{A.2}$$

Using the above Green function, the famous integral theorem of Helmholtz and Kirchoff is obtained as:

$$U(P) = \frac{1}{4\pi}\iint_{\Sigma}\left[\frac{\partial U}{\partial n} - \left(ik - \frac{1}{l}\right)U\cos\left(\vec{n},\vec{l}\right)\right]dS \tag{A.3}$$

Now applying Kirchoff's boundary conditions:

$$U(P) = \frac{A}{2i\lambda}\iint_{\Sigma}\frac{e^{ik(l+s)}}{ls}\left[\cos\left(\vec{n},\vec{l}\right) - \cos\left(\vec{n},\vec{s}\right)\right]dS \tag{A.4}$$

Equation (A.4) is Fresnel-Kirchhoff diffraction formula.

Kirchhoff's theory is based on imposing boundary conditions on both the field (U) and its normal derivative ($\partial U/\partial n$). Further, Kirchhoff's theory has internal mathematical inconsistencies, as Kirchhoff's diffraction formula can not reproduce the boundary conditions used as the observation point approaches the aperture. A more consistent formulation is obtained by Rayleigh and Sommerfeld with the use of a Green's function given by [1]:

$$G_{R-S} = \frac{\exp(ikl)}{l} - \frac{\exp(ikl')}{l'} \tag{A.5}$$

Here l' is the mirror image of l on the opposite side of the screen. Using Equations (A.5) and (A.1) we obtain:

$$U(P) = \frac{-1}{2\pi} \iint_{\Sigma} U \frac{\exp(ikl)}{l} \left(ik - \frac{1}{l} \right) \cos\left(\vec{n}, \vec{l}\right) dS \tag{A.6}$$

This is a Rayleigh-Sommerfeld diffraction formula. This formulation is further simplified under the assumption of $z >> \lambda$ as:

$$U(P) = \frac{1}{i\lambda} \iint_{\Sigma} U \frac{\exp(ikl)}{l} \cos\left(\vec{n}, \vec{l}\right) dS \tag{A.7}$$

References

[1] J. W. Goodman, Introduction to Fourier optics, 3rd ed. Englewood, Colo.: Roberts & Co., (2005).

Appendix B

The Finite-Difference Time-Domain (FDTD) Method

The finite-difference time-domain (FDTD) method has recently become the start-of-the-art method for solving Maxwell's equations in complex geometries. Being a direct time and space solution, it offers the user a unique insight into all types of problems in electromagnetics and photonics. In addition, FDTD can also obtain the frequency solution as well by exploiting Fourier transforms, thus a full range of useful quantities can be calculated, such as the complex Poynting vector and the transmission/reflection of light. In the present work all FDTD calculations are performed by using a commercial FDTD solver *FDTD Solutions* by Lumerical Inc., Canada [1].

B.1 Maxwell's Equations and FDTD

Originally proposed by K.S. Yee [2], the FDTD method has emerged as a foremost numerical tool for the solution of the time-dependent Maxwell's equations in either differential or integral form. The FDTD method utilizes the central difference approximation to discretize the Maxwell's equations in both time and spatial domain, and then solves the resulting equations numerically to derive the electric and magnetic field distributions at each time step using an explicit leapfrog scheme.

Consider the general Maxwell's equations in time domain

$$\frac{\partial \mathbf{D}}{\partial t} = \nabla \times \mathbf{H} \tag{B.1}$$

$$\mathbf{D}(\omega) = \varepsilon_0 \cdot \varepsilon_r^* \cdot \mathbf{E}(\omega) \tag{B.2}$$

$$\frac{\partial \mathbf{H}}{\partial t} = -\frac{1}{\mu_0} \nabla \times \mathbf{E} \tag{B.3}$$

where,

E - Electric field intensity

H - Magnetic field intensity

D - Electric flux density

These equations can be normalized using

$$\tilde{\mathbf{E}} = \sqrt{\frac{\varepsilon_0}{\mu_0}} \cdot \mathbf{E} \tag{B.4}$$

$$\tilde{\mathbf{D}} = \frac{1}{\sqrt{\varepsilon_0 \cdot \mu_0}} \cdot \mathbf{D} \tag{B.5}$$

The normalized equations can be written as

$$\frac{\partial \tilde{\mathbf{D}}}{\partial t} = \frac{1}{\sqrt{\varepsilon_0 \cdot \mu_0}} \nabla \times \mathbf{H} \tag{B.6}$$

$$\tilde{\mathbf{D}}(\omega) = \varepsilon_r^* \cdot \mathbf{E}(\omega) \tag{B.7}$$

$$\frac{\partial \mathbf{H}}{\partial t} = -\frac{1}{\sqrt{\varepsilon_0 \cdot \mu_0}} \nabla \times \tilde{\mathbf{E}} \tag{B.8}$$

Equations (B.6) to (B.8) give six scalar equations for **D** and **H**. For example, equation for D_z is as:

$$\frac{\partial D_z}{\partial t} = \frac{1}{\sqrt{\varepsilon_0 \cdot \mu_0}} \left(\frac{\partial H_Y}{\partial x} - \frac{\partial H_x}{\partial y} \right) \tag{B.9}$$

The next step is to take finite difference approximations. To implement the scheme, Yee algorithm (see Figure B.1) is used. Yee has positioned the components of **E** and **H** about a unit cell of a lattice (Yee cell) as shown in a figure. It is observed that each **E** field component is surrounded by four **H** field components; similarly each **H** field component is surrounded by four **E** field components (If the field components on adjacent cubes are taken into account). The resulting equation for $\mathbf{D_z}$ is given by Equation (B.10).

$$\begin{aligned} &D_z^{n+1/2}(i,j,k+1/2) = \\ &D_z^{n-1/2}(i,j,k+1/2) + \frac{\Delta t}{\Delta x \cdot \sqrt{\varepsilon_0 \cdot \mu_0}} \begin{pmatrix} H_y^n(i+1/2,j,k+1/2) - H_y^n(i-1/2,j,k+1/2) \\ -H_x^n(i,j+1/2,k+1/2) + H_x^n(i,j-1/2,k+1/2) \end{pmatrix} \end{aligned} \tag{B.10}$$

By the same token, the update equations for the other field components can be derived. Since these equations compute the new field components from the field components at previous time-steps, they are frequently called update equations. In the equations the temporal location of the **E** and **H** field components differs by half time-step (*Δt/2*). In a typical simulation flow, one would determine the new **H** field components at *n+1/2* from the previous field components. Then the new **E** field components at *n+1* will be calculated. The process is then repeated as many times as required until the last time-step is reached [3].

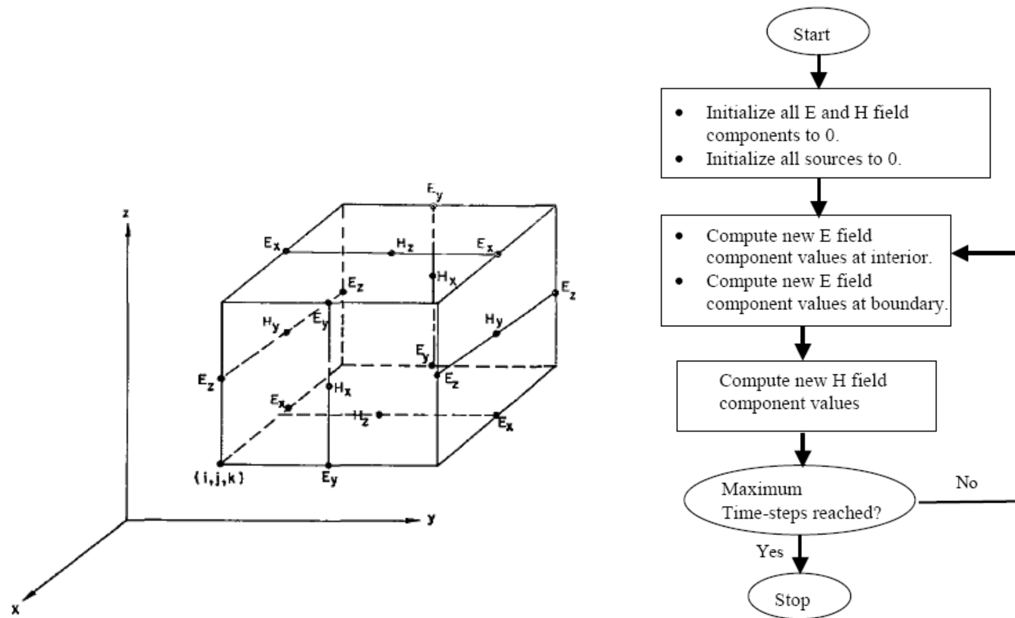

Figure B.1 Positions of the field components about a unit cell of the Yee lattice and FDTD algorithm [2].

B.2 Boundary conditions in FDTD

Boundary conditions are used to truncate the computational domain when modeling an open region problem. Mur [4] proposed absorbing boundary conditions in 1980. Its accuracy was further improved by Mei and Fang [5] with the introduction of super absorption technique. Chew [6] proposed Liao's boundary condition. Mei's and Chew's boundary conditions perform better than Mur's condition especially at oblique incident waves. But they suffer from either an instability problem or inaccurate solutions. Berenger's *perfect matching layer* (PML) absorbing boundary conditions is reported to be most robust and effective [7-8]. PML conditions allow radiation to propagate out of the computational area without interfering with the fields inside. In this thesis, PML boundary used as an absorbing media to truncate the simulation region. We must note here, in the strict sense, PML is not a boundary condition but a perfectly absorbing layers placed adjacent to the boundaries of the simulation region.

Table B.1 PML parameters used in FDTD simulations.

PML parameter	Value
Kappa (The normalized imaginary electric and magnetic conductivity)	2
Sigma (The maximum normalized electric and magnetic conductivity)	0.25
Layers	12
Polynomial power (How rapidly the electric and magnetic conductivity increases as radiation propagates at normal incidence into the PML)	3

References

[1] *FDTD Solutions, from Lumerical Solutions Inc., http://www.lumerical.com.*

[2] K. S. Yee, "Numerical solution of inital boundary value problems involving Maxwell's equations in isotropic media," *IEEE Trans. Antenna and Propagation* **14(3)**, 302-307 (1966).

[3] A. Taflove and S. C. Hagness, *Computational Electrodynamics: the finite difference time-domain method.* Boston: Artech House, (2005).

[4] G. Mur, "Absorbing boundary conditions for the finite-difference approximation of the time-domain electromagnetic-field equations," *IEEE Trans. Electromagn. Compat.* **23(4)**, 377-382 (1981).

[5] K. K. Mei and J. Fang, "Superabsorption--A method to improve absorbing boundary conditions," *IEEE Trans. Antenna and Propagation* **40(9)**, 1001-1010 (1992).

[6] Z. Liao, H. L. Wong, Y. Baipo, and Y. Yuan, "Transmitting boundary for transient wave analyses," *Scientia Sinica* **27(10)**, 1063-1076 (1984).

[7] J. P. Berenger, "A perfectly matched layer for the absorption of electromagnetic-waves," *J. Comp. Phys.* **114(2)**, 185-200 (1994).

[8] J. P. Berenger, "Three-dimensional perfectly matched layer for the absorption of electromagnetic waves," *J. Comp. Phys.* **127(2)**, 363-379 (1996).

Appendix C

Focused Ion Beam (FIB) Nanofabrication

C.1 Focused Ion Beam (FIB) for Device Fabrication

FIB etching has been widely used as a versatile maskless lithography technique in numerous fields. FIB systems generally use an ion beam of Ga^+, focused to a spot size as small as 7 nm in diameter and accelerated up to 50 keV energies. Nanopatterning using FIB etching is generally employed for device modification, transmission electron microscopy (TEM) sample preparations etc. Because FIB patterning saves process steps and time by reducing of hassles and defects inherent in mask transferring in other lithographic techniques, it can be exploited to develop prototypes of microsystem as well as optoelectronic devices.

C.2 Review of Micromachining by Focused Ion Beam (FIB)

C.2.1 Simple Milling

Simple milling in FIB refers to the sputtering phenomenon due to energetic impingement of focused ion beam on the target material. It is possible to process several tens on nanometer level area without using a mask. This is the reason it is also termed as “maskless etching”. In addition, provision to observation of processing condition under microscope makes very accurate and high precise results possible.

C.2.1.1 Beam Current

Ion beam current and beam diameter play important roles in FIB milling. Young et al [1] reported effect of a beam current on milling yield and resolution of pattern. Beam

diameter is a function of ion beam current. When ion beam current decreases, the numbers of ion decreases. The beam diameter is dependent on the ability to focus the ions. A smaller beam diameter results in better pattern definition. Nevertheless, a smaller beam current takes a long time to mill a pattern.

C.2.1.2 Angle of Incidence

The relationship between incident angles and sputtering yield was investigated by Xu et al [2]. They found that the sputtering yield increases as the incident angle increases, but sputtering yield decreases for angles around 75° - 80° for Ga^+ ions due to more incident ions being scattered from the target surface.

Tseng et al [3] carried out TRIM simulation to see the dependence of the sputtering yield on the incident angle with two types of ions, *As* and *Ga*, in sputtering of *Au* and *Si* substrates. The simulated results were compared with experimental data by Santamore et al [4] and Leher et al [5] (See Figure C.1(a)).

Ion incidence angle effect on lateral dimensions and depth of diffractive structure was investigated by Fu et al [6]. The period of the structure increases and the depth degrades as the ion incidence angle increases (Figure C.1 (b)).

In all reports, the maximum is reported around 80° incidence angle. Sputtering yield is governed by the surface collision cascade. As incidence angle increases from normal incidence, the probability of the target atoms escaping from the surface during cascade increases. At glancing angles, surface channeling plays an important role that causes the sputter yield to decrease, which is another reason for the smaller depths at large incidence angles.

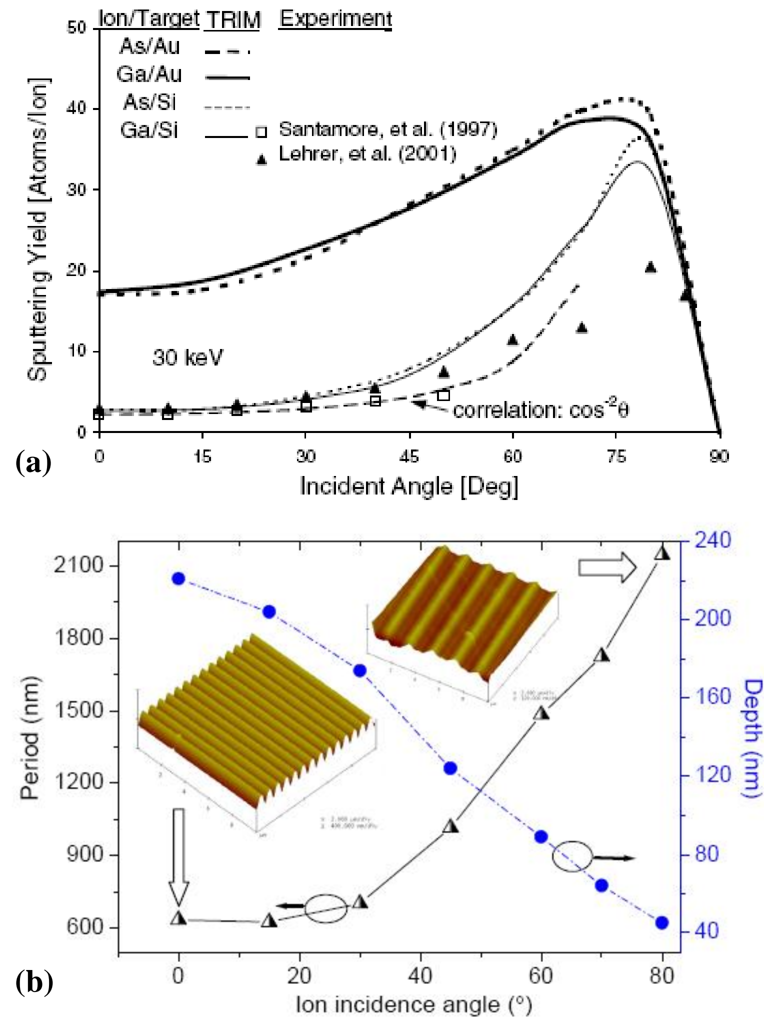

Figure C.1 (a) Ion incidence angles versus lateral dimension [3] and (b) dimensions of the diffractive structures on Si (111) [6].

C.2.1.3 Ion Energy

Tseng et al [7] investigated the effect of ion energy on two types of target substrates (*Au* and *Si*) using three types of ion sources (*As*, *Ga* and *Ar*) at normal incidence as a function of the ion energy. TRIM simulation was employed and results were compared with the experimental data. The sputtering yield of the *Au* substrate is much higher than that of the *Si* substrate. *As*, *Ga* and *Ar* shows decreasing yield according to their decreasing atomic weights as shown in Figure C.2 (a).

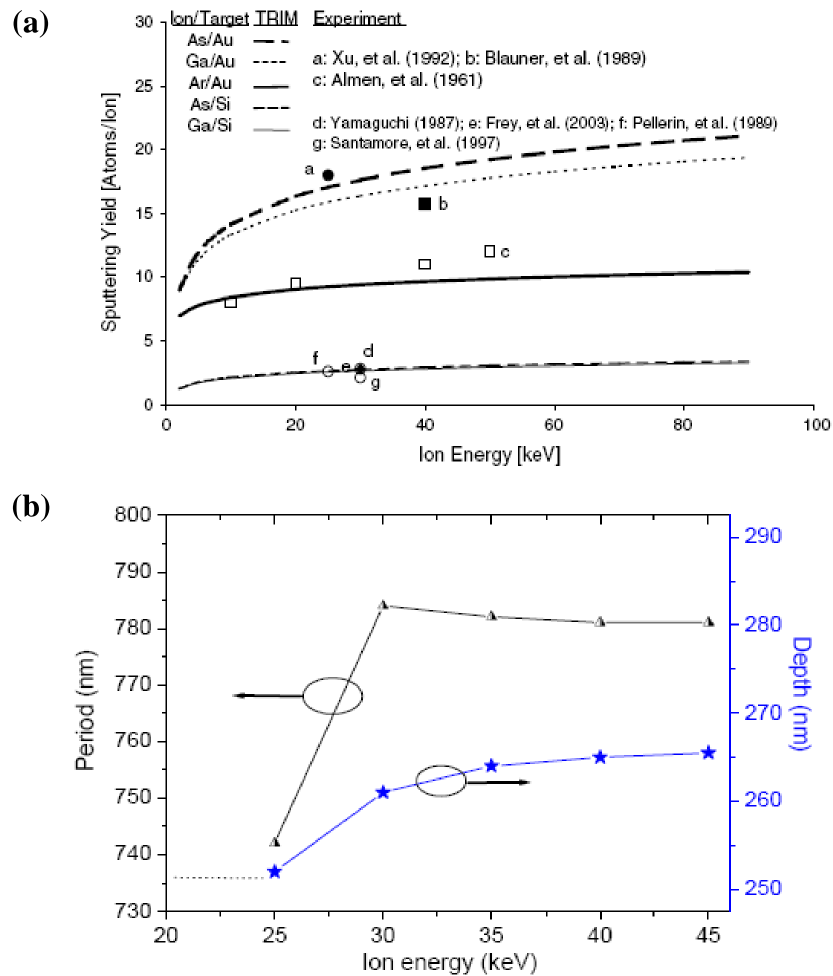

Figure C.2 Effect of ion energy on (a) sputtering yield [7] (b) depth and period of diffractive structure [6].

C.2.1.4 Dwell Time (or Ion Dose)

While milling a pattern, FIB system digitizes it into an array of pixels. Ion beam is then moved pixel by pixel. At each pixel, the ion beam is kept for a certain period termed as a dwell time. If all other operating parameters are constant, the ion dose is proportional to the dwell time, i.e. the longer the dwell time, the higher the ion dose.

Hausmann et al [8-11] investigated extensively the dwell time effect on FIB ion implantation in cobalt disilicide. However, ion implantation is quite different from milling process. Fu et al [12] investigated the influence of dwell time on FIB micromachining process by means of a single pixel-writing mode sputtering of *Si*.

Long dwell time leads to deep sputtering depth due to the reduction of the scanning pixel numbers.

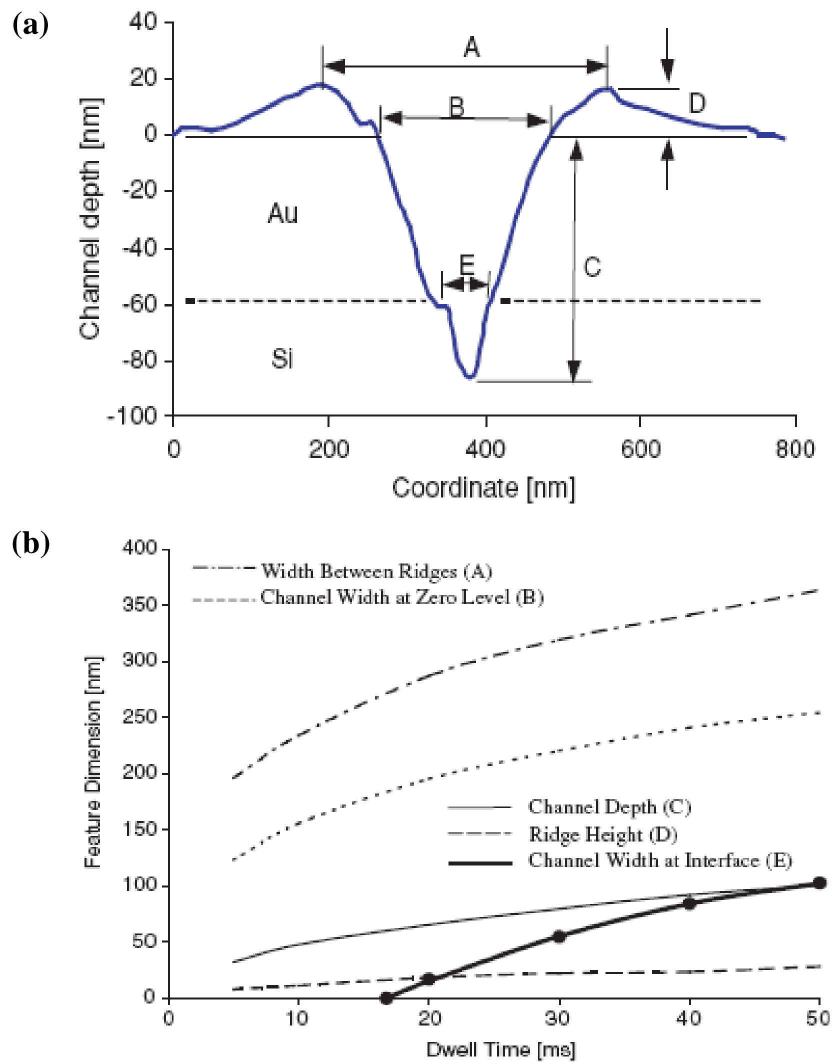

Figure C.3 (a) AFM measurement and feature definition of a typical channel cross section in *Si* substrate. (b) Channel profile measurement for various dwell times [7].

Tseng et al [7] used different dwell times to obtain different submicron channels on gold-coated *Si* substrates. They observed that the channel is milled deeper (Figure C.3) as the dwell time is increased and the rate of increase of the channel depth is gradually reduced with increasing dwell time.

Xiong et al [13] observed that the milling depth increases linearly with the dose density for depths less than 7 nm in milling ($Ni_{80}Fe_{20}$) permalloy nanochannels. On the other hand, Li et al [14] studied the nanochannel profiles at several dwell times (0.1, 1, 10 and 100 μs) and beam currents (1, 4, 11 and 70 pA) and found that the channel depth increases almost linearly with the ion dose but not with the dwell time.

C.2.1.5 Number of Passes

Yamaguchi et al [15] studied the effects of using single and repetitive passes on milling a *Si* substrate. It can be seen from Figure C.4, with a single pass, a cavity with an inclined bottom was observed and the depth of the cavity at the end of the milling is far deeper than the depth from where the milling is commenced. Tapered bottom may be attributed to the redeposition effect. Repetitive passes yields more uniform milling.

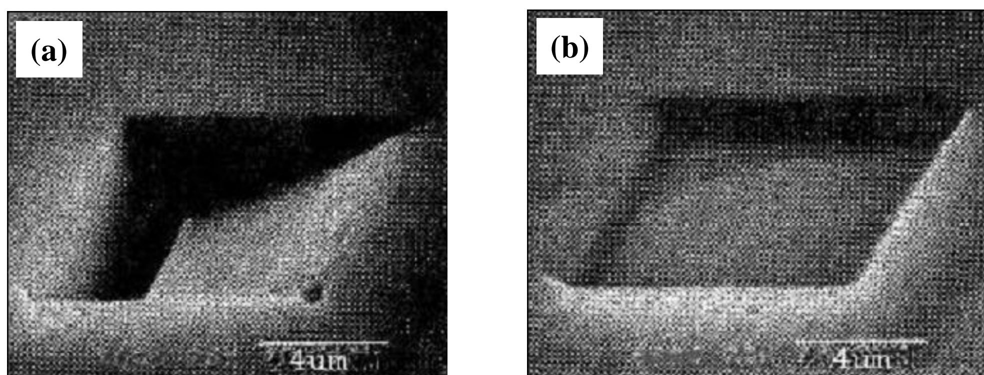

Figure C.4 SEM photographs of *Si* pattern (a) slow single pass at 2 s per line with 300 scan lines; (b) fast (200) repetitive passes at 10 ms per line with 300 scan lines [15].

Fu et al [12] milled an annular cavity by a single pass and four repetitive passes as shown in Figure C.5. Changing from a single pass scheme to a repetitive approach enlarges the diameter of the tip or increases the slope of the cone. Using repetitive

passes, the redeposition will be proportionally reduced in each pass and a portion of the redeposition from the earlier passes can be removed by the subsequent passes.

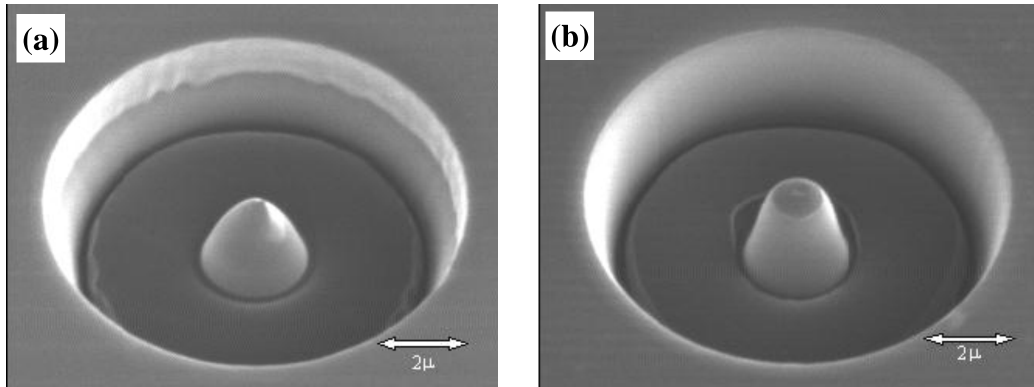

Figure C.5 Tip structures milled: (a) using a single pass (b) using four repetitive passes [12].

C.2.2 Milling with Enhanced Etch

Low throughput of FIB sputtering limits its applications to prototype or nanostructure formation. Introduction of reactive gases like Cl_2, XeF_2 etc. results in improved etch rate compared to sputtering rate of many materials like *Si*, *Al*. The process is termed as *gas assisted etching* (GAE) or *chemical assisted focused ion beam machining* (CE-FIBM).

Chemical enhancements of material removal rates result from chemical reactions that are initiated by impinging Ga^+ ions. These reactions involve a chemical injected into the vacuum, which then adsorbs to the sample surface and the surface constituents of the material being micromachined. Ideally, these reactions increase the material removal rate and result in a volatile reaction product, thus reducing redeposition of micromachined material.

Various gas species have been investigated for different work materials. A mixture of Cl_2 and NH_3 was successfully demonstrated by Edinger [16] to enhance *Cu*

removal rate. However, a redeposition or the formation of corrosion products was clearly observed in the approach. Gonzalez et al [17, 18] have demonstrated that the use of organochlorides and oxygen containing precursors increases the FIB machining selectivity of copper with respect to SiO_2 by a factor of 4. Problems like differential sputtering due to different crystolligrahpic grain oreientation (see Figure C.6) are shown to be overcome by GAE [19].

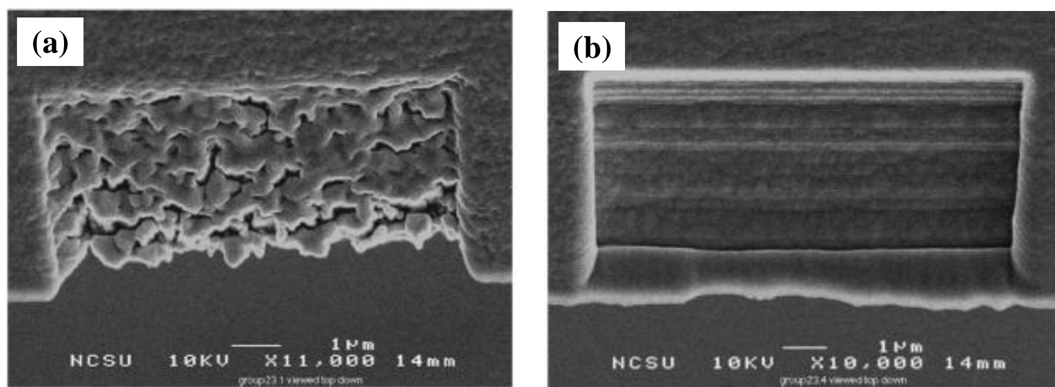

Figure C.6 Free edge micromachining of Permalloy (a) without chemical enhancement and (b) using C_2Cl_4 [19].

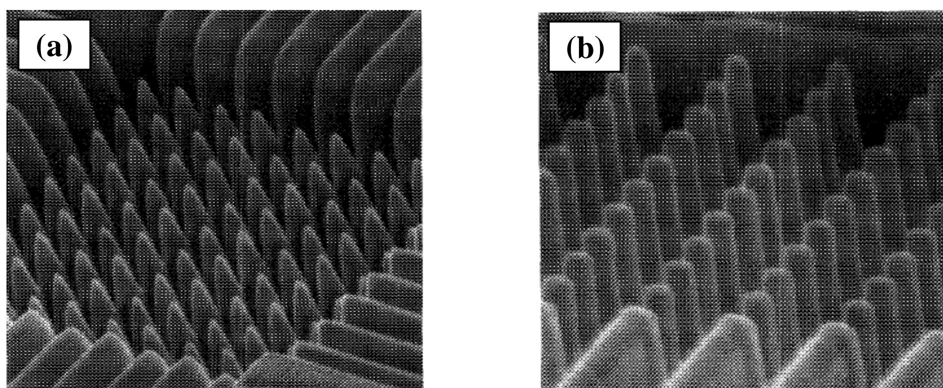

Figure C.7 Array of pillars etched in *GaAs* (a) without protective layer (b) with a protective layer present (0.3 μm PMMA) [20].

Young et al [20, 21] exploited etch selectivity with some material combinations (Figure C.7). The etch selectivity between two materials is the ratio of

the relevant etch rates under the same etch parameters. For instance, over etching of Al layer on SiO_2 with a little etching of SiO_2 is possible because of high selectivity of order of 15–20 between the two materials. In addition, the undesirable effects of ion beam profile (approximated as Gaussian distribution with long tails) like rounded edges to etched features and implantation to the area surrounded by the recess can be minimized by using a sacrificial layer on the top of the substrate. It can be seen from Figure where an array of pillars was milled using GAE with and without protective layer of 0.3 μm PMMA.

GAE when combined with geometrical micromachining can further enhance micromachining capability. Geometrical micromachining enhancement takes advantage of the greater sputtering rates available at very high impact angle, i.e., close to parallel to the surface to be micromachined. This combination has been exploited for micromachining permalloy using C_2Cl_4 [22, 23], for sharpening of diamond cutting tools with H_2O [24], and for measurement of photoresist line widths without sample cleaving with H_2O [25].

Table C.1 Etch rate enhancement for various gas-target combinations. (edited from [17, 19, 26, 27]).

Gas	Target	Etch rate (μm^3/nC)	Enhancement factor
Cl_2	Silicon	2.6	11.8
	Aluminum	0.6	3
	GaAs	6.9	10
	Silver	1.1-2.8	< 2
H_2O	Diamond	1	7
	PMMA	7.5	15
	Polyamide	8.5	17
XeF_2	Silicon	---	7-12

Gas	Target	Etch rate ($\mu m^3/nC$)	Enhancement factor
C_2Cl_4	Permalloy	0.78	7.8
I_2	PMMA	0.9	2

References

[1] R. J. Young, "Micro-machining using a focused ion beam," *Vacuum* **44(3-4)**, 353-356 (1993).

[2] X. Xu, A. D. Della Ratta, J. Sosonkina, and J. Melngailis, "Focused ion beam induced deposition and ion milling as a function of angle of ion incidence," *J. Vac. Sci. Technol. B* **10(6)**, 2675-2680 (1992).

[3] A. A. Tseng, "Recent developments in micromilling using focused ion beam technology," *J. Micromech. Microeng.* **14(4)**, 15-34 (2004).

[4] D. Santamore, K. Edinger, J. Orloff, and J. Melngailis, "Focused ion beam sputter yield change as a function of scan speed," *J. Vac. Sci. Technol. B* **15(6)**, 2346 (1997).

[5] C. Lehrer, L. Frey, S. Petersen, and H. Ryssel, "Limitations of focused ion beam nanomachining," *J. Vac. Sci. Technol. B* **19(6)**, 2533-2538 (2001).

[6] Y. Fu, N. K. A. Bryan, and W. Zhou, "Quasi-direct writing of diffractive structures with a focused ion beam," *Opt. Express* **12(9)**, 1803-1809 (2004).

[7] A. A. Tseng, I. A. Insua, J. S. Park, B. Li, and G. P. Vakanas, "Milling of submicron channels on gold layer using double charged arsenic ion beam," *J. Vac. Sci. Technol. B* **22(1)**, 82-89 (2004).

[8] S. Hausmann, L. Bischoff, J. Teichert, D. Grambole, F. Herrmann, and W. Moller, "Investigation of dwell-time effects on the cobalt disilicide formation using focused ion beam implantation," *Microelectron. Eng.* **42**, 233-236 (1998).

[9] S. Hausmann, L. Bischoff, J. Teichert, M. Voelskow, D. Grambole, F. Herrmann, and W. Moller, "Dose rate effects in focused ion beam synthesis of cobalt disilicide," *Appl. Phys. Lett.* **72(21)**, 2719 (1998).

[10] S. Hausmann, L. Bischoff, J. Teichert, M. Voelskow, and W. Moller, "Dwell-time related effects in focused ion beam synthesis of cobalt disilicide," *J. Appl. Phys.* **87(1)**, 57-62 (2000).

[11] S. Hausmann, L. Bischoff, M. Voelskow, J. Teichert, W. Moeller, and H. Fuhrmann, "Dwell-time effects in focused ion beam synthesis of cobalt

disilicide: Reflectivity measurements," *Nuc. Instr. Meth. Phys. Res. B* **148(1-4)**, 610-614 (1999).

[12] Y. Fu, N. K. A. Bryan, and O. N. Shing, "Microfabrication of diffractive optical element with continuous relief by focused ion beam," *Microelectron. Eng.* **54(3-4)**, 287-293 (2000).

[13] G. Xiong, D. A. Allwood, M. D. Cooke, and R. P. Cowburn, "Magnetic nanoelements for magnetoelectronics made by focused-ion-beam milling," *Appl. Phys. Lett.* **79(21)**, 3461 (2001).

[14] H. W. Li, D. J. Kang, W. T. S. Huck, and M. G. Blamire, "Focused ion beam fabrication of silicon print masters," *Nanotechnol.* **14(2)**, 220-223 (2003).

[15] H. Yamaguchi, A. Shimase, S. Haraichi, and T. Miyauchi, "Characteristics of silicon removal by fine focused gallium ion beam," *J. Vac. Sci. Technol. B* **3**, 71-74 (1985).

[16] K. Edinger, "Gas assisted etching of copper with focused ion beams," *J. Vac. Sci. Technol. B* **17(6)**, 3058-3062 (1999).

[17] J. C. Gonzalez, D. P. Griffis, T. T. Miau, and P. E. Russell, "Chemically enhanced focused ion beam micromachining of copper," *J. Vac. Sci. Technol. B* **19**, 2539-2542 (2001).

[18] J. C. Gonzalez, M. I. N. da Silva, D. P. Griffis, and P. E. Russell, "Improvements in focused ion beam micromachining of interconnect materials," *J. Vac. Sci. Technol. B* **20(6)**, 2700-2704 (2002).

[19] P. E. Russell, T. J. Stark, D. P. Griffis, J. R. Phillips, and K. F. Jarausch, "Chemically and geometrically enhanced focused ion beam micromachining," *J. Vac. Sci. Technol. B* **16(4)**, 2494 (1998).

[20] R. J. Young, J. R. A. Cleaver, and H. Ahmed, "Characteristics of gas-assisted focused ion beam etching," *J. Vac. Sci. Technol. B* **11(2)**, 234-241 (1993).

[21] R. J. Young, J. R. A. Cleaver, and H. Ahmed, "Gas-assisted focused ion beam etching for microfabrication and inspection," *Microelectron. Eng.* **11(1-4)**, 409-412 (1990).

[22] D. M. Thaus, T. J. Stark, D. P. Griffis, and P. E. Russell, "Development of focused ion-beam machining techniques for Permalloy structures," *J. Vac. Sci. Technol. B* **14(6)**, 3928 (1996).

[23] D. M. Thaus, T. J. Stark, D. P. Griffis, and P. E. Russell, "Organochloride chemically enhanced focused ion beam micromachining of permalloy," *Appl. Phys. Lett.* **68(26)**, 3829 (1996).

[24] D. P. Adams, M. J. Vasile, G. Benavides, and A. N. Campbell, "Micromilling of metal alloys with focused ion beam-fabricated tools," *Prec. Eng.* **25(2)**, 107-113 (2001).

[25] T. J. Stark, D. P. Griffis, and P. E. Russell, "Characterization of resist profiles using water enhanced focused ion beam micromachining," *J. Vac. Sci. Technol. B* **14(6)**, 3990-3995 (1996).

[26] J. Orloff, M. Utlaut, and L. Swanson, *High resolution focused ion beams: FIB and its applications*. New York: Kluwer academic/plenum publishers, (2003).

[27] T. J. Stark, G. M. Shedd, J. Vitarelli, D. P. Griffis, and P. E. Russell, "H_2O enhanced focused ion beam micromachining," *J. Vac. Sci. Technol. B* **13(6)**, 2565-2569 (1995).

List of Publications

1. R. G. Mote, S. F. Yu, A. Kumar, W. Zhou and X. F. Li, *Experimental Demonstration of Near-Field Focusing of a Phase Micro-Fresnel Zone Plate (FZP) under Linearly Polarized Illumination*, Applied Physics B (Lasers and Optics), Vol. 102, No. 1, pp. 95-100 (2011).
   (DOI: 10.1007/s00340-010-4210-8).
2. R. G. Mote, S. F. Yu, W. Zhou and X. F. Li, *Sub-wavelength Focusing Behavior of High Numerical-aperture Phase Fresnel Zone Plates under Various Polarization States*, Applied Physics Letters, Vol. 95, No. 19, Art. No. 191113, (2009).
   (DOI: 10.1063/1.3263728).
3. R. G. Mote, S. F. Yu, W. Zhou and X. F. Li, *Design and Analysis of Two-dimensional High-Index-Contrast Grating Surface-emitting Lasers*, Optics Express, Vol. 17, No. 1, pp. 260-265 (2009).
   (DOI: 10.1364/OE.17.000260).
4. R. G. Mote, S. F. Yu, B. K. Ng, W. Zhou, and S.P. Lau, *Near-field Focusing Properties of Zone Plates in Visible Regime – New Insights*, Optics Express, Vol. 16, No. 13, pp. 9554-9564 (2008). (Selected for Virtual Journal for Biomedical Optics, Vol. 3, No. 7, 2008).
   (DOI:10.1364/OE.16.009554)